STUDY OF RESONANCE LIGHT SCATTERING FOR REMOTE OPTICAL PROBING

by

C. M. Penney (Principal Investigator), W. W. Morey, R. L. St. Peters, S. D. Silverstein, M. Lapp, and D. R. White

Prepared under Contract No. NAS 1-11624

by

General Electric Corporate Research and Development
P. O. Box 8
Schenectady, New York 12301

for

NATIONAL AERONAUTICS AND SPACE ADMINISTRATION
LANGLEY RESEARCH CENTER
HAMPTON, VIRGINIA 23365

September 1973

SRD-73-125

TABLE OF CONTENTS

TABLE OF CONTENTS (Continued)

LIST OF ILLUSTRATIONS

STUDY OF RESONANCE LIGHT SCATTERING FOR REMOTE OPTICAL PROBING

C. M. Penney (Principal Investigator), W. W. Morey, R. L. St. Peters, S. D. Silverstein, M. Lapp, and D. R. White

SUMMARY

The objective of the work described in this report is to investigate enhanced scattering and fluorescence processes in the visible and uv which will enable improved remote measurements of gas properties.

The theoretical relationship between scattering and fluorescence from an isolated molecule in the approach to resonance is examined through analysis of the time dependence of re-emitted light following excitation by pulsed incident light. Quantitative estimates are developed for the relative and absolute intensities of fluorescence and resonance scattering. New results are obtained for depolarization of scattering excited by light at wavelengths within a dissociative continuum.

The experimental work was performed in two separate facilities. One of these utilizes argon and krypton lasers, single moded by a tilted etalon, and a 3/4 meter double monochromator. This facility was used to determine properties of the re-emission from NO_2, I_2 and O_3 excited by visible light.

The second facility involves a narrow-line dye laser, and a 3/4 meter single monochromator. The dye laser produces pulsed light with 5 nsec pulse duration and 0.005 nm spectral width. The spectrometer and associated electronics provide both time (6 nsec) and spectral (0.02 nm) resolution of the re-emitted light. This facility was used to measure the absolute vibrational Raman scattering cross sections of N_2 and O_2 at 300 nm, and to examine in detail the fluorescence from SO_2 excited at various wavelengths near 300 nm. It was found that both N_2 and O_2 cross sections are several times larger than predicted by a $(1/\lambda_{scatter})^4$ extrapolation from the visible. Sharp line fluorescence from SO_2 in air near STP was observed to be 10^4 time stronger than the N_2 vibrational Raman scattering. Comparable or larger cross sections for O_3 and numerous atomic species are estimated.

Use of the strong scattering and fluorescence processes in various measurement situations is considered. Among the remote, range-resolved measurements that appear practical are: ambient SO_2 and O_3 in the lower atmosphere from the ground; O_3 in the stratosphere from the ground; and numerous atomic species at altitudes above 50 km from a satellite.

I. INTRODUCTION

The objective of the work described in this report is to identify and investigate optical processes in the visible and ultraviolet that can expand the capabilities of remote, spatially resolved measurements of gas properties. The optical processes considered here are those that divert light from an incident beam, such that some of the diverted light returns to a collector. Intensity, spectral and/or polarization analysis of the collected light provides information about the gas volume from which it came.

One type of probe based on this principle is the single-ended LIDAR system, illustrated in Fig. 1. This type of probe has already been employed with considerable success for ground- and air-based studies of the atmosphere (refs. 1 and 2) and shows good potential for satellite-based studies. A second example is the bi-axial system shown in Fig. 2, which can be used to obtain precise three-dimensional resolution in relatively small regions such as a wind tunnel (ref. 3).

There are a number of optical diversion processes upon which such probing systems can be based. Ideally, the observed process should have the following characteristics:

(a) It should be effectively instantaneous. This characteristic is particularly desirable for LIDAR applications, where ranging is accomplished through timing. In practice, it is often preferable that the observed process introduce less than 10^{-8} second time uncertainty.

(b) The intensity of the diverted light per molecule should be independent of gas pressure and constituency.

(c) The returned light should be characteristic of the observed molecules and their states of excitation.

(d) The process should be strong enough for easy observation, but not so strong as to prevent light transmission to the measurement point.

We shall consider several optical processes which meet these criteria to varying degree. The processes can be divided into two types: scattering and fluorescence. Within the title of this report, the work "scattering" is used to denote both of these processes generically. However, subsequently, we will use this term exclusively to designate those processes which are effectively instantaneous and insensitive to collision effects such as relaxation, collisional depolarization and quenching. On the other hand, we shall use the term fluorescence to designate processes which are intrinsically "slow", displaying a time uncertainty at low gas pressures which is typically greater than 10^{-8} sec, and a corresponding sensitivity to collision effects at high pressure.

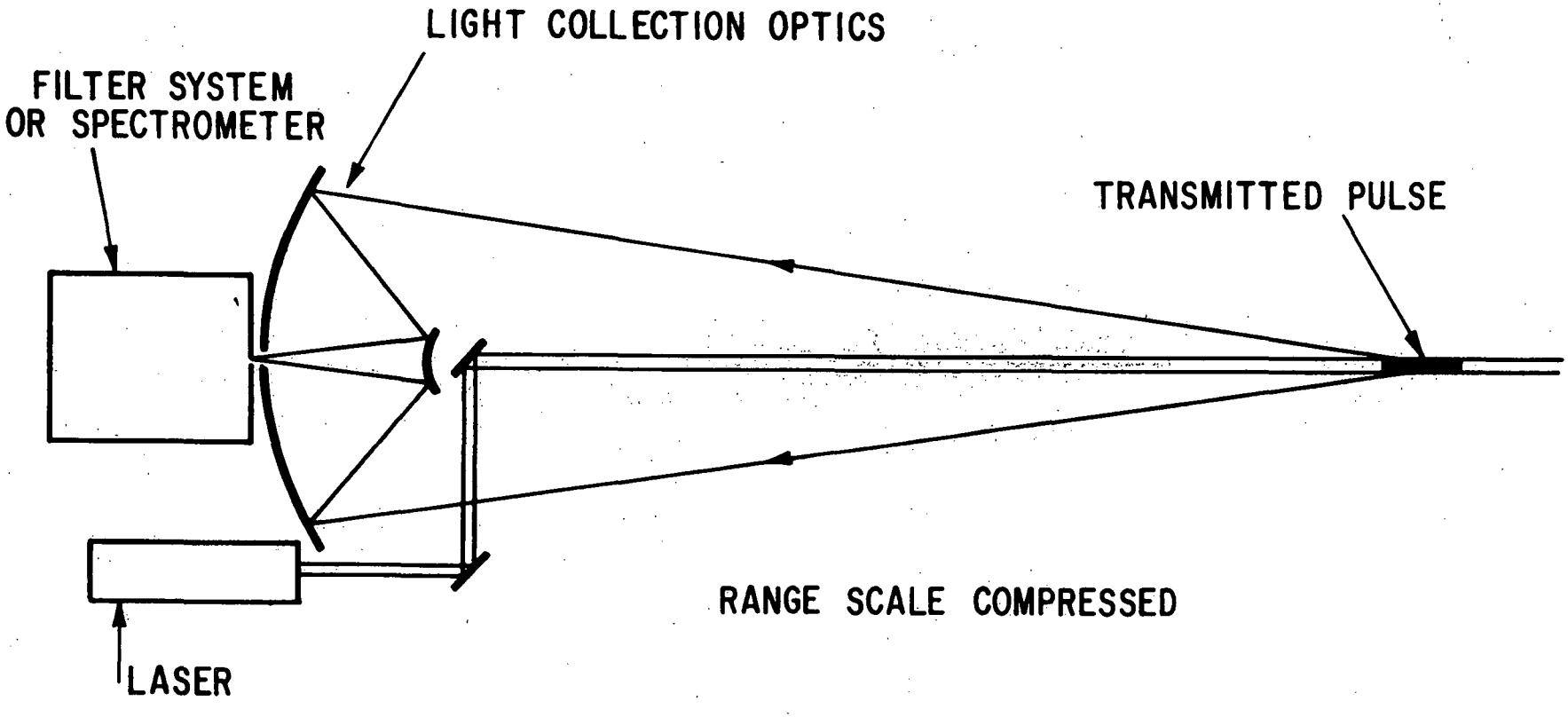

Figure 1 LIDAR (LIght Detecting And Ranging) single ended optical probe. In this system, ranging is accomplished by correlation to time-of-flight of a light pulse. For illustrative purposes, the range scale is greatly compressed on the figure in comparison to typical configurations.

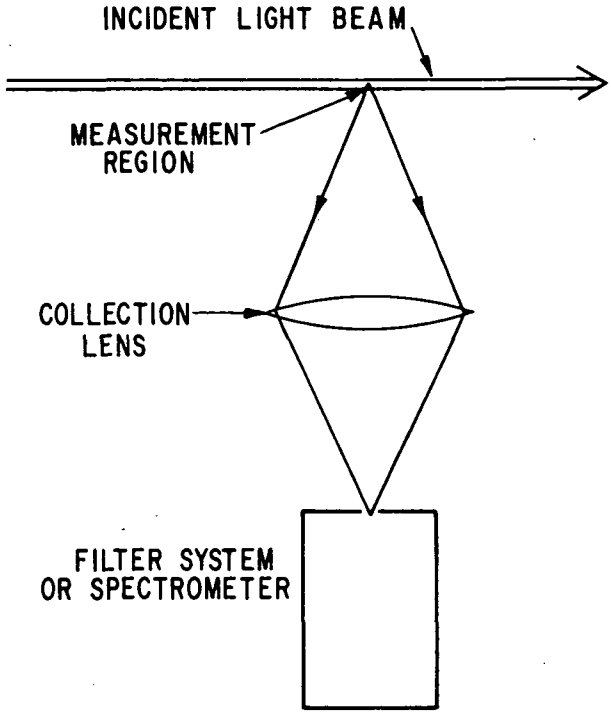

Figure 2 Bi-axial optical probe. This configuration provides convenient three-dimensional resolution at close range.

Although fluorescence is often thought of as a process following actual excitation into an excited state, the distinction between fluorescence and scattering does not always correlate with separation from resonance. There are situations to be considered in which excitation in a strong absorption region produces scattering. This type of process is often called resonance scattering (ref. 4). However, the use of such terms in the literature extends to processes which could also be regarded legitimately as fluorescence, producing a somewhat confusing situation. In Appendix A we describe several different criteria for distinguishing between scattering and fluorescence that have appeared in the literature. The present choice is based on two considerations: First, scattering has been regarded by many as an "instantaneous" process, in which case there is not time for collisions to occur. Second, this choice is convenient for gas probe applications, because under conditions of present interest scattering satisfies the first two "ideal" properties we have listed for a probe, whereas fluorescence often fails one or both of these criteria.

Because nature often fails to accommodate idealism, ultimately we will consider both scattering and fluorescence processes in some detail. Thus at this point we present a descriptive list of some of the general types of optical

diversion processes that are potentially useful for gas probing. The list serves to introduce terminology, and to provide an initial orientation concerning these processes. The general types of transitions involved in the molecular processes included in this list are illustrated by level diagrams in Fig. 3.

Scattering from Molecules

Rayleigh scattering. - In this process light is scattered from a molecule whithout exchanging any energy with the internal states of the molecule. Only the very small amount of energy necessary to conserve momentum between the light photon and scattering molecules is exchanged (Doppler-Brillouin effect). Therefore the scattered light has nearly the same spectral distribution as the incident light, and it is very difficult to determine the relative concentration of different molecules from this spectral distribution. Temperature information is accessible from the spectral distribution, but, because of the small amounts of energy exchanged, it requires rather delicate measurements.

Raman scattering. - This process involves an exchange of a significant amount of energy between the scattered light photon and the scattering molecule. Consequently, the scattered light undergoes substantial shifts in wavelength. The resulting bands of scattered light are characteristic of the particular molecule. The intensity of a band is proportional to the number of molecules in the particular initial state leading to that band. Thus Raman scattering provides direct information about both the constituency and excited state populations of molecules in a system.

Elastic light scattering by particles. - In this process, which is often called Mie scattering (appropriate for spherical homogeneous particles), light is scattered from particles suspended in the gas. The light undergoes only the (usually) minute spectral shift arising from the particle motion. However, the dependence of the scattering on incident wavelength, on polarizations of incident and scattered light, and on scattering angles can be used to obtain some information about the particle distribution.

Luminescence from Molecules

Fluorescence. - This process can be initiated by absorption of light at a wavelength within a particular absorption line or band of a molecule. Subsequently, the molecule may re-emit light in a transition from the excited state to the original or a different lower state. The probability of re-emission per unit time γ is usually constant such that at very low pressures the fluorescence intensity displays an exponential decay curve with time constant $1/\gamma$. However, before a molecule can de-excite by emitting light, the excitation may be

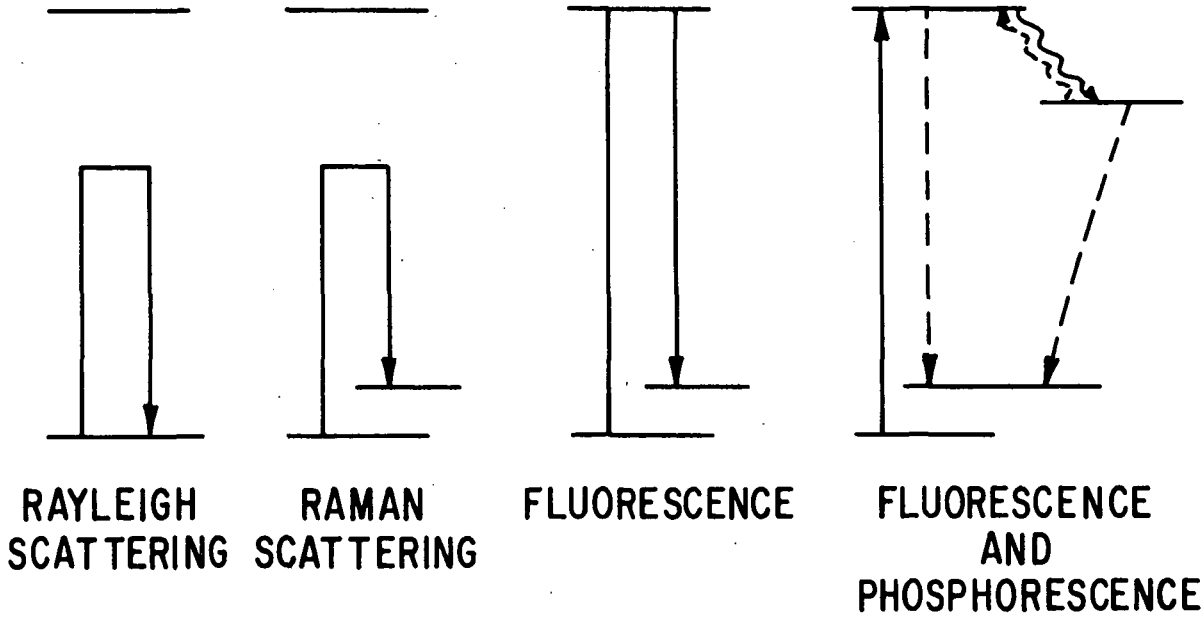

Figure 3 Level diagram illustrating various optical diversion processes in molecules.

altered by some non-radiative process . For example, the molecule may undergo collisions with other molecules. These collisions can have several effects. One effect is that they can cause the molecule to lose "memory" of the direction and polarization of the incident beam, increasing the depolarization of the fluorescence and decreasing the anisotropy of its angular distribution. Collisions in which small amounts of energy are exchanged redistribute the excitation among various upper molecular states, broadening the spectral distribution of the fluorescence. In other collisions all or most of the excitation energy is degraded in a non-radiative process. For example, it may be converted to kinetic energy. The latter phenomenon reduces the fluorescence intensity and is, therefore, referred to as quenching. Quenching also shortens the decay time of re-emission, as mentioned previously. This effect is advantageous for time-of-flight ranging. However, in general, collision processes render the fluorescence spectral distribution, polarization and intensity per molecule dependent upon the gas constituency and total pressure. Therefore, the effect of these processes must be known or calculated before quantitative data can be obtained from fluorescence. In particular, if the collision effects are dominated by a species of variable concentration, the concentration of the quenching species must be measured separately.

Although collision effects tend to smooth out the spectral detail in fluorescence, nevertheless enough detail is often retained even at atmospheric pressure to allow identification of the fluorescing species.

Phosphorescence. - This process involves excitation to an upper state, followed by a transition, often collision-induced, to a state from which radiative decay is forbidden. Phosphorescence is composed of the slow forbidden decay, and of fast decay following a second transition, again often collision-induced, back to the states with allowed transitions. Since phosphorescence involves a more detailed collision history than fluorescence, and is often slow even at high pressure, it is rarely used in gas probing.

Scattering and Luminescence from Particles

In addition to the processes mentioned in the list above, particles can contribute Raman scattering, fluorescence and phosphorescence. Among these, Raman scattering is very weak, but fluorescence seems likely to provide useful measurements of particle properties. However, this subject will not be addressed specifically in this paper.

Optical Diversion Processes and Gas Probing

Raman scattering. - Among the processes discussed above, only Raman scattering (RS) completely satisfies the first three "ideal" properties for an optical probe; i.e., it is instantaneous, not sensitive to quenching, and characteristic of the type and excitation of the scattering molecules. Furthermore, RS does not require a tunable laser, and data analysis to obtain desired

information about the gas is relatively simple. However there is one substantial disadvantage of ordinary RS - it is relatively weak. For example, a typical RS cross section for scattering of visible light is 10^{-30} cm^2/sr per molecule (ref. 5.). In contrast, a typical Rayleigh cross section is about 1000 times larger (ref. 6), and a fluorescence cross section, about 10^{10} to 10^{16} times larger (in the absence of quenching). Because RS is so weak, RS probes with high sensitivity at long range require large lasers and collector lenses. In fact, limitations of size, weight, expense, safety and/or present technology are often reached all too soon in such applications. That point will be examined in some detail in Chapter IV. However at the present time it serves to introduce the question of major interest in this report; namely, can we find processes which are much stronger than ordinary RS, yet share to a useful extent its desirable characteristics for optical probing?

Enhanced scattering upon approach to resonance. - Indeed, the possibility of strongly enhanced RS itself is suggested by the resonance-like structure of the basic quantum expression for scattering. We will argue that this equation, which is presented in Chapter II, describes both scattering and fluorescence, at least in simple systems represented by a two or three level quantum model. In this case the resonance peaks produce fluorescence, and not scattering. As the incident light frequency approaches a strong, isolated absorption line, the character of the diverted light will undergo a gradual transition from that of scattering (effectively instantaneous and not subject to quenching) into fluorescence. Furthermore, the wavelength dependence of this transition may depend sensitively on detailed line broadening mechanisms which are operative in the experimental situation. (In fact, observation of the scattering-to-fluorescence transition should provide new information about line broadening in the far wings of the absorption line.) However, qualitative theoretical arguments suggest that the intensity of RS can be substantially enhanced in the approach to a strong isolated absorption line or band before the transition to fluorescence-like properties occurs. This type of scattering, which has been called pre-resonance or near-resonance Raman scattering, has attracted interest among those who use RS as a gas probe; therefore, it has received substantial attention in the work reported here.

Scattering following excitation into a dissociative continuum. - In this process a molecule is excited by light with sufficient photon energy to cause it to dissociate. However, there is a distinct probability that the molecule will de-excite by re-emitting light before it dissociates. This light displays scattering-like properties because typically dissociation will occur so quickly that the excited molecule has little chance to experience a collision. Consequently the re-emitted light appears "instantaneously" and is insensitive to

collisions and associated quenching, etc. This process has been identified and studied experimentally by Holzer, Murphy and Bernstein (ref. 4) in halogen molecules. Aspects of it have been examined theoretically by Berjot et al. (ref. 7, 8). In particular, moderately strong enhancement of scattering from I_2 has been found under excitation at wavelengths shorter than the dissociation limit near 510 nm (ref. 4).

Scattering over quenched fluorescence. - This process has been discussed by Berjot, Jacon and Bernard (ref. 9, 10) for situations when fluorescence is strongly quenched, leaving a remnant of scattering from intermediate states not in resonance. In this case the intensity of diverted light per absorbing molecule should decrease in propagation to background gas pressure until a "floor" of scattering is reached. Simultaneously the depolarization should go through a characteristic variation. Berjot et al. have examined this phenomenon theoretically and shown favorable comparison to experiments with I_2 in high pressure (up to 40 atm!) argon. However, in Chapter III we shall show that their results may arise at least partially from an alternative mechanism.

Quenching balanced by increased absorption due to line broadening. - The rate of fluorescence per molecule R_F can be expressed as the product of a rate R_A of absorption and a probability P_E of re-emission before quenching (ref. 11). Although P_E will decrease as pressure increases, R_A can increase at a sufficient rate to balance this decrease (or even over-balance it), if the exciting wavelength is on a wing of the absorption line. The increase of R_A can be explained as follows: Both theory and experiment have demonstrated that the area under an absorption line (integral of absorption cross section over wavelength or frequency remains very nearly constant as collisions broaden the line (ref. 12). Therefore, the absorption must decrease on line center, but increase in the wings. This effect has been studied in I_2 vapor by Fouche et al. (ref. 13), and St. Peters et al. (ref. 14). The former group first demonstrated that an enhancement on the order of 10^6 can be obtained at a separation of about 0.1 cm^{-1} from line center, and that this strong re-emission is fairly insensitive to pressure, varying by a factor of $\lesssim 10$ over the range from a few torr to 700 torr. However, there is a strong collision-induced continuum in the re-emission spectral distribution at the higher pressures studied. Therefore, we consider this process to be a form of fluorescence, albeit a potentially useful form.

General fluorescence. - Fluorescence is much stronger than ordinary RS, typically by factors of 10^{10}-10^{16} at low pressure, as mentioned previously. However, it is often more difficult to decipher density and temperature information from measurements of fluorescence intensity, because of resonance absorption of the incident beam (which is sensitive to the fine detail of line broadening), because of quenching and, at low pressure, because of the delay in re-emission which complicates time-of-flight ranging. Furthermore, if narrow line absorption is involved, then efficient use of the incident beam

requires that its spectrum be commensurately narrow and precisely controlled.

Nevertheless, we believe that there are many situations in which fluorescence can be used effectively to probe the atmosphere. One example which has already been implemented is the particularly successful observation of Na and K vapor in the upper atmosphere (refs. 15, 16). These measurements, which have been made from distances on the order of 80 km, are successful largely because the observed atoms are concentrated in a relatively thin layer and their absorption cross sections are very large, producing decay times which are too fast for substantial quenching at that altitude.

However, there is at least one other favorable situation for fluorescence probing of the atmosphere, which has relatively wide applicability. This situation satisfies the following conditions:

1. The species whose measurement is sought exists at low concentration in a carrier gas which dominates line broadening and quenching.

2. The pressure of the carrier gas is known with sufficient accuracy to make line broadening and quenching corrections, and it is high enough to shorten the re-emission delay of observed fluorescence to the point where time-of-flight ranging can be used.

3. The quenched fluorescence of the target species is much stronger than ordinary RS and has a characteristic spectral distribution which allows its identification.

Under these conditions, the fluorescence will be nearly proportional to the concentration of the observed species, and a single-ended LIDAR instrument can be used to observe it with time-of-flight ranging. Moreover, if the absorption bands are fairly wide and smooth, then the requirements on the linewidth and spectral stability of the laser source are not critical. These conditions are satisfied for NO_2 and SO_2. Relevant characteristics of fluorescence from these gases will be described subsequently in this report.

The two fields of enhanced scattering near or in absorption regions, and laser excited fluorescence have experienced rapid acceleration in the last few years. For example, in this period over 100 papers have been published on resonance Raman scattering and closely related subjects. In this introduction we have endeavored to give an overview of those developments which pertain directly to LIDAR probing of the atmosphere. In subsequent chapters, we will explain our own work in more detail, and place it into context with the work of other groups and with ultimate desired applications.

II. THEORY

In this chapter we present theoretical analyses of various aspects of the scattering and fluorescence processes described in the previous chapter. Work performed under this contract will be described in detail and placed into context by brief descriptions of related work performed here under other support, and elsewhere.

Near-Resonance Raman Scattering

Classical Analysis of Scattering. - Here we develop a relatively simple classical model which represents Rayleigh and Raman scattering, as well as fluorescence. Although this classical analysis is not quantitatively correct, it provides a significant qualitative picture of a transition from scattering to fluorescence in the approach to resonance. This picture is confirmed in limiting cases by a detailed quantum-mechanical calculation which will be described subsequently.

Scattering has been characterized by an effectively instantaneous time response, and insensitivity to collision effects. In the case of pulse excitation, these two properties would seem to be closely related, for if the response is instantaneous there is not time for a molecule to experience a collision. Initially, we will use the classical model to investigate the time dependence of re-emission following pulsed excitation. Subsequently, we shall infer the significance of collision effects insofar as possible.

We consider a charged oscillator whose response represents that of a molecule. The alternating electric field of an incident light beam will set this oscillator in motion, such that it radiates a second alternating field which represents the diverted radiation. This field alternates at the same frequency as the incident radiation (for a stationary oscillator) and thus constitutes Rayleigh scattering or resonance fluorescence. However, if the oscillator is, say, rotating, this motion will modulate the properties of the field. Thereupon side bands will be produced in the radiation at a separation from the incident light frequency which is equal to the rotation frequency. These side bands represent rotational Raman scattering or fluorescence. Other types of Raman scattering and fluorescence (vibrational, vibrational-rotational, etc.) can likewise be represented through this model.

We wish to discover what happens as the frequency of incident light is brought near resonance with the oscillator; in particular we wish to ascertain the amplitude and time dependence of the diverted radiation when the incident light is in the form of a short pulse. To do so, we represent the incident light at the oscillator in terms of its electric field

$$I_1 = \frac{c}{4\pi} E_1^2(t) \tag{1}$$

and introduce the Fourier transform $E_1(\omega)$ of the field such that

$$E_1(t) = \int_{-\infty}^{\infty} \frac{d\omega}{2\pi} E_1(\omega) e^{+i\omega t} \tag{2}$$

The response of the charged oscillator is described by the differential equation

$$\ddot{X}(t) + \Omega^2 X(t) + \frac{2e^2\Omega^2}{3mc^3} \dot{X}(t) = -\frac{e}{m} E_1(t) \tag{3}$$

where X(t) is the separation between the charges, e is the charge magnitude, m is the reduced mass associated with the charges, and Ω is the (angular) resonance frequency.

Introducing the Fourier transform of X(t) through

$$X(t) = \int_{-\infty}^{\infty} \frac{d\omega}{2\pi} X(\omega) e^{+i\omega t} \tag{4}$$

and taking the Fourier transform of Eq. (3), we obtain

$$X(\omega) = \frac{e}{m} \frac{E_1(\omega)}{\omega^2 - \Omega^2 - i\omega\gamma} \tag{5}$$

where

$$\gamma = \frac{2e^2\Omega^2}{3mc^3} \tag{6}$$

The far field of the scattered radiation at a distance R from the oscillator and in a direction perpendicular to its oscillation is given by

$$E_2(R, t) = -\frac{e}{Rc^2} \ddot{X}\left(t - \frac{R}{c}\right) \tag{7}$$

or using Eq. (2)

$$E_2(R, t) = -\frac{e}{Rc^2} \int_{-\infty}^{\infty} \frac{d\omega}{2\pi} \omega^2 X(\omega) e^{+i\omega\left(t - \frac{R}{c}\right)} \tag{8}$$

Here we consider only the scattered field at the same frequency as the incident field; i. e. , Rayleigh scattering. The frequency-shifted fields, arising say from rotation of the oscillator (Raman scattering), can be expected to show the same general time dependence.

Substituting for $X(\omega)$ from Eq. (5) we obtain

$$E_2\left(R, t+\frac{R}{c}\right) = -\frac{1}{R}\left(\frac{e^2}{mc^2}\right)\int_{-\infty}^{\infty}\frac{d\omega}{2\pi}\,\frac{\omega^2 E_1(\omega)e^{+i\omega t}}{\omega^2-\Omega^2-i\omega\gamma} \tag{9}$$

and therefore, the total scattered irradiance at a distance R is given by

$$I_2\left(R, t+\frac{R}{c}\right) = \frac{c}{4\pi R^2}\left(\frac{e^2}{mc^2}\right)^2\left[\int_{-\infty}^{\infty}\frac{d\omega}{2\pi}\,\frac{\omega^2 E_1(\omega)e^{+i\omega t}}{\omega^2-\Omega^2-i\omega\gamma}\right]^2 \tag{10}$$

The angle dependence of this irradiance, which we shall omit in this derivation, is given by $\cos^2\psi$, where ψ is the angle between the polarizations of incident and observed re-emitted light.

Suppose that the scattered radiation is analyzed by a spectrometer (or filter) with passband $S(|\omega|)$. The irradiance of scattered light within this passband is

$$I_2(R, t) = \frac{c}{4\pi R^2}\left(\frac{e^2}{mc^2}\right)^2\left[\int_{-\infty}^{\infty}\frac{d\omega}{2\pi}\,S(|\omega|)\,\frac{\omega^2 E_1(\omega)e^{i\omega t}}{\omega^2-\Omega^2-i\omega\gamma}\right]^2 \tag{11}$$

where we have omitted the time-of-flight delay R/c.

Equations (1), (2) and (10) relate the time dependence of the incident and observed scattered radiation. To examine this dependence for a simple case we assume that the incident light is in the form of a coherent pulse with Gaussian time distribution and pulse length $1/\Delta$; i. e.

$$E_1(t) \propto e^{-t^2\Delta^2/2}\cos\omega_1 t \tag{12}$$

The Fourier transform of this pulse is

$$E_1(\omega) = K\left[e^{-(\omega-\omega_1)^2/2\Delta^2} + e^{-(\omega+\omega_1)^2/2\Delta^2}\right] \tag{13}$$

where K is a normalization constant. It is convenient to express this constant in terms of the energy per unit area J_1 in the incident pulse. Thus

$$K^2 = \frac{4\pi^{3/2} J_1}{c\Delta} \tag{14}$$

Substituting from Eq. (13) into Eq. (10), we obtain

$$I_2(t) = \frac{cK^2}{4\pi R^2}\left(\frac{e^2}{mc^2}\right)^2 \left[\int_{-\infty}^{\infty} \frac{d\omega}{2\pi} S(\omega) \frac{\omega^2 e^{-(\omega-\omega_1)^2/2\Delta^2}}{\omega^2-\Omega^2-i\omega\gamma} e^{i\omega t} + \text{C. C.}\right]^2 \tag{15}$$

where C. C., signifying the complex conjugate of the integral, arises from the second term in Eq. (13). It is apparent from this result that the time dependence of the scattered light is determined by an integral of the form

$$\int_{-\infty}^{\infty} \frac{d\omega}{2\pi} S(\omega) \frac{\omega^2 e^{-(\omega-\omega_1)^2/2\Delta^2}}{\omega^2-\Omega^2-i\omega\gamma} e^{i\omega t} \tag{16}$$

We have not been able to obtain a general closed form expression for this integral. However its qualitative behavior can be inferred from a plot of part of the integrand. Furthermore, Eq. (15) can be solved for several limiting cases. Finally, numerical solutions can easily be obtained using a computer. We will discuss each of these approaches below.

If a wide, constant passband is assumed, $S(\omega)$ may be set equal to one, and the integral in Eq. (15) becomes a Fourier transform of the function

$$F(\omega) = \frac{\omega^2 e^{-(\omega-\omega_1)^2/2\Delta^2}}{\omega^2-\Omega^2-i\omega\gamma} \tag{17}$$

Note that this function is a product of two strongly peaked functions, i. e. ,

$$\frac{\omega^2}{\omega^2-\Omega^2-i\omega\gamma} \quad \text{and} \quad e^{-(\omega-\omega_1)^2/2\Delta^2}$$

A plot of $|F(\omega)|$ is shown in Fig. 4 for the "near-but-off" resonance case. Except for a change in amplitude and slight shift in frequency, this function differs but little from the Gaussian frequency distribution of the incident light. Therefore, in this case we expect the re-emission to follow the time dependence of the incident pulse; i. e. , it will be effectively instantaneous. This

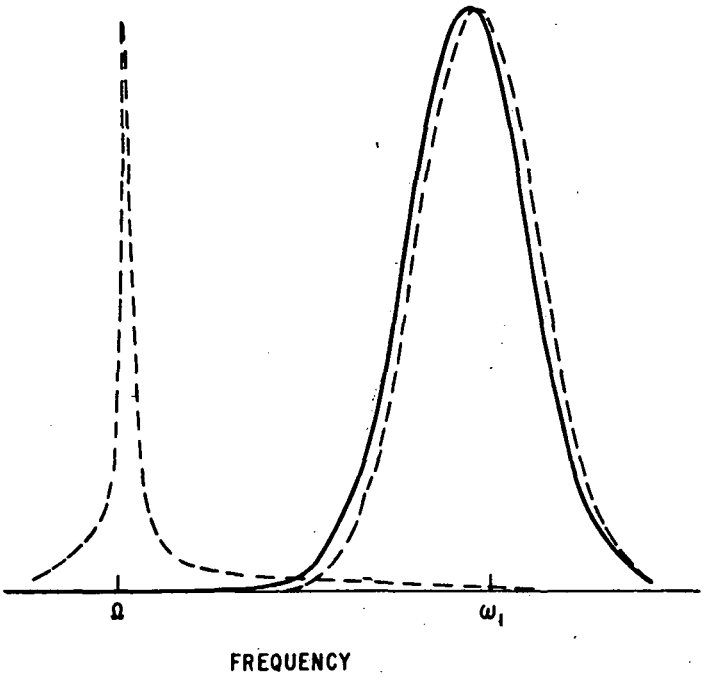

Figure 4 Plot of absolute values of the two peaked functions in $F(\omega)$, and their product, for the "near-but-off-resonance" case. The dashed line mostly to left represents $\text{abs}[\omega^2/(\omega^2-\Omega^2-i\omega r)]$, that mostly to right represents $\exp[-(\omega-\omega_1)^2/2\Delta^2]$, and the solid line represents the normalized product.

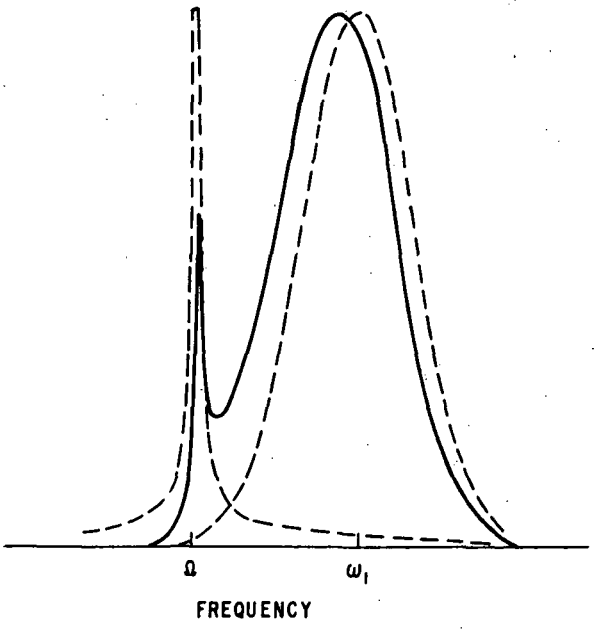

Figure 5 Plot of absolute values of the two peaked functions in $F(\omega)$, and their product, for the "intermediate" (partial overlap) case.

conclusion follows from the fact that in each case (incident and observed scattered light) the time dependence is determined by similar integrals of the frequency dependent function.

In Fig. 5 we show an intermediate case, in which the spectral distribution of the incident radiation substantially overlaps the absorption line. In this case one component of the product closely resembles the Gaussian distribution, but a small second peak appears near the center of the absorption line. Here we expect that the light in the spectral region of the Gaussian will appear as a short pulse, whereas the light centered in the spectral region of the smaller peak will exhibit a slower, quasi-exponential decay. Thus, in this case both scattering and fluorescence appear in the diverted light.

Finally, if the spectral distribution of the incident light is a broad peak centered on a relatively narrow absorption line, corresponding to traditional fluorescence, then the product has nearly the same shape as the absorption line; therefore, in this case the re-emitted light will follow the expected, relatively slow exponential decay of fluorescence.

We may obtain approximate expressions for the magnitudes of fluorescence and scattering for the case of near-but-off resonance by utilizing an approximate form for $F(\omega)$. In this approximation, $F(\omega)$ is replaced by the sum of two functions, in each of which the wing of one peak is evaluated at the center of the other; i. e. ,

$$F(\omega) \simeq \frac{\omega_0^2 \, e^{-(\omega-\omega_0)^2/2\Delta^2}}{\omega_0^2 - \Omega^2 - i\omega\gamma} + \frac{\Omega^2 e^{-(\Omega-\omega_0)^2/2\Delta^2}}{\omega^2 - \Omega^2 - i\omega\gamma} \qquad (18)$$

This approximation can be quite good when the separation from resonance is large compared to Δ, although it breaks down very near resonance. In particular, when the separation from resonance is large compared to both Δ and γ, and $\Delta >> \gamma$, the first term in $F(\omega)$ clearly leads to scattering and the second to fluorescence. We have just argued that both processes may exist simultaneously. It is possible to estimate the absolute magnitudes of each, and their ratio by substituting from Eq. (18) into Eq. (15). We obtain an expression for $I_2(\omega)$ which contains a square of the sum of two integrals, one arising from each term in $F(\omega)$. Cross products of these integrals produced in the squaring operation lead to contributions which "beat", oscillating at a frequency equal to the separation from resonance. This type of beating will be washed out by collision effects and Doppler broadening in most cases. Thus, for present purposes, we drop these terms, leaving two components to I_2; i. e.

$$I_2 = I_{2S} + I_{2f}$$

where

$$I_{2S}(t) = \frac{cK^2}{4\pi R^2}\left(\frac{e^2}{mc^2}\right)^2\left(\frac{\omega_1^2}{\omega_1^2-\Omega^2}\right)^2\left[\int_{-\infty}^{\infty}\frac{d\omega}{2\pi}S(\omega)e^{-(\omega-\omega_1)^2/2\Delta^2}\,e^{i\omega t} + C.\,C.\right]^2 \quad (19)$$

and

$$I_{2f}(t) = \frac{cK^2}{4\pi R^2}\left(\frac{e^2}{mc^2}\right)^2\,\Omega^4 e^{-(\Omega-\omega_1)^2/\Delta^2}\left[\int_0^{\infty}\frac{d\omega}{2\pi}\,S(\omega)\,\frac{e^{i\omega t}}{\omega^2-\Omega^2-i\omega\gamma} + C.\,C.\right] \quad (20)$$

Continuing our assumption of a broad passband ($S(\omega) = 1$), we can easily evaluate these integrals, obtaining

$$I_{2S}(t) = \frac{J_1\Delta}{\sqrt{\pi}R^2}\left(\frac{e^2}{mc^2}\right)^2\left(\frac{\omega_1^2}{\omega_1^2-\Omega^2}\right)^2 e^{-\Delta^2t^2} \quad (21)$$

and

$$I_{2f} = \frac{2\,J_1\Omega^2}{\sqrt{\pi}R^2\Delta}\left(\frac{e^2}{mc^2}\right)^2 e^{-(\Omega-\omega_1)^2/\Delta^2}\;e^{-\gamma t}\;,\quad t\geq 0 \quad (22)$$

$$= 0,\quad t < 0.$$

It is clear that I_{2S} follows the time dependence of the incident pulse, while I_{2f} shows the exponential decay of fluorescence. Integrating over time we obtain the total energy (per unit area) in each component:

$$J_{2S} = \frac{J_1}{R^2}\left(\frac{e^2}{mc^2}\right)^2\left(\frac{\omega_1^2}{\omega_1^2-\Omega^2}\right)^2 \quad (23)$$

$$J_{2f} = \frac{2\,J_1\Omega^2}{\sqrt{\pi}R^2\Delta\gamma}\left(\frac{e^2}{mc^2}\right)^2 e^{-(\Omega-\omega_1)^2/\Delta^2} \quad (24)$$

The results for the fluorescence components $I_{2f}(t)$ and J_{2f} are of mostly academic interest, since typically these will be significant only near the limit of applicability of the approximation, and there they are likely to be very sensitive to inhomogeneous pressure and Doppler broadening, whose effects we have not included.

However, the results for the scattering component, $I_{2S}(t)$ and J_{2S} are of practical interest, because they remain significant far from resonance where the approximation is very good. If Eq. (23) is multiplied by the angle-dependent factor appropriate to this simple model, $\cos^2\psi$, summed over

polarization and integrated over the area of the sphere at distance R, the total scattered energy is obtained in the form

$$Q_2 = \frac{8\pi}{3} J_1 \left(\frac{e^2}{mc^2}\right)^2 \left(\frac{\omega_1^2}{\omega_1^2 - \Omega^2}\right)^2 \tag{25}$$

Defining a scattering cross section

$$\sigma_T = \frac{Q_2}{J_1} \tag{26}$$

and employing the near-resonance approximation

$$\left|\omega_1^2 - \Omega^2\right|^2 \simeq 4\Omega^2 (\omega_1 - \Omega)^2 , \quad \omega_1 = \Omega \tag{27}$$

we obtain

$$\sigma_T = \frac{2\pi}{3}\left(\frac{e^2}{mc^2}\right)^2 \left(\frac{\omega_1}{\omega_1 - \Omega}\right)^2 . \tag{28}$$

It is interesting to compare Eq. (28) with the quantum mechanical result presented subsequently in Eq. (45). Except for numerical factors which are near unity for strong transitions, they are the same.

So far we have discussed the time dependence of $I_2(t)$ through qualitative arguments and limiting cases. Now, to be more precise, we consider a direct numerical solution for $I_2(t)$ under conditions which are in the transition zone between limiting cases. Starting with Eq. (15), we first put it into a more convenient form for computer integration.

Let

$$J(\omega) = \left[\frac{cK^2}{\pi R^2}\right]^{1/2} \left(\frac{e^2}{mc^2}\right) S(\omega) \left(\frac{\omega^2 e^{-(\omega-\omega_0)^2/2\Delta^2}}{\omega^2 - \Omega^2 - i\omega\gamma}\right) \tag{29}$$

Then

$$I_2(t) = \left| \int_{-\infty}^{\infty} \frac{d\omega}{2\pi} J(\omega)\, e^{i\omega t} \right|^2 \tag{30}$$

neglecting unmeasurable high frequency components. It is convenient to take explicit account of a detector response in order to limit the necessary computer operations; therefore, let us define $R(t, t')$ to be the response of a detector at time t to a signal at time t'. Then the detector signal will be

$$Z(t) = \int_{-\infty}^{t} R(t, t')\, I_2(t')dt' \tag{31}$$

Substituting for $I_2(t)$ from Eq. (30) and writing out the absolute square, we obtain

$$Z(t) = \int_{-\infty}^{t} dt' R(t, t') \int_{-\infty}^{\infty} \frac{d\omega d\omega'}{4\pi^2} J^*(\omega) J(\omega') e^{i(\omega' - \omega)t'} \tag{32}$$

Introducing $\alpha = \omega' - \omega$ and inverting the order of integration, we may put this equation into the form

$$Z(t) = \int_{-\infty}^{\infty} \frac{d\omega d\alpha}{4\pi^2} J^*(\omega)\, J(\omega+\alpha) \int_{-\infty}^{t} dt' R(t, t') e^{i\alpha t'} \tag{33}$$

Now suppose that the detector response is exponential; then

$$R(t, t') = \frac{1}{\tau} e^{-(t-t')/\tau} \quad , \; t > t'; = 0, \quad \text{otherwise} \tag{34}$$

and, performing the integration over t', we obtain

$$Z(t) = \frac{1}{4\pi^2} \int_{-\infty}^{\infty} d\alpha \, \frac{e^{i\alpha\tau}}{1+i\alpha\tau} \int_{-\infty}^{\infty} d\omega \, J^*(\omega)\, J(\omega+\alpha) \tag{35}$$

It is convenient to define the correlation function

$$G(\alpha) = \int_{-\infty}^{\infty} d\omega \, J^*(\omega)\, J(\omega+\alpha) \tag{36}$$

Then note $G(-\alpha) = G^*(\alpha)$. Using this property and the fact that the J's are negligible for negative values of ω, we can write Eq. (35) in the form

$$Z(t) = \frac{1}{2\pi^2} \Re \left\{ \int_{0}^{\infty} d\alpha \, \frac{e^{i\alpha\tau}}{1+i\alpha\tau} \, G(\alpha) \right\} \tag{37}$$

where the symbol $\Re$ denotes the real part of the integral.

In the computer calculation the correlation function $G(\alpha)$ is first calculated. This operation is facilitated by the fact that the J's are significant over only a small spectral region. Furthermore, large values of α do not have to be considered because of the denominator in the α-integral. After calculation of the correlation function, a fast Fourier transform routine is used to obtain $Z(t)$ and this function is displayed by a digital plotter. The results obtained over a representative range of conditions are shown in Fig. 6. The transition from delayed to instantaneous re-emission in the simple case considered is quite evident.

A quantum mechanical analysis of the time dependence of re-emission from a molecule following pulsed excitation has been developed by Seth D. Silverstein (see Appendix C). In this analysis the light pulse is represented by a propagating coherent wave packet of the type introduced by Glauber (ref. 17). The results confirm those of the classical approach described above.

Relevant conclusions can be drawn from these results along what might be considered as three levels of conjecture. First we consider pulsed excitation of a gas at sufficiently low pressure such that interactions between molecules can be neglected. In this situation the distinction between scattering and fluorescence concerns only the time dependence of the re-emission. The behavior of the classical model implies that "instantaneous" re-emission (i. e., scattering) will be observed when the separation from resonance is several times larger than the widths of the excitation and absorption lines. We have not included the line shifts resulting from particle motion in this analysis. However, the resulting Doppler broadening falls off extremely rapidly in the line wings, such that we may conclude that scattering will be observed under the condition described above providing the absorption line width is considered to include the Doppler broadening.

At the second level of conjecture, we consider the effect of particle interactions on the re-emission as the pressure is increased. At STP, the mean time between collisions τ_c for small molecules is on the order of 10^{-10} sec., whereas the duration of a collision is on the order of 10^{-11} to 10^{-12} sec. If we may regard a molecule as "isolated" in between collisions, then the results of the classical model apply. However, in this case the interaction between molecule and light must occur in a time short compared to τ_c, which necessitates that the spectral width of the exciting pulse be large in comparison to the collision broadening width

$$\gamma_c \simeq 1/\tau_c$$

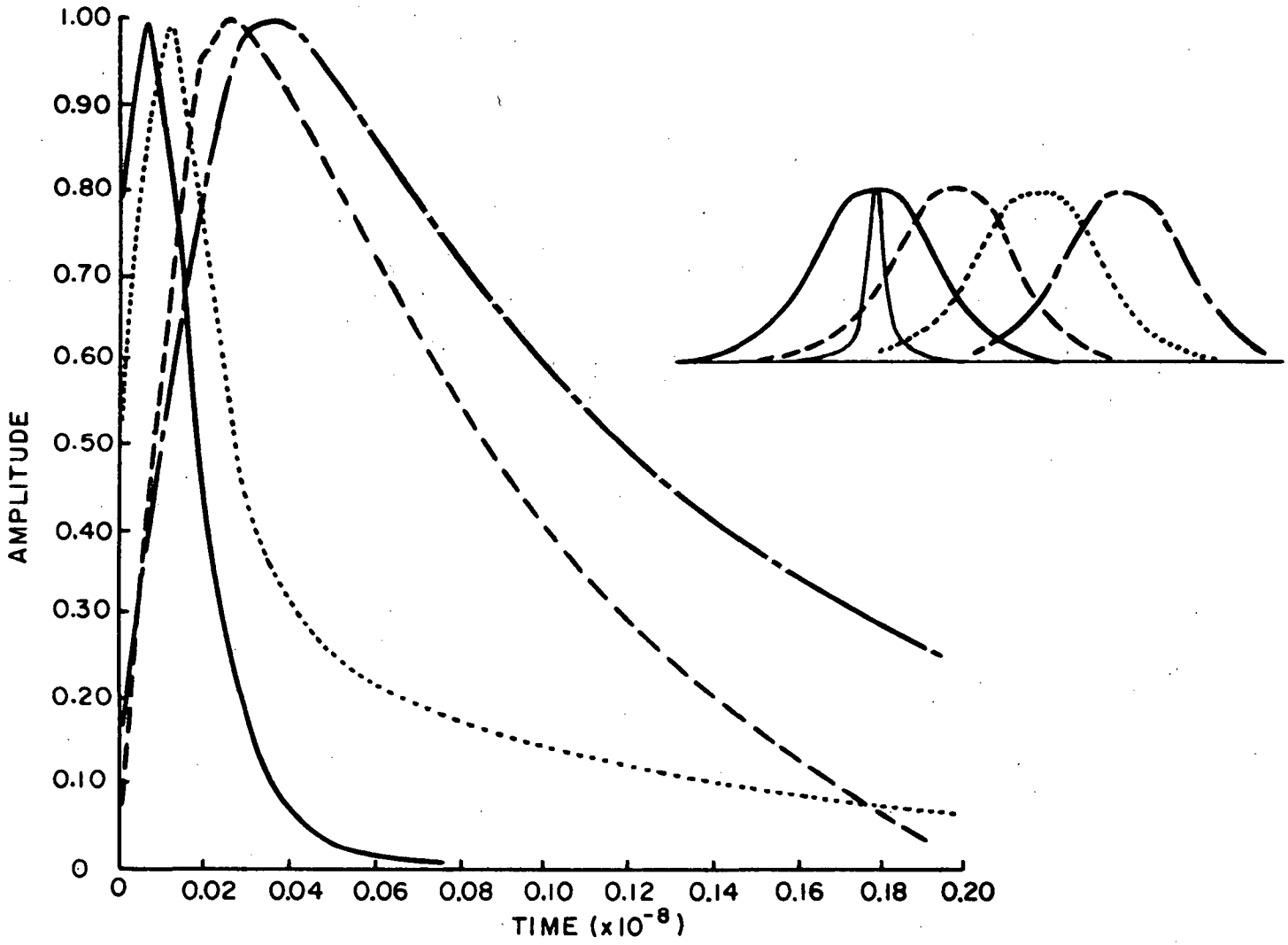

Figure 6 Plots of the time-dependence of detector responses for a short incident light pulse and consequent light re-emission from a charged oscillator, as a function of separation from resonance. The assumed spectral distributions of incident light and absorption line for each case are shown in the upper right corner. The re-emission time dependence overlays the incident pulse (solid line) for the off-resonance (no overlap) case. Pulses are displaced from zero by the finite detector response.

This condition, when coupled with that of no overlap, suggests that scattering will be observed when the separation from resonance is much larger than the collision broadening width of the absorption line. Here also, we must consider Doppler broadening, and in addition, we must consider the absorption line shifts introduced by the fields of interacting molecules. The statistical distribution of these fields introduces a so-called inhomogeneous broadening which has the effect of shifting some molecules into resonance. Whenever the contribution of these molecules to the re-emission is significant, it will display characteristics of fluorescence. This type of broadening is often called "statistical broadening" (ref. 12). It will be discussed in somewhat more detail subsequently. However, we note that statistical broadening does not necessarily fall off as fast as Doppler broadening in the line wings. Hence its effect can extend much farther from resonance. The detailed theory of statistical line broadening in the far wings of a line is difficult, and so far incomplete, prohibiting definite conclusions about the transition from scattering to fluorescence. On the other hand, our arguments suggest that experimental observations of this transition might provide valuable information about the broadening processes.

Finally, at the third level of conjecture, we consider excitation by monochromatic (and hence continuous, rather than pulsed) radiation. In this case, the distinction between fluorescence and scattering can be made only on the basis of sensitivity to collision effects (within the criteria adopted in this report). The classical analysis developed previously bears no obvious application to this case. Indeed, in order to relate the quenching of monochromatic excitation to a temporal behavior of re-emission, we would have to consider individual absorption events, which are distinctly quantum-mechanical in nature. Consequently, we believe that the transition from scattering to fluorescence in the case of monochromatic excitation is properly treated only by a quantum-mechanical analysis of intermolecular effects in the far wings of an absorption line. Such an analysis is not yet available in the literature, and is regarded as beyond the scope of this investigation. However, in its absence it is tempting to speculate that quenching of monochromatic radiation will not differ substantially from that of broad band radiation centered at the same wavelength, provided there is no significant overlap of the latter with the absorption line.

If this and previous speculations are correct, the transition from scattering to fluorescence should occur at a separation from resonance several times larger than the absorption line width, the emission linewidth or the range of significant inhomogeneous broadening, whichever is larger. However, we do not consider this general conclusion to be firmly established. Preliminary indications from a different, quantum analysis suggest that it should be regarded with healthy skepticism until tested by additional theoretical analysis and experiments.

Simple Quantum Mechanical Calculations

In this section we use relatively simple quantum-mechanical results for scattering and fluorescence to draw some useful conclusions about these phenomena. The basic quantum-mechanical expression for a differential light scattering cross section can be written in the form

$$(\sigma_{12})_{n\to f} = \frac{\omega_2^4}{c^4\hbar^2}\left|\sum_r \frac{(D_2)_{fr}(D_1)_{rn}}{\omega_{rn}-\omega_1+i\gamma_r/2} + \frac{(D_1)_{fr}(D_2)_{rn}}{\omega_{rf}+\omega_1-i\gamma_r/2}\right|^2 \qquad (38)$$

Here D_1 and D_2 are components of the dipole moment vector in the directions of unit vectors $\hat{\epsilon}_1$ and $\hat{\epsilon}_2$ which designate the directions of polarization of incident and scattered light, respectively; e. g.

$$D_1 \equiv \tilde{D} \cdot \hat{\epsilon}_1$$

The symbol $(D_1)_{rn}$, for example, designates a matrix element of D_1 between the initial state n and an intermediate state r, and $\omega_{rn} \equiv \omega_r - \omega_n$, where $\hbar\omega_r$ is the energy of the state r. The quantity γ_r is the line width for the state r. To correspond to a practical case this cross section must be averaged over the distribution of initial states (n) of molecules (atoms) under observation and, for each initial state, it must be summed over all final states (f) which correspond to scattering in the spectral range of interest.

The cross section is defined such that the intensity (watts/steradian) of light scattered per molecule in corresponding transitions and with appropriate polarizations is given by

$$\mathcal{I}_2 = \sigma_{12} I_1 \qquad (39)$$

where I_1 is the incident irradiance (watts/m^2).

Simplification near resonance. - Sufficiently near resonance, one or a few terms in the sum over r in Eq. (38) will often predominate. Unless the gas is highly excited, these terms must be of the first type; i. e. , with denominators of the form $\omega_{rn} - \omega_1 + i\gamma_r/2$. In such cases, if only one intermediate state is involved for each initial-final state pair, we may write the cross section in the form

$$(\sigma_{12})_{n\to f} = \frac{\omega_2^4}{c^4\hbar^2}\,\frac{\left|(D_2)_{fr}\right|^2\left|(D_1)_{rn}\right|^2}{(\omega_{rn}-\omega)^2+\gamma_r^2/4} \qquad (40)$$

In particular, the total cross section, that is, the cross section integrated over all scattering angles, and summed over scattered light polarizations, is given by

$$\sigma^T_{n\to f} = \frac{8\pi}{9}\,\frac{\omega_s^4}{c^4\hbar^2}\,\frac{\left|D_{fr}\right|^2\left|D_{rn}\right|^2}{(\omega_{rn}-\omega)^2+\gamma_r^2/4} \tag{41}$$

where $|D_{rf}|^2$ designates the absolute square of the vector matrix element; i. e.,

$$\left|D_{rf}\right|^2 \equiv \tilde{D}_{rf}\cdot\tilde{D}_{rf} = \sum_{k=x,\,y,\,z}\left|(D_k)_{rf}\right|^2 \tag{42}$$

Note that the absorption oscillator strength for the transition $n\to r$ is defined by

$$f_{rn} = \frac{2m\,\omega_{rn}}{3\,e\,\hbar}\left|D_{rn}\right|^2 \tag{43}$$

Thus we obtain for the total cross section

$$\sigma^T_{n\to f} = \frac{2\pi\,\omega_2^4}{\omega_{rn}\,\omega_{rf}\left[(\omega_1-\omega_{rn})^2+\gamma_r^2/4\right]}\left(\frac{e^2}{mc^2}\right)^2 f_{rn}\,f_{rf} \tag{44}$$

In this derivation we have excluded consideration of degeneracy arising from various orientations of the total angular momentum of the molecule. Fortunately, it is possible to include this ubiquitous type of degeneracy rigorously. Averaging over initial orientations (magnetic quantum numbers) and summing over final orientations, we find that the result is σ^T as given by Eq. (44), multiplied by g_f/g_r, where the g's are the state orientation degeneracies associated with the total angular momentum J; e. g.

$$g_r = 2J_r + 1$$

The near resonance approximations $\omega_{rn} = \omega_1$ and $\omega_{rf} = \omega_2$ can be used to write Eq. (44) in the form

$$\sigma^T_{n\to f} = 2\pi\,\frac{g_f}{g_r}\left(\frac{\omega_2}{\omega_1}\right)^3\left(\frac{e^2}{mc^2}\right)^2\left(\frac{\omega_1}{\omega_1-\omega_{rn}}\right)^2 f_{rn}\,f_{rf} \tag{45}$$

where we have neglected the linewidth γ_r. It is interesting to note that this differs from the classical result of Eq. (28) only by the factor

$$3 \frac{g_f}{g_r} \left(\frac{\omega_2}{\omega_1}\right)^3 f_{rn} f_{rf} \tag{46}$$

which is near unity for a strong transition.

Comparison of Expressions for Scattering and Fluorescence. - Using Eq. (41), we can write an expression for the rate R_{sc} at which photons are scattered per molecule in an incident beam of irradiance I_1 (watts/m^2). Thus

$$R_{sc} = I_1 \sum_f{}' \frac{\sigma^T_{n\to f}}{\hbar \omega_2} \tag{47}$$

where $\omega_2 = \omega_1 - \omega_{fi}$ and the sum over f extends over all final states for which $\omega_2 > 0$. Substituting from Eq. (41) for the cross section, we obtain

$$R_{sc} = I_1 \frac{8\pi}{9 c^4 \hbar^3} \frac{|D_{rn}|^2}{(\omega_{rn}-\omega_1)^2 + \gamma_r^2/4} \sum_f{}' (\omega_1-\omega_{fi})^3 \left| D_{fr} \right|^2 \tag{48}$$

The radiation linewidth γ_r is given by

$$\gamma_r = \frac{4}{3} \sum_f{}' \frac{\omega_{rf}^3}{\hbar c^3} \left| D_{fr} \right|^2 \tag{49}$$

This result and the near resonance approximation

$$\omega_{rf} \cong \omega - \omega_{fi}$$

can be substituted into Eq. (48) to obtain

$$R_{sc} = I_1 \frac{4\pi^2}{3 c \hbar^2} \left| D_{rn} \right|^2 \frac{\gamma_r/2\pi}{(\omega_{ri}-\omega_1^2)^2 + \gamma_r^2/4} \tag{51}$$

But this expression is equal to that for the rate at which photons are absorbed, given by first order perturbation theory, and therefore it is also equal to the rate of R_F of fluorescence in the absence of collision effects. This result suggests that Eq. (38) describes both scattering and fluorescence in the

absence of collisions. In this sense, scattering and fluorescence can be regarded as the same phenomenon in different behavior regimes, as already suggested by the classical analysis. However, in actual experimental situations, inhomogeneous broadening and multiplicity of intermediate levels can lead to a variety of conditions, such that both fluorescence and scattering can appear simultaneously upon excitation near resonance. Furthermore, we must consider processes in which re-radiation excited in an absorption region is terminated quickly by an internal process such as dissociation. In such cases this radiation can display the properties of scattering, even though excited "on resonance. "

Ratio of Scattering Excited Near Resonance to (Quenched) Fluorescence Excited on Resonance. - An estimate of this ratio is useful for experimental purposes; for example, one must consider the fluorescence excited by light in the wings of the spectral distribution of quasi-monochromatic incident light in comparison to scattering excited on line center. This estimate also sets the stage for later considerations of excitation within the wings of an absorption line. We develop this estimate in terms of the integrated absorption coefficient K, defined as follows. If the transmission of a monochromatic beam of light through length ℓ of a gas is given by

$$T = e^{-k(\omega)p\ell}$$

where p is the pressure in atmospheres (referred to STP), then (ref. 12)

$$K \equiv \int k(\omega)d\omega = 2\pi^2 c\left(\frac{e^2}{mc^2}\right) N_0 F_r f_{rn} \tag{52}$$

Here the integral extends over the line, N_0 is the number density of molecules at STP and F_r is the fraction of those molecules in the initial state r. An approximate value for $k(\omega)$ at its maximum can be obtained by dividing this integral by the total linewidth Γ (including collision broadening). This maximum value can be equated to $N_0 F_n(\sigma_a)$ peak, where (σ_a) peak is effective the absorption cross section at line center. Thus we obtain

$$(\sigma_a)_{peak} \simeq \frac{2\pi^2 c}{\Gamma}\left(\frac{e^2}{mc^2}\right) f_{rn} \tag{53}$$

The probability that the absorbed light will be re-emitted in a transition r→f (before quenching) is

$$P_E \simeq \gamma_{rf}/\nu_c \Phi . \tag{54}$$

providing quenching is the dominant decay mechanism ($\nu_c \Phi >> \gamma_r$). Here γ_{rf} is the transition probability per unit time for a radiating transition r→f, γ_r

is the total radiation probability per unit time, ν_c is the collision frequency and Φ is the probability of quenching per collision. Note

$$\gamma_{rf} = \frac{2\omega^2_{rf} f_{rf}}{c}\left(\frac{e^2}{mc^2}\right) \tag{55}$$

Therefore

$$P_E = \frac{2\omega^2_{rf} f_{rf}}{c\nu_c \Phi}\left(\frac{e^2}{mc^2}\right) \tag{56}$$

The total cross section for fluorescence re-emission in the transition r→f is then

$$(\sigma_f)_{peak} = (\sigma_a)_{peak} P_E = \frac{4\pi^2 \omega^2_{rf}}{\Gamma \nu_c \Phi}\left(\frac{e^2}{mc^2}\right)^2 f_{rn} f_{rf} \tag{57}$$

Assuming that the line broadening is dominated by quenching, we set

$$\nu_c = \Gamma/2$$

Then

$$(\sigma_f)_{peak} = \frac{8\pi^2\omega^2_{rf}}{\Gamma^2 \Phi}\left(\frac{e^2}{mc^2}\right)^2 f_{rn} f_{rf} \tag{58}$$

The ratio of the cross section for re-emission excited off resonance, given by Eq. (45), to the peak re-emission as given by Eq. (58) is

$$\frac{\sigma_{NRRS}}{(\sigma_f)_{peak}} = \left(\frac{\omega_{rf}}{\omega_{rn}}\right)\frac{\Phi}{4\pi}\left(\frac{\Gamma}{\Delta\omega}\right)^2 \tag{59}$$

where $\Delta\omega$ is the separation from resonance. To recapitulate, the following assumptions were made in deriving Eq. (59):

(a) Quenching is the dominant de-excitation mechanism.

(b) Simple Lorentz collision broadening model is applicable.

(c) Collisions are the dominant broadening mechanism.

If we assume, moreover, that NRRS is observed at a separation from resonance equal to 10 times the linewidth Γ, and $\Phi \simeq 1$, then

$$\frac{\sigma_{NRRS}}{(\sigma_f)_{peak}} \simeq 10^{-3} \qquad (60)$$

Actually, the effects of inhomogeneous broadening may reach out to a further separation than 10 Γ, in which case Eq. (60) is a high estimate. Nevertheless it illustrates that where a discrete strong absorption line is involved, such that the (quenched) fluorescence is likewise strong, there is a good chance that NRRS will be observed.

Near Resonance Raman Scattering From Atoms

Previously, we have used a slightly more detailed version of Eq. (45), which includes the angle and polarization dependence of the scattering, to calculate the electronic Raman scattering cross sections for the following group of atoms: boron, aluminum, gallium, indium and thallium. This series is characterized by low-lying excited electronic states and accessible higher states through which RS can proceed. These properties are evident from the level diagrams shown in Fig. 7. The NSSR cross sections calculated for aluminum atoms (ref. 18) which are shown in Fig. 8, are typical of the group. It is significant that an enhancement of about 10^8 over N_2 vibrational RS is predicted at separations from resonance on the order of 1 nm. The corresponding Raman shift near resonance is about 2 nm. Although an experiment appears feasible to verify this strong re-emission, and to determine whether or not its characteristics are those of scattering, none has yet been reported to our knowledge.

Near Resonance Raman Scattering From Molecules

In the situation discussed above, the oscillator strengths are large (~1) and the absorption lines distinct and well separated. For molecules the situation for this type of NRRS is generally less favorable. Typically, molecule absorption lines are closely spaced, individual line oscillator strengths are much smaller and, as a rule, only a moderate fraction of molecules are in initial states which contribute to a particular absorption line. Thus we are led to consider NRRS in proximity to an absorption band, rather than to a line. Typical bands of interest for the molecules O_3, SO_2, and NO (refs. 19, 20, 21) are shown in Fig. 9 a, b and c.

There is a complication in the calculation of NRRS from a band, because within the absolute square in Eq. (38), some of the terms in the sum over intermediate states (r) may be positive and others negative, producing interference effects. (In the general case, these terms can be complex with various phases.) These effects are discussed in somewhat more detail in Appendix B. However, at a separation from resonance which is large

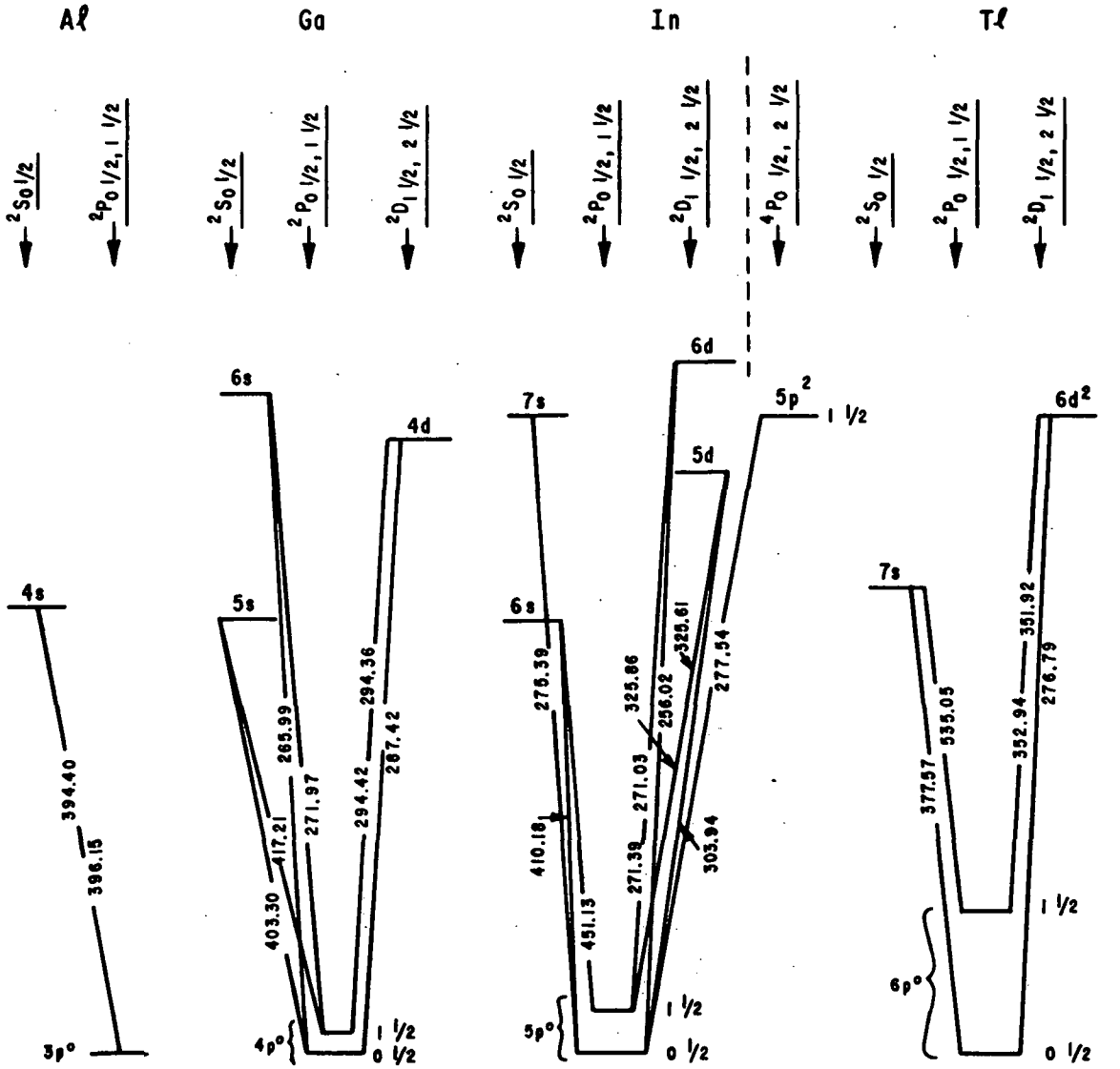

Figure 7 Level diagrams for aluminum, gallium, indium and thallium, showing transitions which lead to shifted re-emission (Raman scattering or fluorescence).

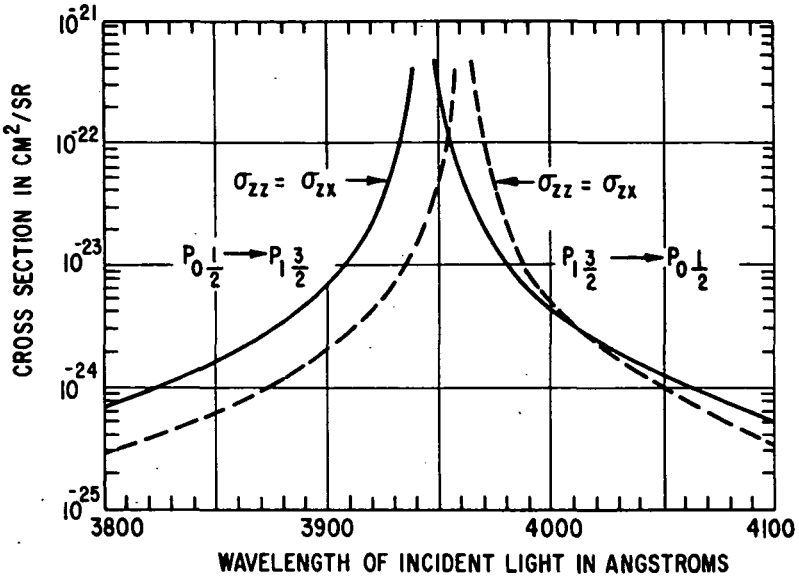

Figure 8 Re-emission cross sections for aluminum calculated from oscillator strengths. The cross sections σ_{zz} corresponds to re-emission with polarization parallel to that of incident light, whereas σ_{zx} corresponds to re-emission with polarization perpendicular to that of incident light.

compared to the width of the nearest band, but small compared to the separation between bands, it can be shown that these interference effects are negligible, such that the contribution of the band to scattering is proportional to its overall strength. Thus, for a first approximation, we estimate NRRS cross sections on this basis. Assuming that the initial and final electronic states are the same, and neglecting rotational structure, we write Eq. (45) in the form

$$\sigma_{12}^{T} = 2\pi\left(\frac{\omega_2}{\omega_1}\right)^3\left(\frac{\omega_1}{\omega_1-\omega_R}\right)^2 f^2\left(\frac{e^2}{mc^2}\right)^2 \sum_{n,\,r} P_n |\langle r|n\rangle|^2 |\langle r|f\rangle|^2 \qquad (61)$$

Here f is the electronic absorption oscillator strength, P_n is the fractional occupation of the vibrational state n, and $|\langle r|f\rangle|^2$, for example, is the overlap integral between vibrational states r and f. The effective resonance frequency is denoted simply by ω_R. The overlap integrals are normalized such that

$$\sum_{a} |\langle a|b\rangle|^2 = 1$$

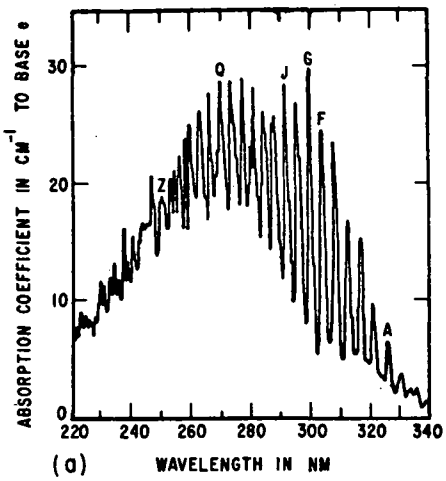

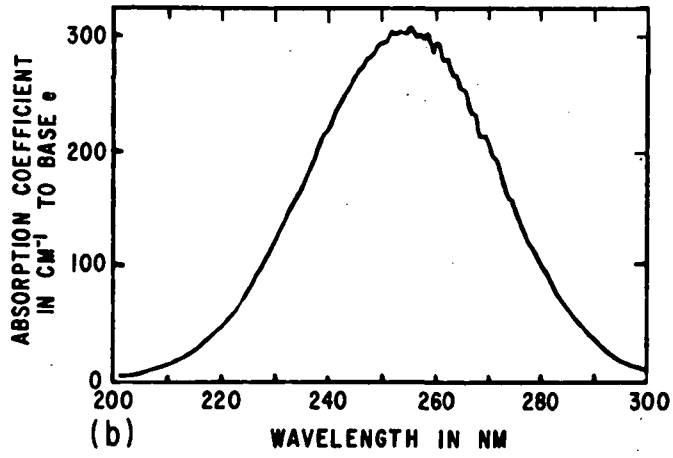

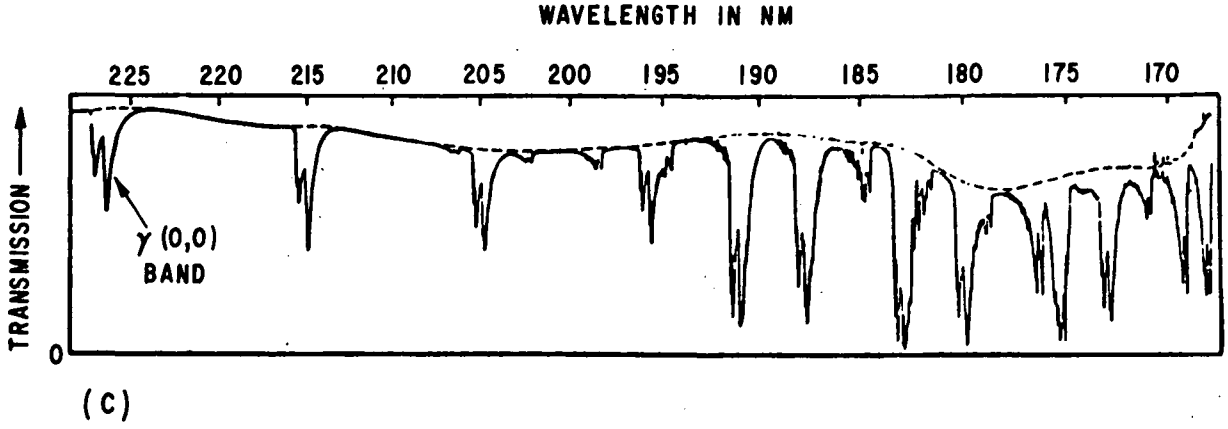

Figure 9 Ultraviolet absorption bands of (a) SO_2, (b) O_3, and (c) NO, partially derived from information in refs. 19, 20 and 21.

Summing Eq. (61) over all final states f, we find that the sum over r can then be completed, and the cross section for Rayleigh plus vibrational Raman scattering becomes

$$\sigma^T = 2\pi\left(\frac{\omega_2}{\omega_1}\right)^3\left(\frac{\omega_1}{\omega_1 - \omega_R}\right)^2 f^2 = 2\pi\left(\frac{\nu_2}{\nu_1}\right)^3\left(\frac{\nu_1}{\nu_1-\nu_R}\right)^2 f^2 \qquad (62)$$

where the second equality has been expressed in terms of wave numbers (e.g., $\nu_1 = \omega_1/2\pi c$). The integrated absorption coefficient for the band (here integrated over wave numbers ν) is

$$K = \pi\left(\frac{e^2}{mc^2}\right) N_0 f \qquad (63)$$

where again N_0 is the molecule number density at STP. Thus we obtain

$$\sigma^T = \frac{2}{\pi N_0^2}\left(\frac{\nu_2}{\nu_1}\right)^3\left(\frac{\nu_1}{\nu_1-\nu_R}\right)^2 K^2. \qquad (64)$$

We can write the integrated absorption coefficient in the form

$$K = \langle k \rangle \, \delta\nu$$

where $\langle k \rangle$ is the average monochromatic absorption coefficient and $\delta\nu$ is the bandwidth. Then

$$\sigma^T \simeq \frac{2}{\pi N_0^2}\,\frac{\nu_2^3}{\nu_1}\left(\frac{\delta\nu}{\nu_1 - \nu_R}\right)^2 \langle k \rangle^2 \qquad (65)$$

Previously, we assumed that near-resonance scattering would be observed at a separation from resonance equal to ten times an absorption line width. Since a typical bandwidth will be much greater than the width of a single line, we assume here that scattering will be observed at a separation from resonance equal to the bandwidth. Then

$$\sigma^T = \frac{2}{\pi N_0^2}\,\frac{\nu_2^3}{\nu_1}\,\langle k \rangle^2 \qquad (66)$$

Now, noting that $N_0 = 2.69 \times 10^{19}$ molecules/cm^3 at STP and that ν_1 and ν_2 are approximately 3×10^4 cm^{-1} for incident wavelengths near 300 nm, we obtain

$$\sigma^T(\text{cm}^2) \simeq 10^{-30}\,\langle k \rangle^2 \qquad (67)$$

for this near UV spectral region, where k is in units of cm^{-1} atm^{-1} to base e and referred to STP. Equation (67) can be used along with the results for SO_2

and O_3 shown in Fig. 9 to obtain an estimate of the enhancement, if any, of the scattering from these molecules. Of course, in general the effects of limited resolution (spectrometer pass band wider than individual absorption linewidths) must be carefully considered in determining $\langle k \rangle$ from absorption measurements. However, the absorption bands for SO_2 and O_3 in Fig. 9 have been shown to be quasicontinuous by high resolution measurements. Thus we can take values of $\langle k \rangle$ directly from these figures. For SO_2 we obtain

$$\langle k \rangle \simeq 20 \text{ cm}^{-1} \text{ atm}^{-1}$$

and

$$\sigma^T \simeq 4 \times 10^{-28} \text{ cm}^2.$$

But the value of σ_T for Rayleigh plus Raman scattering from SO_2 extrapolated from measurements in the visible is several orders of magnitude larger. Thus this estimate suggests that there will be no significant enhancement of the scattering from SO_2 under the near-resonance conditions assumed for this example.

For O_3

$$\langle k \rangle \simeq 200 \text{ cm}^{-1} \text{ atm}^{-1}.$$

In this case Eq. (67) provides the estimate

$$\sigma^T \simeq 4 \times 10^{-26} \text{ cm}^2$$

which is approximately equal to the extrapolated cross section. Thus little enhancement of the total scattering is predicted, although Raman scattering may be moderately enhanced if the Raman-to-Rayleigh ratio increases.

A NRRS cross section can be estimated similarly for NO, using integrated absorption coefficients measured by Bethke (ref. 21). For the longest wavelength absorption band, $\gamma(0,0)$, we obtain

$$\langle k \rangle \simeq 30 \text{ cm}^{-1} \text{ atm}^{-1}$$

and

$$\sigma^T \simeq 10^{-27} \text{ cm}^2$$

This value is about two orders of magnitude smaller than the extrapolated total cross section for NO at 226.5 nm (1.6×10^{-25} cm^2). Therefore in this case there appears to be little hope of useful enhancement.

Alternatively, Eq. (45) can be used to estimate the NRRS for incident light at, say, 250 nm. In developing this estimate, we simply sum the contributions from the various bands listed by Bethke algebraically, neglecting interference effects which might make the actual cross section substantially larger (or smaller) than estimated. We obtain

$$\sigma^T \simeq 3.6 \times 10^{-28} \text{ cm}^2$$

which is orders of magnitude less than the extrapolated cross section.

Thus the cases considered here are unlikely to produce strongly enhanced scattering. However, in later sections of this report we will point out more promising situations.

Approach to Resonance - Excitation within the Broadened Line. - When the exciting wavelength is tuned toward the center of a pressure broadened absorption line, at some point interactions between gas molecules will begin to have a significant affect on the re-emitted light. In particular, there are spectral regions where pressure broadening and quenching have comparable opposite effects on the intensity of this light, such that the intensity per molecule can be insensitive to pressure over a broad pressure range.

This phenomenon can be explained within the context of the Lorentz line-broadening theory, following an analysis similar to those developed in refs. 11 and 22. The absorption cross section in the presence of Lorentz broadening is given by

$$\sigma_a = \left[\frac{\pi^2 c^2 \gamma_{rn}}{\omega_{rn}^2}\right]\left[\frac{\Gamma/2\pi}{(\omega_1-\omega_{rn})^2 + \Gamma^2/4}\right] \tag{68}$$

Here γ_{rn} is the probability per unit time for the radiating transition r→n, and Γ is the total width of the upper level r. The effective cross section for light re-emission associated with the molecular transition r→f is given by the product of the absorption cross section and the probability P_L that the transition r→f will occur before some other event (e. g. collision or radiation) alters the state of excitation; thus

$$\sigma_L = \frac{\omega_2}{\omega_1} \sigma_a P_L \tag{69}$$

Here the subscript L indicates re-emission into a particular line.

It is possible to derive a simple expression for P_L if one assumes that the various decay rates associated with the excited state r are independent of the excitation frequency. The probability per unit time of decay by radiation is γ. Non-collisional decay by processes such as dissociation and predissociation can occur in some cases; the probability rate for these processes will be designated by Γ_D. Collisions induce decay by quenching, at a probability rate Γ_Q. Elastic collisions make a contribution Γ_E to line broadening, and other collisions produce small changes in the excitation energy at a rate Γ_B, typically creating a broad band of fluorescence upon which the various lines are superimposed. Thus the total linewidth is given by

$$\Gamma = \gamma + \Gamma_D + \Gamma_E + \Gamma_B + \Gamma_Q$$

If the rate of excitation is R, then the steady state population N_r of molecules in state r is given by

$$R = \gamma_{rf} N_r + (\gamma - \gamma_{rf}) N_r + \Gamma_D N_r + \Gamma_B N_r + \Gamma_Q N_r = (\Gamma - \Gamma_e) N_r$$

Here we assume that repopulation of state r by collisions is negligible. Then the probability of decay by re-emission r→f is given by the ratio of this rate to all decay rates; i. e. ,

$$P_L = \frac{\gamma_{rf}}{\Gamma - \Gamma_E} \tag{70}$$

Likewise, if we assume that the various decay rates for all excited states are equal, the probability of decay by re-emission into the broad continuum following excitation of state r is

$$P_B = \frac{\Gamma_B}{\Gamma - \Gamma_e} \frac{\gamma}{\gamma + \Gamma_Q + \Gamma_D}$$

From Eqs. (68), (69) and (70), we obtain for the line fluorescence

$$\sigma_L = \frac{\pi^2 c^2 \gamma_{rn} \omega_2}{\omega_1^3} \left[\frac{\Gamma/2\pi}{(\omega_1 - \omega_{rn})^2 + \Gamma^2/4} \right] \left[\frac{\gamma_{rf}}{\Gamma - \Gamma_E} \right] \tag{71}$$

This result leads to interesting predictions, for if collision broadening and quenching predominate, then to a good approximation

$$\Gamma_E = \epsilon p$$
$$\Gamma_Q = qp$$
$$\Gamma = \kappa p$$

where p is pressure and ϵ, q and κ are appropriate proportionality constants. Substituting the first and last of these results into Eq. (71) we obtain

$$\sigma_L = \frac{\pi^2 c^2 \gamma_{rn} \omega_2}{\omega_1^3} \left[\frac{\gamma_{rf}/2\pi}{(\omega_1 - \omega_{rn})^2 + \kappa^2 p^2/4} \right] \left[\frac{\kappa}{\kappa - \epsilon} \right] \qquad (72)$$

This equation predicts that for excitation well out on the line wings, where $\omega - \omega_{rn} >> Kp$, the resulting line fluorescence per molecule will be independent of pressure. Furthermore, to the extent that the last term approaches unity (insignificant proportion of elastic collisions) it will be independent of gas constituency. A similar result obtains for the broad continuum fluorescence. These results are not changed by inclusion of Doppler broadening provided that the separation from resonance is also large relative to the Doppler width.

Although this particular result has not been emphasized previously to our knowledge, the basic idea is not new. Mitchell and Zemansky (ref. 12) discuss the interplay of line broadening and quenching in qualitative detail, and the results of Fouche, Herzenberg and Chang (ref. 11) are very similar to those presented above. However Fouche et al. did not include the elastic collisions which, within this simple theoretical model, are necessary to account for initial increases in the fluorescence cross section with background gas pressure as observed by St. Peter's et al. (refs. 14, 22).

The simple Lorentz broadening theory is still utilized as a useful first approximation close to resonance. Thus, it is interesting to compare Eq. (72) with the quantum mechanical result for scattering, which should describe the same effect far from resonance. If transitions through a single intermediate level dominate the scattering (as in the case of Al atoms described previously, even tens of nm from resonance) then the scattering cross section is, from Eq. (45),

$$\sigma^T = 2\pi \frac{\omega_2^3}{\omega_1} \left(\frac{e^2}{mc^2} \right)^2 \frac{f_{rf} f_{rn}}{(\omega_1 - \omega_{rn})^2} \qquad (73)$$

Using the relationship between oscillator strength and radiation line width

$$\gamma_{rn} = \frac{2\omega_{rn}^2}{c} \left(\frac{e^2}{mc^2} \right) f_{rn} \qquad (74)$$

and the equivalent expression for γ_{rf}, we obtain

$$\sigma_s = \frac{\pi^2 c^2 \gamma_{rn} \omega_2}{\omega_1^3} \quad \frac{\gamma_{rf}/2\pi}{(\omega-\omega_{rn})^2} \tag{75}$$

This result differs significantly from Eq. (72) by the absence of the factor $\kappa/(\kappa-\epsilon)$. The difference reflects a failure in one or perhaps both theoretical analyses which must be examined by a more detailed theory.

Effect of Statistical Broadening. - Up to this point, we have used the Lorentz broadening theory to describe the effects of interactions between molecules on fluorescence. There is a complementary approach to line broadening which leads to somewhat different conclusions. In the rudimentary form of this theory, the relative motions of molecules are neglected. The fields at a molecule produced by its near neighbors introduce relative shifts in energy levels such that the absorption line for that molecule is also shifted. The overall broadened line is produced by the superposition of these shifts weighted by the statistical probability of the configurations producing each shift. This approach has been called the statistical broadening theory (ref. 12).

Thus, if we designate the coordinates describing a particular configuration of neighbors around a molecule by X, the probability of this configuration by P(X) and the resulting shift by $\delta(X)$, the absorption line is given in the simplest formulation by

$$\sigma_a(\omega) = \left[\frac{\pi^2 c^2 \gamma'_{rn}}{\omega_{rn}^2}\right] \int dX\, P(X) \frac{\gamma_r/2\pi}{[\omega-\omega_{rn}-\delta(X)]^2 + \gamma_r^2/4} \tag{76}$$

Except for the contribution of the natural line width, this type of broadening is of the type often called inhomogeneous broadening; that is, the absorption line of any particular molecule at a particular time is much narrower than the composite line width. Doppler broadening, which is also inhomogeneous in nature, can be incorporated within this formulation by extending the variables indicated by X to include the velocity of the absorbing molecule, and including within $\delta(X)$ the corresponding Doppler shift.

Equation (76) differs from its Lorentz broadening counterpart in that it does not predict increasing absorption with pressure far from resonance. Furthermore, it can account for the absorption line asymmetry and shift which are observed in many pressure broadening experiments. However it represents an extreme case (static condition) just as does simple collision broadening (instantaneous collisions). Many physical situations can be expected to fall somewhere in between. Such cases can be represented conceptually by adding a term to γ_r which depends on the rate of change of the configuration X.

It is the task of detailed line-broadening theory to predict the behavior of the inhomogeneous and homogeneous contributions to the line shape. The goal of our theoretical considerations up to this point has been to use simple, general results to illustrate the relationships between scattering and fluorescence, as these terms are defined herein. We have also tried to make clear the intimate relationship between fluorescence excited near resonance by narrow wavelength sources, and the basic characteristics of line broadening. The continuing development of tunable lasers is opening this field of research into what should be an exciting and informative subject.

Excitation into Dissociative Continuum. - When a molecule is excited into a dissociative state by absorption of light, it must either re-emit this energy quickly or fly apart, converting an appreciable fraction of its energy to kinetic energy. The time required to dissociate is on the order of 10^{-11} to 10^{-12} seconds. Thus, in this situation there is little time for collisions to quench or alter the re-emission, with the result that it assumes the characteristics of scattering.

Holzer, Murphy and Bernstein (ref. 4) have identified and examined this situation in re-emission from halogen vapors I_2, Br_2, Cl_2, IBr, ICl and BrCl. The scattering is characterized by strong overtones out to many harmonics, introduced by transitions through the continuum of outgoing spherical waves which characterize the dissociative states. The enhancement of this kind of scattering can be moderately strong. Holzer, Murphy and Bernstein found that when I_2 is excited by 488.0 nm radiation, the cross section for the fundamental vibrational RS is about 4.4×10^{-28} cm^2/sr, 100 times larger than that for the ν_1 band of methane, or about 800 times stronger than that for N_2 at that wavelength. However, cross sections for this type of scattering from Br_2 and Cl_2 are much smaller.

Other molecules which are conveniently excited above their lowest dissociation limits are O_3 (~1000 nm) and NO_2 (398 nm) (ref. 23). Conflicting results exist for NO_2 excited at 337.1 nm, with unpublished ν_1 vibrational cross sections quoted from 1 to 1000 times that of N_2. One possible source of difficulty with these measurements is that N_2O_4 exists in equilibrium with

NO_2, and the equilibrium constants are sensitive functions of (NO_2/N_2O_4) partial pressures and temperature. Furthermore, N_2O_4 absorbs more strongly than NO_2 near 337.1 nm (ref. 24).

Finally, the RS cross sections for O_3 excited near its very strong dissociative continuum centered at 250 nm have not been measured yet. However, in Chap. IV we develop an estimate of this cross section that suggests it might be very large.

Scattering following excitation into the dissociative continuum has been examined theoretically by a number of authors, with particular attention given to I_2. Behringer (ref. 25) developed a theoretical expression for its intensity. Jacon, Berjot and Bernard (ref. 8) developed a quantitative expression for the scattering intensity as a function of the incident wavelengths, and demonstrated agreement between this expression and their experimental results. In particular, they pointed out the importance of off-resonance (virtual) terms in the scattering amplitude. Finally, Kiefer and Bernstein (ref. 26), and Williams and Rousseau (ref. 27) have explained the vibrational rotational structure of the vibrational and overtone " lines. "

Scattering Over Quenched Fluorescence. - Jacon et al. (ref. 9) have pointed out that when fluorescence excited on resonance is strongly quenched, its intensity can be reduced to a point where scattering through nearby off-resonance states is comparable. This behavior can be predicted by writing the quantum-mechanical expression for the cross section in the form

$$\sigma \propto \frac{\omega_s^4}{\hbar^2 c^4} \quad F_i \quad \sum_f{}' \left| \left\{ \frac{\langle f|D|r\rangle\langle r|D|i\rangle}{-i\Gamma_r/2} + \sum_g{}' \frac{\langle f|D|g\rangle\langle g|D|i\rangle}{\omega_{gi}-\omega_1-i\Gamma_g/2} \right. \right. \tag{77}$$

$$\left. \left. + \text{antiresonant terms} \right\} \right|^2$$

Here we have summed over the limited group at final states (f) for which $\omega_1 - \omega_{fi}$ is in the frequency range of interest. The contribution of the intermediate state in resonance (r) is separated out of the sum over intermediate states, and we have inserted total widths Γ (including collision broadening) into the resonance denominators in order to take account of Lorentz broadening. Jacon et al. consider Eq. (77) to represent both fluorescence and scattering.

The widths Γ in Eq. (77) can be expressed in the form

$$\Gamma_r = \gamma_r + \kappa p$$

where γ_r is the total width for non-collisional decay.

At low pressure the resonance term will clearly predominate (providing the line separation is much larger than line widths), leading to strong fluorescence. However, at high pressure the resonance term will be much smaller, whereas the sum over off-resonance terms will change relatively little if $\omega_{gi} - \omega >> kp$ for all significant contributions. Thus it appears that there are cases in which near-resonance scattering can predominate over strongly quenched fluorescence.

Berjot, Jacon and Bernard (ref.10)have used this argument to explain the changes in the re-emission of I_2 excited by 501.7 nm radiation as the background pressure of argon is varied from 0 to about 40 atmospheres. The changes in depolarization, lineshape and overtone sequence are all characteristic of the transition of the dominant contribution from fluorescence (at low pressure) to Raman scattering (at high pressure). However, Jacon et al. (ref. 9) leave the impression that the intermediate states which contribute the dominant scattering at high pressure are part of the discrete set, as implied by Eq. (77). In fact, the polarization, intensity and lineshape variation with pressure all indicate that the dominant scattering contribution arises from transitions which begin from excited vibrational states and reach the dissociative continuum. Thus, we believe that Jacon et al. have actually observed RS following excitation into the dissociative continuum, rather than NRRS from discrete states.

Fluorescence

Dependence of Fluorescence on Gas Pressure. - The basic equations governing the dependence of fluorescence on gas pressure have been given previously. From Eq. (71), the effective cross section per molecule for line fluorescence excited by a monochromatic incident beam is

$$\sigma_L(\omega) = A \frac{\Gamma/2\pi}{(\omega_1-\omega_r)^2 + \Gamma^2/4} \frac{\gamma_L}{\Gamma-\Gamma_E} \tag{78}$$

under the assumption of Lorentz broadening. Here A represents factors that are independent of pressure, and γ_L represents the probability per unit time for decay by emission into the observed line. The pressure dependence of the contributions to the linewidth Γ can be expressed by

$$\begin{aligned} \Gamma &= \gamma + \Gamma_E + \Gamma_B + \Gamma_Q \\ \Gamma_E &= \epsilon p \\ \Gamma_B &= bp \\ \Gamma_Q &= qp \end{aligned} \tag{79}$$

where γ is the total width for non-collisional decay (radiation + dissociation, etc.) and p is gas pressure. Equation (78) is applicable at line center, providing that collision broadening dominates over Doppler broadening, and in the line wings beyond the range where they are effected by Doppler broadening. If, in addition, excited state decay is primarily through collision-induced processes, then for excitation on line center ($\omega_l = \omega_r$)

$$\sigma_L \propto 1/p^2 \tag{80}$$

Likewise, on the wings we find that σ_L is independent of pressure, as discussed previously.

On the other hand, if the spectral distribution of the incident beam is constant over the absorption line, the effective "cross section" is obtained by integrating $\sigma_L(\omega_l)$ over frequency. This operation yields

$$\sigma_L = A \frac{\gamma_L}{\Gamma - \Gamma_E} \tag{81}$$

It should be noted that σ_L now has dimensions of area (x) frequency, since it must be multiplied by incident irradiance per unit frequency. This result produces the pressure dependence of the Stern-Volmer equation (ref. 12); i. e. ,

$$\frac{\gamma_L}{\Gamma - \Gamma_e} = \frac{\gamma_L}{\gamma + (b+q)p} \tag{82}$$

Likewise, if the absorption is continuous or quasi-continuous (composed of many lines with line separation < line width) such that the absorption per molecule is not pressure-dependent, we obtain

$$\sigma_L = A\, \rho(\omega) \frac{\gamma_L}{\Gamma - \Gamma_E} \tag{83}$$

where $\rho(\omega)$ is an effective line density. Thus, in this case also the Stern-Volmer pressure dependence is predicted. It should be noted that the results for the last two cases do not depend on lineshape, but rather on the integral over it. In that sense they do not depend on the assumption of Lorentz broadening. A case of major present interest involves fluorescence from one of the minor constituents in a carrier gas (air). Under the assumption that collision rates are additive,

$$\Gamma_E = \epsilon_1 p_1 + \epsilon_2 p_2 + \ldots + \epsilon_c p_c$$

$$\Gamma_B = b_1 p_1 + b_2 p_2 + \ldots + b_c p_c \qquad (84)$$

$$\Gamma_Q = q_1 p_1 + q_2 p_2 + \ldots + q_c p_c$$

Here p_1, p_2 ... represent partial pressures of minor gases, and p_c, the partial pressure of the carrier gas. Likewise $\epsilon_1 \cdot b_1$, q_1, etc., represent corresponding coefficients for components of the line width. In cases where the carrier gas dominates the quenching,

$$\frac{\gamma_L}{\Gamma - \Gamma_E} \rightarrow \frac{\gamma_L}{(q_c + b_c)p_c} \qquad (85)$$

and consequently, the fluorescence per molecule is independent of minor constituency. When this result is applicable to atmospheric monitoring, it implies that only a simple and rather small (< 10%) pressure broadening correction must be made to fluorescence data in determining the molecule number density of a minor constituent. This is the favorable situation for probing applications which was pointed out previously.

Depolarization of Scattering and Fluorescence. - The polarization characteristics of scattering and fluorescence are relevant to present interest for two reasons. First, polarization can often be used to identify what type of process is being observed; second, processes can be separated from each other and/or background on the basis of polarization. For example, it should be possible to view nearly unpolarized fluorescence from NO_2 over highly polarized Raman scattering from CO_2, even though both occur in the same spectral region, by using polarization filters to reject the CO_2 scattering.

The polarization of scattered light and fluorescence is partly characterized by its depolarization factor. There are two alternative definitions of depolarization. The one we shall use is in terms of an experimental configuration involving a linearly polarized incident light beam and scattered light propagating in a direction perpendicular to the polarization and propagation direction of the incident beam. The depolarization ρ is then the following ratio: the intensity of that scattered light with polarization perpendicular to the incident beam polarization, divided by the intensity of that scattered light with polarization parallel to the incident beam polarization. This definition is illustrated in Fig. 10. In terms of the symbols used in that figure

$$\rho = I_x / I_z. \qquad (86)$$

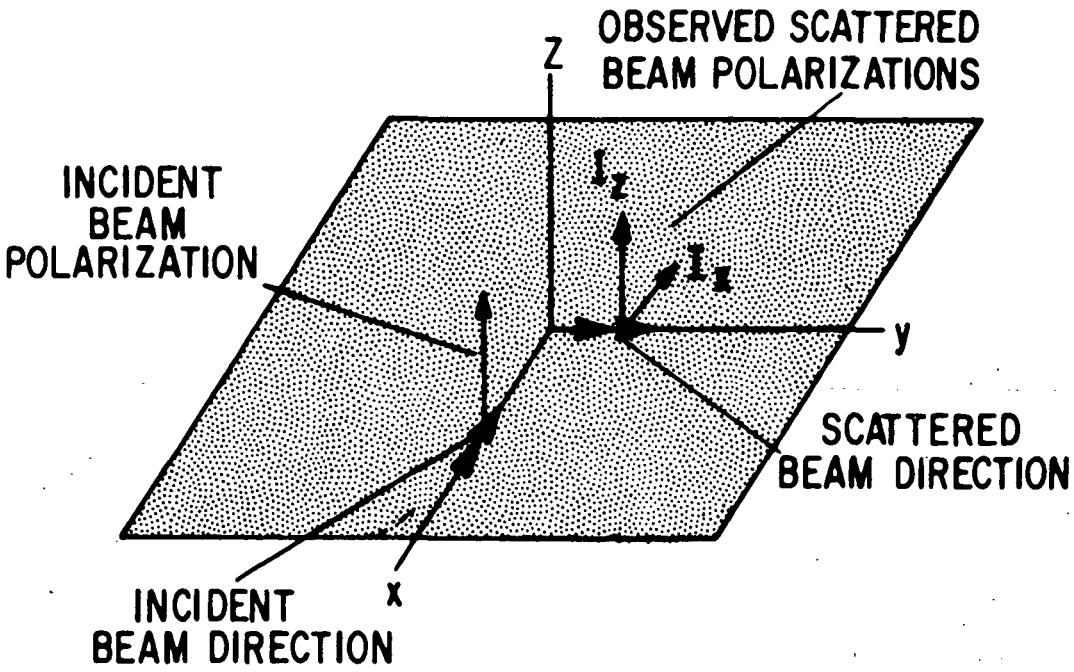

Figure 10 Scattering geometry for definition of depolarization.

The definition of the alternative depolarization ρ' is similar except that the incident beam is unpolarized. The relationship between the two quantities is

$$\rho' = \frac{2\rho}{1+\rho} . \qquad (87)$$

The significance of these depolarization factors extends beyond the experimental configuration in which they are defined. In fact, the depolarization is a fundamental characteristic of the scattering, or fluorescence, determining for example its angular dependence (ref. 18). The depolarization (ρ) for vibrational Raman scattering away from resonance is quite small for many molecules, with occasional exceptions where it reaches 3/4. On the other hand, the depolarization of non-resonance rotational Raman scattering is usually 3/4.

The studies of depolarization in scattering and fluorescence trace back to the original theoretical works of Placzek (ref. 28) and Mrozowski (ref. 29) and the early experimental work of Wood and subsequent work of Pringsheim (ref. 30).

The depolarization of scattering and fluorescence from symmetric top molecules excited near and in resonance has been examined theoretically

by Seth D. Silverstein. This examination has revealed an effect not previously predicted to our knowledge: the dimunition of depolarization in scattering upon excitation in a dissociative continuum. This result has been demonstrated in experiments conducted by R. L. St. Peters and Seth D. Silverstein. Their results have been published (see ref. 31 and Appendix D). Below we present a qualitative description of their work.

Two types of processes are considered. In the first, the transition is from a discrete initial state through a discrete intermediate state to a discrete final state (DDD transition). In the second, the intermediate state is within the dissociative continuum (DCD transition). When the excitation is on resonance, DDD processes lead to fluorescence, while in the case of excitation well off resonance they may lead to scattering, as we have defined it. (But see Appendix A.) On the other hand, the DCD processes lead to scattering of the type identified by Holzer, Murphy and Bernstein (ref. 4). Many of the depolarization results for the DDD case have appeared previously, but in obscure references; these have been re-derived in the present work.

In the DDD case, the depolarization contributed by individual transitions is independent of the quantum number K which designates the angular momentum component of the molecule parallel to the figure axis of the symmetric top. For $K \neq 0$ there are in general three Q branch transitions, which we denote by Q_α ($\alpha = \pm 1, 0$). These components correspond to the total angular momentum sequences shown below.

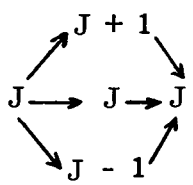

The individual depolarization contributions for these Q-branch components depend on the initial total angular momentum quantum number J. For $\alpha = \pm 1$, both go to 3/4 asymptotically at large J, while the $\alpha = 0$ component goes to 1/3. For K = 0 in both electronic states there is no Q-branch absorption and the component corresponding to $\alpha = 0$ is absent.

Besides the Q branch transitions, there are those in which the total angular momentum changes from initial to final state. The entire manifold of transitions is shown below.

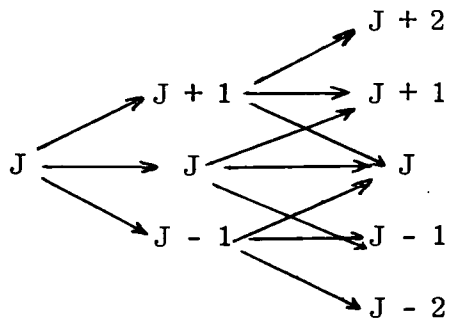

This manifold obviously results from the emission-absorption selection rules $\Delta J \pm 1, 0$. If $K=0$, in both upper and lower electronic states, then the selection rules reduce to $\Delta J = \pm 1$, and the $J' = J \pm 1$ transitions vanish, along with the $J \rightarrow J \rightarrow J$ transition. The depolarization of $\Delta J = \pm 2$ transitions, and the asymptotic depolarization of the remaining Q-branch transitions is 3/4.

Since the Q-branch components start from the same initial state, and end on the same final state, their contributions can interfere within the absolute square of the scattering equation. (See Appendix B for a general discussion of interference effects.) However, the resonance situation will pick out only one of these transitions in the DDD case, providing that the separation of the upper states is larger than the linewidths involved.

In the case of I_2 excited from the ground electronic state by wavelengths longer than the dissociation limit, the transitions are of the DDD type and $\overline{K = 0}$ in both upper and lower electronic states. Furthermore, the rotational constant of I_2 is very small because of the large nuclear mass of iodine. Thus high angular momentum states are thermally excited. The transitions observed in recent experiments on I_2 using argon laser excitation are nearly all high J transitions, such that the asymptotic high J results for Q-branch depolarizations are applicable. Thus the depolarization of each component of the doublet which results (corresponding to transitions $J \rightarrow J+1 \rightarrow J+2, 0$ or $J \rightarrow J-1 \rightarrow J-2, 0$, depending on which state is excited) is 3/4.

This depolarization is observed, in fact, at low pressure. As (I_2 or background gas) pressure is increased, two effects can change the depolarization. First, elastic collisions occuring between excitation and reemission cause it to increase. Second, homogeneous line broadening can enable significant contributions from both ($J \pm 1$) Q-branch components, in which case they can interfere within the absolute square, reducing depolarization. In I_2, the separation of the $J \pm 1$ upper states in transitions which have been observed is sufficiently large so that the first effect can be expected to predominate, at least at moderate pressures. In fact, an increase in depolarization is observed in this regime.

In the DCD case, the situation is markedly different, because the continuum states are effectively degenerate in J. As a result, the Q-branch transitions through J+1 and J-1 intermediate states interfere, reducing the depolarization of the Q-branch to a limiting value of 1/8. The experiments we have conducted to observe the Q branch in DCD transitions yield a depolarization of 0.12 ± 0.01, in excellent agreement with the theoretical result. These experiments necessarily require very narrow ($< 2 cm^{-1}$) slit because the $J' = J+2$ and $J' = J-2$ branches are shifted only slightly from the Q-branch. Theoretical calculations indicate that the composite depolarization of all three branches is 1/3 in the limit of large J. This result has also been confirmed by our experiments with wide slit functions, and has been observed by others. Our interpretation of the high pressure I_2 experiments described by Berjot et al. (ref. 10) is that the DDD fluorescence that predominates at low pressure is quenched to the point where DCD scattering, which is not quenched, predominates at high pressure. This interpretation is consistent with their relatively wide slit function observations of the change in depolarization from 3/4 to 1/3 at high background pressures and their observation that higher pressures are required to produce the effect at 514.5 nm than at 501.7 nm. The latter observation is reasonable because DCD transitions are weaker at the larger wavelength because fewer molecules are available in the higher vibrational states which produce them.

III - EXPERIMENT

In this chapter we describe experimental results obtained under support of this contract, and the two separate experimental facilities utilized for this work.

Double Monochromator Facility

The Double Monochromator Facility (DMF) has been in use for several years, providing measurements of Raman cross sections and scattering lineshapes in flames, among other things. A block diagram of its present configuration is shown in Fig. 11.

Light sources. - The primary light sources used with this facility are separate argon and krypton ion lasers (Coherent Radiation Laboratory Model 52) run from a common power supply. The ion lasers feature servo power stabilization to much better than 1%, and they can be operated in single longitudinal mode (SLM) using a tilted etalon. This technique provides lines with spectral width and long term stability within 0.0001 nm, in conjunction with tuning ranges on the order of 0.01 nm for the stronger lines. The available spectral lines, corresponding power levels and SLM performance are shown in Table I.

Double Monochromator. - A Spex 3/4 meter double monochromator, model 1400-11, is used to analyze the light diverted from the incident beam by gas molecules. This monochromator is fitted with 1200 ℓ/mm Bausch and Lomb gratings blazed for 500 nm (first order), providing a linear reciprocal dispersion of about 0.55 nm/mm at the exit slit. A periscopic microscope focussed on the entrance slits from inside the monochromator facilitates alignment, since the image of light diverted from the laser beam is likewise focussed on these slits when optimum alignment is achieved, and thus the slits and scattering volume are viewed simultaneously in focus through the microscope. The wavelength setting is sensed directly from the lead screw by a digital encoder providing 0.001 nm resolution. Scattered light which has passed through the spectrometer is detected by a selected RCA C31000E extended red response photomultiplier in a dewar cooled to -70°C by N_2 gas bubbled through liquid N_2. The dark count of this tube at room temperature is approximately 20,000 cts/sec, but at -70°C it is reduced to about 10 counts/sec. Careful measurements have revealed that the tube sensitivity to visible light remains nearly constant over this range. This photomultiplier has a semiconductor first dynode whose high secondary electron production produces a discrete pulse height spectrum. This characteristic facilitates pulse counting signal processing.

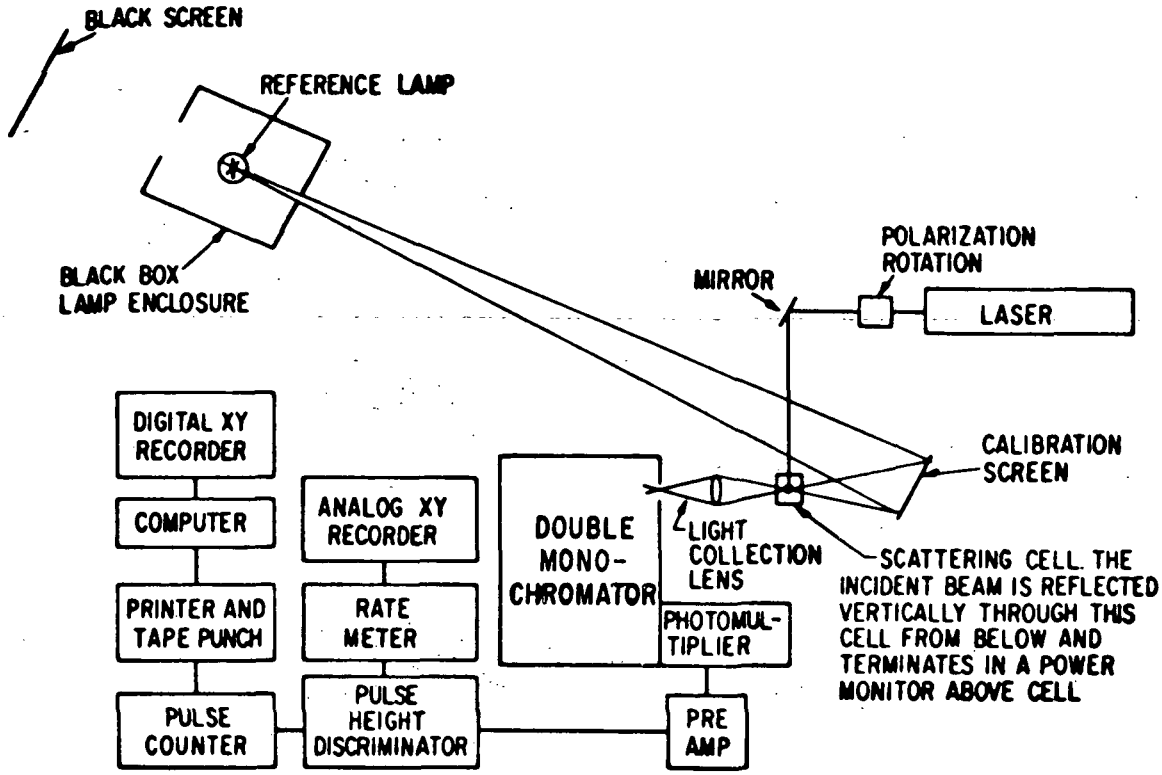

Figure 11 Block diagram of the Double Monochromator Facility (DMF).

TABLE I

Some spectral lines available from the Ar+ and Kr+ CRL Model 52 lasers used as primary sources for the double monochromator facility. Lines which have been operated in longitudinal single mode (LSM) and, in some cases, LSM tuning ranges and peak powers, are shown in the last two columns.

λ_{air}	Type	Power	LSM	Peak Power
350.74/356.42	Kr	0.05W		
351.11/363.79	Ar	?		
457.94	Ar	0.5 W		
476.24	Kr	0.2 W		
476.49	Ar	0.8 W	✓	
487.99	Ar	2.1 W	~0.01 nm	0.7 W
496.51	Ar	0.8 W	✓	
501.72	Ar	0.3 W	0.005 nm	0.1 W
514.53	Ar	2.3 W	~0.01 nm	0.7 W
520.83	Kr	0.2 W	✓	0.05W
530.87	Kr	0.5 W	0.01 nm	0.2 W
568.19	Kr	0.8 W	~0.01 nm	0.3 W
647.10	Kr	1.2 W		

Signal processing electronics. - The preamplified photomultiplier pulses are brought to a single channel pulse height analyzer (Hamner Model N302) which is usually operated in integral mode to reject small pulses characteristic of noise. The accepted pulses are sent to a count rate meter which provides an analog signal for an x-y recorder. They are also counted over preset time intervals and printed along with wavelength readings from the spectrometer digital encoder. A punched paper tape representation of this printout is also provided in order to communicate data to a computer for subsequent manipulation and display.

Vacuum and gas handling system. - The purpose of this system is to provide gases and gas mixtures for observation at the spectrometer. The system can be connected through a stainless steel bellows to a mounted scattering cell. In order to withstand corrosive gases, the system is constructed of stainless steel tubing and Hoke stainless steel valves, with stainless steel Swagelock fittings. Rough indication of gas pressure is provided by thermocouple gauges, and accurate pressure readings are obtained using a combination of Hg and silicone (Dow Corning 704) oil manometers. The system is evacuated by a Welch Duo Seal roughing pump and cold trap. It is necessary to provide a bypass on the cold trap in order to avoid condensing gases such as NO_2 and SO_2 in this trap. After long evacuation, the entire system will hold at < 10 m Torr for days with the pump and cold traps valved off, indicating that there are no significant leaks.

Calibration. - Absolute and relative spectral calibrations of the spectrometer-photomultipler system are obtained using GE 200W quartz-halogen projection lamps. These lamps, which are recommended by the Bureau of Standards as intense and stable secondary standards (ref. 32), were calibrated by Eppley Laboratory, Inc., and Optronic Laboratories, Inc. (one each). The absolute calibrations were checked by subsitution and found to be consistent within 10%. The lamps are mounted in a large (75 cm cube) black box with a small hole, through which one of them illuminates a diffuse scattering screen at a distance of several meters, as shown in Fig. 11. The scattering screen was constructed by flowing Eastman White Reflectance Paint (a suspension of $BaSO_4$ crystals) (ref. 33) onto a 1/2" thick aluminum plate. The area to be covered (9" square) was milled out to a depth of 1/16" and sandblasted. The barium sulphate coating was built up in several steps, with intervening slow ($\sim$ 1 day) drying in an enclosed space, and finally scraped with a sharped-edged glass plate back to a thickness of 1/16". Through a direct comparison of incident and scattered light, this screen was found to approximate a perfect Lambertian scatterer to within experimental error of 3% at a scattering angle of 30°, with incident light normal to the screen, over the spectral range from 450 nm to 500 nm, and separately, over the range from 500 nm to 650 nm. These spectral ranges were isolated using filters.

The light from the reference lamp is diffusely scattered by the screen and then passes through the scattering cell. Part of this light is focussed by the collection lens through the monochromator slit. A polarization filter near the lens (on the slit side) is inserted and rotated to determine the relative polarization response of the spectrometer. Sensitivity to second order diffraction (usually negligible) is evaluated by using a filter substitution technique.

This calibration technique provides the following important advantages:

1. The reference count rate and scattering/fluorescence count rate can be made approximately equal with convenient slit settings and reference lamp-to-screen distance. In our work visible light calibrations were obtained with the reference lamp placed at a distance of 3 to 4 meters from the scattering screen, and the slit settings used in reference measurements were typically 300 μm x0.5 cm (entrance), 3000 μm (intermediate), and 300 μm (exit). These slit widths are sufficiently large to avoid significant diffraction and polarization effects.

2. All of the light from the reference lamps collected by the lens and subsequently focussed through the entrance slit of the spectrometer must pass through the virtual image of the entrance slit within the scattering cell. Since the scattered light emanates from the same region, spatial variations in system response should not introduce significant calibration errors.

3. The calibration of the system can be checked using the reference lamp during each measurement, even with the cell in place.

Experiments With NO_2

Nitrogen dioxide exhibits strong absorption through most of the visible and into the uv. At wavelengths longer than the first dissociation limit (~398 nm) the absorption spectrum consists of many discrete lines; however the distribution is so dense that the fine structure can be seen only at very low NO_2 pressures (< 1m Torr).

Laser-excited fluorescence from NO_2 has been studied by several groups, among which are: Sakurai and Broida (ref. 34); Sackett and Yardley (refs. 35, 36, 37); Fouche, Herzenberg and Chang (ref. 11); and Stevens, Swagel, Wallace and Zare (ref. 38). Sakurai and Broida described the overall features of the fluorescence spectrum, measured low pressure absorption coefficients at a number of laser wavelengths, and identified an isolated absorption line within the 488 nm argon laser gain curve. These authors clearly demonstrated the strong advantage tuned laser fluorescence provides as a technique for unravelling complicated molecular spectra.

Sackett and Yardley carried out a detailed study of the time dependence of NO_2 fluorescence following pulsed excitation, as a function of incident light wavelength. Using a dye laser with narrow line (<0.1 nm) output in the blue (440-490 nm) they observed non-exponential decay which showed definite variations with excitation wavelength. In particular, for some excitation wavelengths they observed a weak component with much shorter lifetime (~1.25 μsec) (ref. 36). This observation is relevant to the anomaly, as yet incompletely understood, which exists in NO_2, SO_2, and CS_2 between the strength of absorption and the predominant fluorescence lifetime (ref. 39). In NO_2 the latter is about 100 times longer than expected from the accepted theoretical relationship between these two quantities. Sackett and Yardley's results also suggest the possibility that there may be spectral regions where the fluorescence quenched by air is much stronger than observed so far.

The theoretical contributions of Fouche, Herzenberg and Chang have been mentioned in Section II. Their experimental results include measurements of the absolute intensity of the line and continuum fluorescence components excited at several Argon laser wavelengths, and measurements of air quenching coefficients. These results will be discussed in more detail subsequently.

Stevens, Swagel, Wallace and Zare report the characteristics of NO_2 fluorescence excited by a narrow band (0.01 nm) pulsed dye laser operated in the spectral region from 593.4 to 594.0 nm. From the spectral, temporal and polarization characteristics of the fluorescence, they were able to draw important information regarding the electronic states and rotational transitions associated with absorption in this region.

It is possible that NO_2 fluorescence can be used to measure its concentration in the atmosphere. This possiblity holds particular interest because NO_2 is an important primary pollutant, it is also a link in atmospheric photochemical chains producing more complex and more insidious pollutants, and as yet there are no well developed ways to measure it remotely in the atmosphere that appear to be fully satisfactory. The spectral distribution of re-emission from a mixture of NO_2, NO and N_2 at a total pressure near one atmosphere, excited by 488.0 nm light, is shown in Fig. 12. Fluorescence from NO_2 contributes three fairly sharp "lines" and a broad continuum. The Raman scattering lines of NO and N_2 also appear, superimposed on the continuum. It is apparent from this figure that even when strongly quenched, NO_2 fluorescence possesses detailed structure which can be used to identify its presence. On the other hand, both the line and continuum fluorescence can overlay Raman scattering from other gas constituents, contributing an undesirable background. Thus it becomes doubly important to know the strength of line and continuum components under conditions typical of those observed by atmospheric probing instruments.

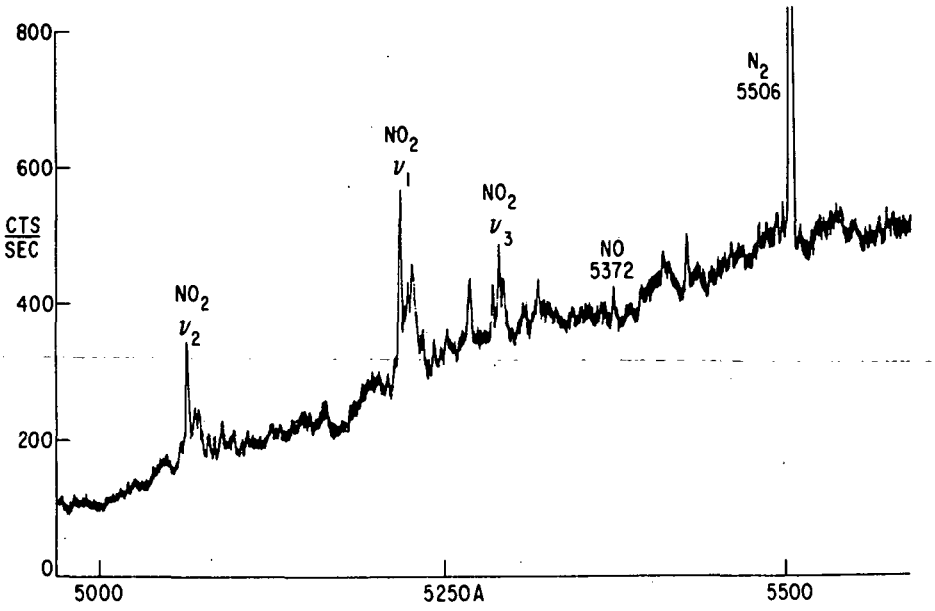

Figure 12 Spectral distribution of re-emission from trace amounts of NO and NO_2 in N_2 at a total pressure of 740 torr. Line fluorescence from NO_2 and Raman scattering from NO and N_2 are superimposed on wide band fluorescence from NO_2.

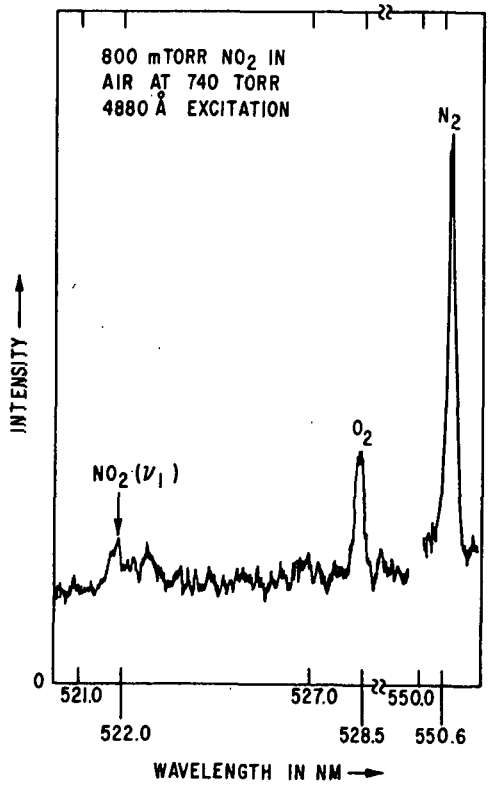

Figure 13 Typical spectral trace used to determine line and wide band fluorescence intensities from NO_2 in air. The excitation wavelength is 488.0 nm.

In previous work we measured the intensity of these components relative to O_2 Raman scattering in air at pressures near one atmosphere. In these measurements care was taken to avoid errors introduced by the NO_2/N_2O_4 equilibrium, which is quite sensitive to temperature, and by the tendancy of excited NO_2 to migrate out of the focal volume before re-emitting light. The measurements were repeated using the DMF with various slit settings for this contract. The results of one of these measurements is shown in Fig. 13. The detailed spectral distribution of the ν_1 line at low pressure (< 1 Torr) is shown in Fig. 14. Measurements of depolarization in the geometry of Fig. 10, obtained by rotating a polarization filter in front of the entrance slit, indicate that the depolarization of this line in air near STP is 1.0 ± 10%. Taking into account the spectral sensitivity variation of the spectrometer, the relative line widths and different polarizations, the results of Fig. 13 indicate that the NO_2 fluorescence intensity in the ν_1 "line" is 110 ± 30 times stronger per molecule than Q-branch vibrational RS from O_2. This result applies for 488.0 nm excitation in air at 740 torr, in the right-angle scattering geometry of Fig. 10. In order to obtain an absolute result, we note that the corresponding O_2 cross section has been measured in our laboratory to be (ref. 5)

$$6.8 \times 10^{-31} \text{ cm}^2/\text{sr} \pm 10\%$$

This value, for scattered light summed over polarization, is in good agreement with recent results obtained at two other laboratories. Thus we conclude that the effective differential cross section for NO_2 line fluorescence under the conditions specified above is

$$7.5 \times 10^{-29} \text{ cm}^2/\text{sr} \pm 35\%$$

or about 130 times enhanced over the N_2 vibrational RS. Because of the strong depolarization of the fluorescence under these conditions, it should be nearly isotropic. Therefore, the corresponding total cross section should be, to a good approximation, 4π times the differential cross section, or

$$9.4 \times 10^{-28} \text{ cm}^2$$

These results are in fairly good agreement with those obtained by Fouche, Herzenberg and Chang (ref. 11). This group measured the air- and self-quenching constants of NO_2 line (ν_1 and ν_2) and continuum fluorescence, and the magnitude of these fluorescence components relative to N_2 vibrational Raman scattering at a NO_2 pressure of 1 torr. From their results we calculate that the effective NO_2 differential cross section for the ν_1 line relative to the corresponding N_2 vibrational Raman cross section (for a trace of NO_2 in air at 740 torr and excitation at 488 nm) is approximately 190. The equivalent ratio for the ν_2 line (750 cm^{-1}) is, from their data, 132 and for the continuum fluorescence in a 1 nm band at a shift of 720 cm^{-1}, 120. The agreement for absolute line intensities is reasonable but our results indicate a

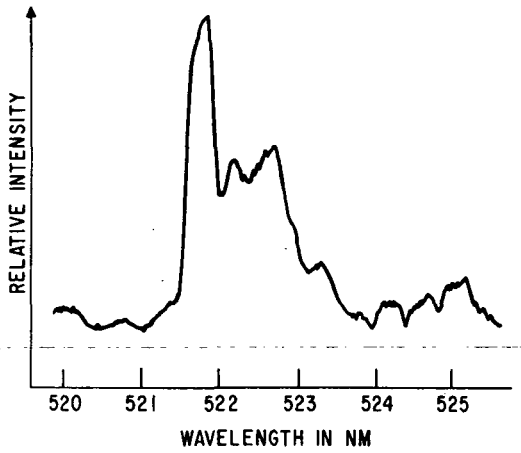

Figure 14 Detailed spectral distribution of the NO_2 ν_1-line fluorescence excited by 488.0 nm radiation. The spectral slit width for this measurement was triangular with 0.15 nm full width at half maximum.

continuum intensity about 6 times larger than theirs for a 1 nm band at 720 cm^{-1} under the conditions cited above.

As long as air is the primary quenching species, the effective NO_2 cross sections should be inversely proportional to collision frequency with air molecules. It is interesting to note that at an altitude of 30 km, where the collision frequency is reduced to about 1% of its sea level value ($\sim 10^{10}$ sec^{-1}) the effective cross sections for line re-emission from NO_2 should be enhanced by about 10^4 over the N_2 vibrational Raman cross section.

Experiments With Iodine Vapor

The vapors of halogens such as I_2, Br_2, and Cl_2 exhibit absorption in the visible, arising from $^3\Pi_0^+ \leftarrow {}^1\Sigma^+$ electronic transitions. The dissociation limits for these transitions are in the blue-green spectral region. Upon excitation at wavelengths longer than the dissociation limit, fluorescence has been observed, whereas at shorter wavelengths, the re-emission is characteristic of scattering (ref. 4).

Iodine and Bromine vapors are convenient subjects for studies of absorption and consequent scattering/fluorescence because they are relatively safe to work with, they are chemically compatible with glass, their vapor pressure is sufficient for many experiments at room temperature, and the distribution of their absorption lines is sufficiently dense so that one and often several absorption lines are found within the gain curves of many argon and krypton laser lines.

Our experimental studies have involved only I_2. Although this molecule seems to have a somewhat greater density of lines than NO_2, individual lines are easily resolved in absorption in I_2. For example, the absorption of I_2 within the 514.5 nm gain curve shown in Fig. 15 indicates the presence of four apparent lines within and on the edge of the gain curve. (Actually, some of these lines result from multiple transitions in near coincidence.) These lines remain resolved at the highest observed I_2 vapor pressure, 2.3 Torr. The situation in NO_2 is notably different. Sakurai and Broida (ref. 34) observed the presence of an isolated NO_2 line within the 488.0 nm gain curve and obtained some information about its shape by observing the transmitted light through a Fabry Perot interferometer. We have also observed this line using the method of tuned laser fluorescence. Our observations, which were qualitative in nature, indicate that this line has a width on the order of 0.002 nm FWHM at very low NO_2 pressure. However at pressures of a few mTorr the fluroescence intensity displayed little variations as the laser was tuned over the width (0.01 nm) of the gain curve. Thus we are led to suspect that NO_2 has an anomalously large self-broadening cross section, and in consequence, observation of its absorption line structure in the visible requires very low pressure, and long path length measurements. The contrasting ability to isolate individual strong lines in the I_2 spectrum is an advantage for studies of tuned laser fluorescence and the approach to resonance. Our work with I_2 has included the following experiments, of which the last two have been supported on this contract:

Measurement of absorption within the 514.5 nm gain curve. - These measurements involved the argon laser, single-moded and tuned by tilted etalon. The results, shown in Fig. 15, were obtained to evaluate the use of an I_2 filter to block the exciting line in Brillouin spectroscopy.

Measurements of re-emission intensity as a function of separation from resonance and background gas pressure. - The purpose of these experiments is to determine whether re-emission from I_2 excited slightly ($\sim$0.005 nm) off resonance is characteristic of scattering or fluorescence. The determination involved repetition and extension of the experiments of Fouche and Chang (ref. 13). Our conclusion is that the re-emission shows nearly counterbalancing effects of line broadening and quenching. The theoretical analysis of these effects in Section II accounts satisfactorily for the relatively weak dependence of re-emission intensity on background gas pressure observed

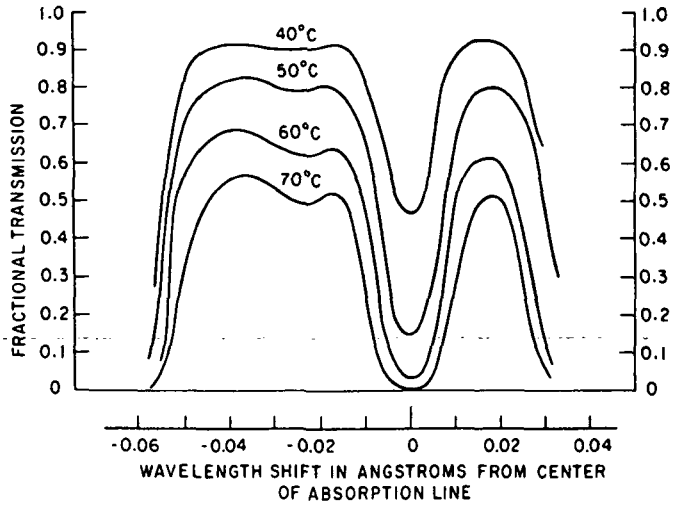

Figure 15 Absorption of I_2 vapor as a function of laser wavelength within the 514.5 nm gain curve of an Ar laser. The laser is single-moded and tuned by a tilted etalon, with wavelength monitored by a Fabry-Perot interferometer. Laser power into cell was 10 mW and laser linewidth < 0.0001 nm (0.001Å). The I_2 vapor pressures correspond to the indicated cold-finger temperatures.

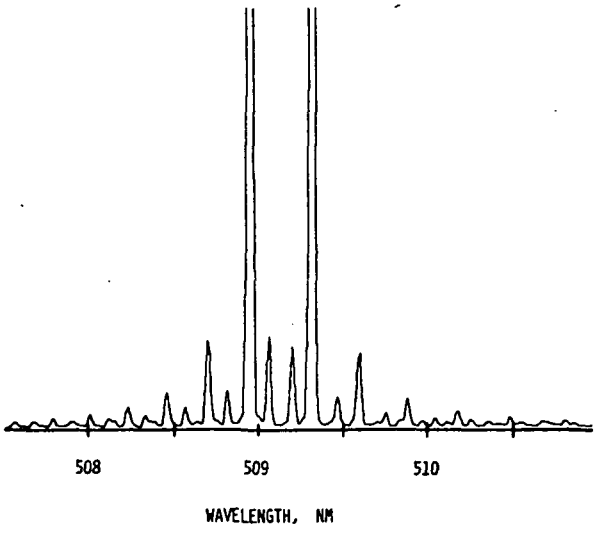

Figure 16 Antistokes fluorescence from iodine excited on a line within the 514.5 nm Ar laser gain curve. The two main peaks emanate from the originally excited I_2 state, while the satellite (collision) peaks result from energy exchanges in collisions associated with ±2 changes in rotational angular momentum quantum number.

by Fouche and Chang, and by St. Peters et al., (ref. 14). Because collision effects are still significant and particularly evident in the spectral fine structure of the re-emission at the largest separations from resonance involved in these experiments, we believe that the re-emission is more accurately described as fluorescence than as scattering.

Measurement of collision to main peak intensities as a function of separation from resonance. - This experiment was undertaken to determine if collision rates depend on separation from resonance. The antistokes fluorescence spectrum of I_2 excited within the 514.5 gain curve is shown in Fig. 16. The main peaks form the strong doublet resulting from direct re-emission from the excited state, whereas the smaller peaks result from collisions imparting a change in angular momentum in units of $\Delta J = \pm 2$ before re-emission. Theoretical results for the time dependence of re-emission led us to speculate that as the incident light is tuned away from resonance with the transition producing this spectrum, at some point the change from fluorescence to scattering should begin, evidenced in this case by a reduction in the collision to main peak intensity ratio. The results obtained upon tuning beyond several Doppler widths is shown in Fig. 17, for the case of one resonance line within the Kr ion laser gain curve at 568.2 nm. It is evident that the effect described above was not observed. In the case of another resonance line near one edge of the 514.5 nm gain curve, we were able to observe the collision to main peak ratio out to more than 1.4 GHz from the resonance center on one side, which is about 3 times the Doppler width. While the two peak intensities decreased by a factor of nearly 10^4, their ratio again remained constant to within a small experimental error.

There are several plausible explanations for the failure to observe the onset of a change from fluorescence to scattering. Among these are:

1. The speculations drawn from the classical theory are wrong. In particular, there may be quantum mechanical effects which are important even to the qualitative nature of the phenomenon as observed in these experiments.

2. These may be significant inhomogeneous broadening, other than Doppler broadening, which extends to the wings of the absorption line. In this case, the molecules responsible for most of the re-emission can be those momentarily shifted into resonance by the fields of near neighbors.

With respect to the first point, two of our group (S.D. Silverstein and R.L. St. Peters) have developed a quantum mechanical calculation which suggests that a constant collision-to-main peak ratio may not be unexpected

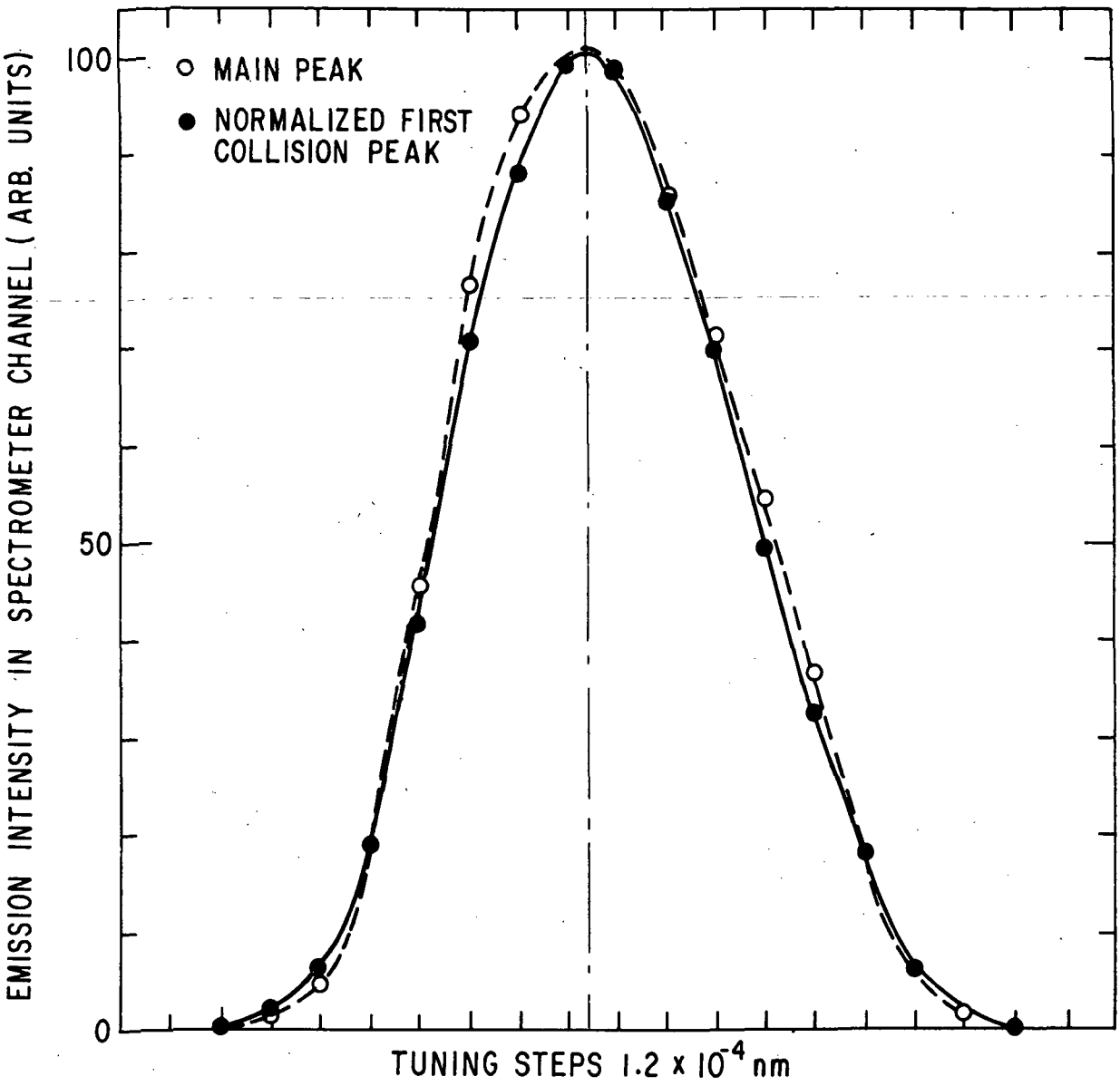

Figure 17 Normalized collision and main peak intensities as a function of separation from resonance.

even in the absence of inhomogeneous broadening. This calculation, however, involves some subtle points which have not yet been adequately resolved.

Whatever the case, the persistence of the collision peaks is strong evidence that this re-emission is fluorescence rather than scattering, as those terms are defined by Holzer, Murphy and Bernstein (ref. 4), and as defined within this report.

Measurements of depolarization of re-emission excited above and below the dissociation limit. - These experiments were conducted to verify the theoretical calculations of depolarization discussed in Section II. The experimental conditions and results have already been described in that section.

Measurement of the Ozone Cross Section at Visible Light Wavelengths

The cross section for O_3 vibrational Raman scattering (ν_1 - 1110 cm^{-1}) was measured for this contract in order to establish a benchmark for corresponding UV measurements. The ozone was generated in a flowing stream of O_2 by photo-dissociation, using a low pressure Hg discharge lamp specially designed to maximize output at the 184.7 nm line relative to the 253.7 nm line. The lamp was enclosed in a 15 cm I.D. pyrex pipe with aluminum end plates and Teflon polymer gaskets. Oxygen pressure and flow rate were measured with suitable precision instruments. The O_2/O_3 mixture was transported through 3/8" I.D. Tygon tubing to the first of two Spectrocil quartz cells (Markson cells, 5 cm long, 2 cm I.D., with two ports) where O_3 concentration was measured by transmission of 253.7 nm radiation from a low pressure Hg lamp. Parallel interference and monochromator filters were used to ensure that only 253.7 nm was observed. The slow decay of O_3 in the cell (~25% in 10 minutes) under non-flowing conditions indicated that the 253.7 nm radiation level used for concentration measurements was not sufficient to significantly alter the O_3 concentration at the flow rates employed. (The 253.7 absorption in O_3 is dissociative.) Ozone concentrations were calculated using well established absorption coefficients (ref. 19). These measurements indicated that the O_3 generator is a stable source providing O_3 concentrations which can be controlled easily by varying the flow rate . The concentration obtained at an O_2 flow rate of 400 cm^3/min is 3.2 torr O_3 in 740 torr O_2.

The second quartz cell was connected to the first cell by 75 cm of 0.95 cm (3/8") Tygon tubing. This cell was used for the scattering measurements. The cells were switched with tubing connections unchanged to determine if the O_3 concentration was significantly changed while flowing through the Tygon tubing. After flow at 400 cm^3/min and O_3 generation had been established for one hour, the concentration in the second cell stabilized at 95% of that in the first cell.

The gas mixture exiting the second cell was passed through Linde Type 13X Molecular Sieve to convert O_3 back to O_2, and then exhausted into a vacuum system through a metering valve.

The scattering intensity of O_3 was measured relative to that of O_2 in the standard 90° geometry illustrated in Fig. 10. Depolarization of the O_3 scattering was found to be less than 20%. The techniques used in these measurements have been described in detail in a previous publication (ref. 40). With a 0.5 nm FWHM semirectangular slit function, we found that the ratio of O_3 to O_2 vibrational Raman scattering, at shifts of 1110 and 1557 cm^{-1}, respectively, is 1.96 for 514.5 nm excitation and 2.05 for 488.0 nm excitation. The estimated error in these measurements is ±20%. The predominant sources of uncertainty are the concentration and scattering count rate determinations. Using our previously measured value for the O_2 Raman scattering cross section, we calculate for the absolute O_3 vibrational cross section a value of 1.01×10^{-30} cm^2/sr ± 25%, at 514.5 nm, for the scattering geometry of Fig. 10.

Fouche and Chang (ref. 41) have reported the O_3/N_2 vibration cross section ratio to be 4.0. In another publication (ref. 42) they report the corresponding O_2/N_2 ratio to be 1.2, which is in agreement with our result. Thus their results lead to the moderately larger value of 3.3 for the O_3/O_2 vibrational RS cross section ratio at 514.5 nm.

Spectrometer-Dye Laser Facility

The Spectrometer-Dye Laser Facility (SDLF) includes a Spex 3/4 meter spectrometer/monochromator and a pulsed dye laser whose output can be doubled, producing incident light over the wavelength range from 230-760 nm. The dye laser, which is pumped by an AVCO Model C950 pulsed N_2 laser, provides pulses with spectral width of 0.005 nm and time width of 5 nsec., at a rate of 100 pps. The average power in the visible is 10mW, and in the uv (doubled), 10-100 μW. Photomultipliers and pulse-counting and timing data analysis are incorporated into this facility, which provides time resolution of 6 nsec. Concurrently, the monochromator provides spectral analysis of re-emitted (or incident) light to 0.02 nm. A Fabry-Perot etalon is used to monitor the dye laser output to higher resolution. The system configuration is illustrated in Fig. 18. A detailed description of components of the system follows.

Dye laser. - The dye laser is pumped by a pulsed N_2 laser; its configuration is similar to that described by Hänsch (ref. 43). The pulsed N_2 pump laser emits pulses of 100 KW peak power at 337.1 nm, and has an average power of 100 mW when operated at its maximum repitition rate of 100 pps. This beam, which is rectangular in cross section with < 2 mr divergence in the short dimension and < 30 mr divergence in the long dimension, is brought to a near focus just inside the surface of a flowing dye cell with an optical

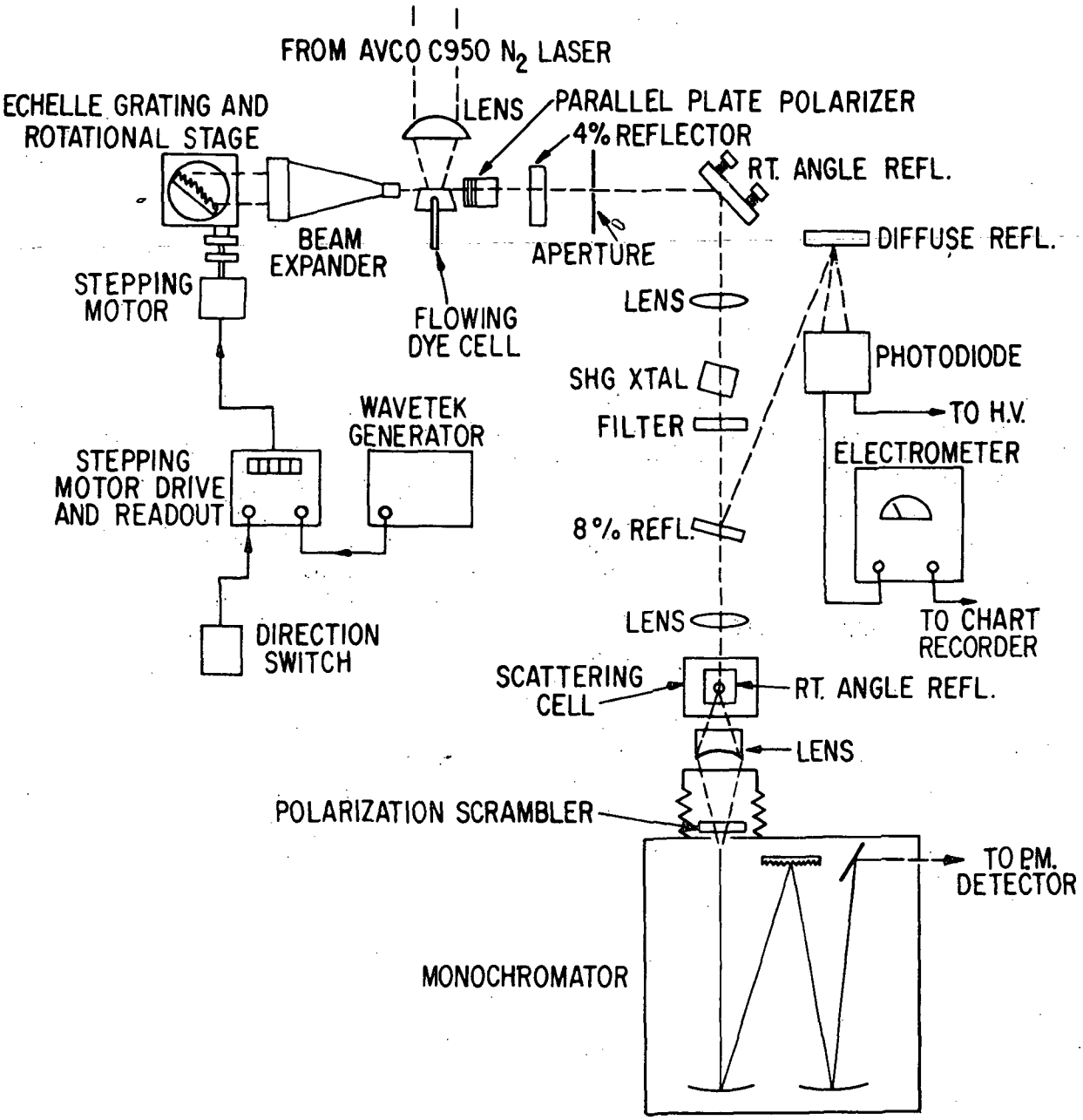

Figure 18 Tunable dye laser and optics for scattering experiments.

grade fused quartz lens of 5" focal length (FL) and 3" diameter. The focal region is a narrow line about 1 cm long and about 0.3 mm high. Most of the N_2 laser beam energy is absorbed within a fraction of a mm just inside the dye cell. The concentration of the dye is set high (about 5×10^{-3} M for rhodamine 6G) to produce strong absorption and a narrow rectangular active volume.

A detail of the flowing dye cell is shown in Fig. 19. The cell was constructed by fusing two fused quartz tubes together as shown in the side view cross section. Quarter inch fused quartz tubing was then attached to the outer cylinder at the angles shown to produce a smooth flow at the input and output connections. The cell was then cut at an angle of 8° to 12° as shown in the top view of Fig. 19. Good optical quality windows purchased from Lambda Optics, antireflection (AR) coated with a broadband multilayer coating on one surface by Broomer Research Corp., were then carefully epoxied on the sides of the 1" diameter tube with the coated surfaces to the outside. Care was taken to avoid blocking the optical path just inside the quartz tube wall with the cementing epoxy. Epoxy was also placed on the inner tube to seal the chamber from the dye solution. The 8° to 12° angle prevents reflection from the windows from being amplified along with the laser beam to significant proportions by the extremely high gain active volume. A pump with a maximum flow rate of 6.3 gal. per minute at 5 psi, speed controlled by a variable voltage transformer, is used to circulate the dye solution through the cell. The dye cell was rigidly mounted on a Brinkman model MP-11/R micromanipulator that allows 3-D translational positioning of the cell with respect to the dye laser optics while the system is operating.

The tuning component of the dye laser is a 58 x 58 mm, 300 ℓ/mm echelle grating blazed at 61°. This grating is mounted on an Aerotech Model ATS-301R rotational stage. The Aerotech stage has positioning resolution of 0.1 arc sec when using the fine adjust differential screw. An Aerotech ATS-301D digital stepping motor and readout is used to rotate the grating. Since the differential screw on the rotational mount moves in and out, the stepping motor used to drive the screw had to be mounted on a translational stage that was free to move back and forth with the linear motion of the differential screw. A ceramic insulated coupler was used to couple the stepping motor shaft with the differential screw shaft. The ceramic coupler provides thermal isolation between the stepping motor and the echelle grating. The grating can be slewed at a fixed rate or stepped manually with the Aerotech drive unit or can be stepped at a present constant rate from an external Wavetek model 115 VCG generator. The direction of rotation can also be controlled externally. A digital readout is provided by the Aerotech drive unit and serves as a reference for positioning the grating.

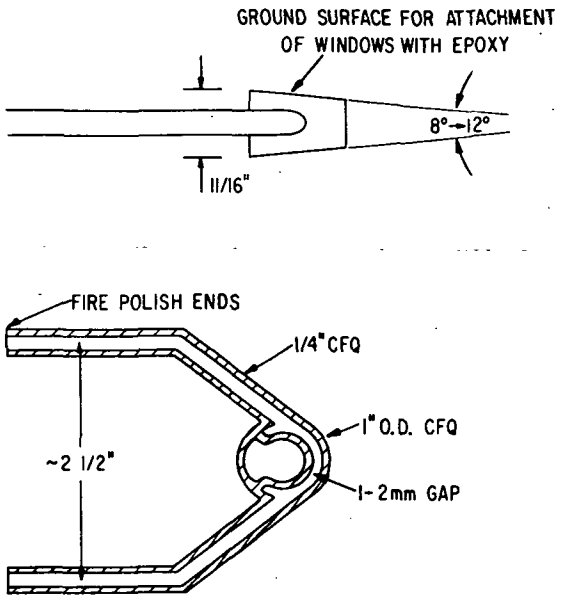

Figure 19 Flowing dye cell for N_2 Laser-Pumped Dye Laser.

To fully utilize the 58x58 mm grating a beam expander is used to expand the cross section of the light beam emitted from the thin lineal active region by a multiple of 51 times. This is accomplished with a 3.9 mm FL by 1.1 mm dia. input lens and a 200 mm FL by 50 mm dia. output lens. The lenses are near diffraction limited and AR coated for high transmissivity in the visible spectrum.

On the opposite side of the optically excited dye region is a parallel plate polarizer that consists of 10 cover glass slides placed at Brewster's angle and mounted in a rotatable mount that allows the linear polarization of the laser to be set at any desired angle about the laser beam. One surface of a 2" dia. glass plate that is slightly wedged and mounted in a Lansing AOD mount is used as the output reflector. The single surface reflector gives a 4% reflection and is quite adequate for the high gain achieved by the rhodamine 6G dye. The echelle grating and rotational mount, the beam expander, the parallel plate polarizer, and the output reflector are mounted on a 6" x 36" invar surface plate for good temperature stability.

The N_2 laser-pumped-dye laser system operates in the manner of a high gain two pass amplifier, rather than as a typical laser which builds up cavity radiation modes by amplifing multiple reflections between resonating reflectors (ref. 43). The oscillation is limited to the two passes made by the short (10 nsec) pump pulse, and the round trip transit time of the laser cavity. The small lineal active volume, which has a gain of about 10^3, amplifies the spontaneous emission, producing an observable amount of superradiance along its axis. The 4% of the superradiance which is reflected by the output mirror is reamplified 10^3 times when passing back through the active region. This signal is then expanded 51 times to fill the echelle grating. The retroreflected light from the grating is angularly dispersed and only a small fraction of the original light, that lying in a narrow angular (and therefore narrow spectral) range is recollimated by the beam expander and sent through the active region for its second amplification and passage through the output reflector. A 4 mm diameter aperture, placed after the output reflector, passes the laser beam and blocks most of the unwanted light which originates from the initial superradiance and from reflections off window and lens surfaces.

The spectral width of this system is determined entirely by the angular dispersion of the grating and beam expander combination and is limited, of course, by the maximum resolution of the exposed grating surface which in our case would be about 4×10^{-3} nm at 600 nm.

Laser performance characteristics. - The maximum average power obtained with the N_2 laser-pumped-dye laser using a 5×10^{-3} concentration of rhodamine 6G, was a little better than 10 mw as measured with a Coherent Radiation Model 205 thermopile. For this power level a Bausch and Lomb 1200 gr/mm grating was used in first order in place of the 300 gr/mm echelle grating and there was no polarizer in the laser. In this instance the emission linewidth integrated over several hundred laser pulses was about 4×10^{-2} nm, as estimated from Fabry-Perot interferograms. When the echelle grating was used (10th order) and the parallel plate polarizer placed in the laser cavity, the average power dropped to the 3 mw range. However, with this grating, the laser linewidth is about 5×10^{-3} nm, which is near the theoretical limit for the number of grooves exposed.

If the 4% output reflector is replaced with an uncoated fused quartz etalon of 14.7 mm thickness (FSR - 8.4×10^{-3} nm), the laser emission width narrows further to about 2 to 3×10^{-3} nm. With the etalon output reflector, however, the spectral output appears to "mode hop" as the laser is tuned by rotating the grating. Sometimes two laser emission lines appear at a separation corresponding to the free spectral range (FSR) of the etalon resonant reflector (8×10^{-3} nm). In some instances the "mode hopping" of the laser produces a 30% periodic variation of the laser output when the laser wavelength is continuously scanned. With the 4% output reflector, though, a single laser wavelength could be continuously scanned with no alteration of the output power.

The N_2 laser-pumped-dye laser has also been operated with the dye 4 methylumbelliferone (4-mu) in perchloric acid and ethanol solution (ref. 44). This dye forms a strong lasing exciplex (4 mu) H^+ in the acidic solution and lases from 460 nm to 560 nm depending on the perchloric acid concentration. The optimum concentration for laser output in ethanol is from 10^{-2} to 1.5×10^{-2} M of 4 mu and 1 to 3 M of perchloric acid with the 1 M perchloric acid concentration optimum for the green wavelengths and the 3M acid concentration for the blue-violet wavelengths. Typical average output power of 5 mw were achieved with the 1200 gr/mm grating in first order.

The angular divergence of the dye laser beam with the R6G dye was estimated to be 1.2 mrad (half angle) for the central bright spot. This divergence allows one to estimate the diameter of the active volume as 0.25 mm for a diffraction-limited wave. The 4 mu dye laser beam cross section, however, was an elongated ellipse and estimations of the half angle divergence gave 1 mrad for the vertical direction and about 12 mrad for the horizontal direction. The larger divergence in the horizontal direction indicates that the N_2 laser pumping radiation is absorbed within a depth of about 30 μm in the dye cell.

Second harmonic conversion. - A right angle dielectric reflector, coated for maximum reflectivity in the yellow-orange part of the spectrum, directs the dye laser beam through a 10 cm FL lens that brings the laser beam to a focus inside a 20 mm cube, ADP crystal whose z axis is oriented at 62° for frequency doubling at 590 nm. The ADP crystal is mounted in a Lansing AOD mount and by angulating the crystal relative to the laser beam the doubling frequency can be angle tuned a few tens of nm about the center wavelength of 590 nm. A calibrated Corning CS 7-54 filter is used immediately after the ADP crystal to completely block the visible laser beam and pass about 85% of the second harmonic.

A 5% conversion efficiency in frequency doubling to the uv is easily accomplished with the ADP crystal. After the losses of the filter and reflections losses from lenses and a right angle reflector are sustained, we easily achieve 100 μW average power at the scattering cell with 5×10^{-3} nm linewidths. The uv laser power is monitored using a slightly wedged quartz disk as a single surface reflector to direct 4% of the beam toward a diffuse ($BaSO_4$) scattering surface (cf. Fig. 18). A known solid angle of the scattered laser light is then detected by a calibrated ITT S-5 vacuum photodiode. The pulse energy is found to vary by 20 to 30% from laser shot to shot. However, the average power varies by no more than about ±3% from a mean value over a second or two of averaging. The large shot to shot variation in the laser pulse energy is probably due to thermo-optic distortions

created by hydrodynamic instabilities in the fluid flow through the active region of the dye cell. These effects average out, however, over several hundred laser shots.

Two other crystals were used for second harmonic generation of the visible dye laser light. A KDP (potassium dyhydrogen phosphate) crystal was purchased from Quantum Technology, Ltd. This crystal was 45° z cut for 90° (noncritical) phase matching near 595 nm at room temperature. The 90° phase matching angle can be temperature tuned to about 602 nm by heating the crystal to 100°C. With noncritical phase matching the SHG efficiencies should be greater than for critical phase matching (i. e., angle tuning) since there is no Poynting vector walk-off for the noncritical matching case. Using a 5. 5 cm F. L. lens to focus the 10 mW dye laser beam into the KDP crystal, uv light was generated when the laser wavelength was set on the proper phase matching wavelength for room temperature. The KDP crystal temporarily generated about 100 μW of UV power but quickly damaged with the generation of an inclusion in the crystal where the laser beam was focussed. In this instance the laser power density was clearly above damage threshold of the crystal. Estimates of the laser peak power density with the 5. 5 cm F. L. lens give over 500 Mw/cm^2, a value that can damage most crystals.

The third crystal used for SHG was lithium formate monohydrate (LFM). This crystal was first used by Singh et al. (ref. 45) for frequency doubling the 1. 06μ Nd lasers. Lithium format is of interest to us because it can be angle matched down to its absorption band edge near 230 nm. Our 1 cm^3 LFM crystal was purchased from Isomet and was protected from dehydration by immersion in a Dow-Corning silicone fluid and placed in a sealed container with an AR coated window for the visible input laser beam and a fused quartz output window for the SHG beam. The crystal was cut at 43° to the z-axis to allow angle phase matching at 275 nm with the laser beam at normal incidence to the crystal faces. Table II shows the results of our SHG measurements with LFM from second harmonic wavelengths of 250 nm to 230 nm. The measured phase matching angles (θ_p meas.) agree quite well with our computed values (θ_p comp) that were made from a projection of Singh's data in the ir and visible spectrum. The LFM crystal, however, was damaged by the optical radiation at all the above listed second harmonic wavelengths. It was found, for example, that at 250 nm the output power of the SHG radiation fell 5 to 10% after 10 min. of operation and a small white cloudy scattering center developed at the position of the laser beam focus in the crystal. This situation became more severe as we proceeded to the shorter wavelengths. The absorption of the uv radiation by the crystal becomes larger and this in turn causes a local temperature rise at the focus of the laser beam in the crystal that can become large enough to dehydrate the crystal and produce the white cloudy inclusions observed in the crystal. If the damage is thermo-optic as just described then the crystal or laser beam could be rotated to avoid overheating and consequent damage.

TABLE II

$\lambda_{2\omega}$ (nm)	θ_p meas.	θ_p comp.	SHG Conversion Efficiency With 10 cm FL lens	8 cm FL lens
250	40.6°	39°	3.1%	2.0%
245	39.8°	38.5°	2.3%	1.9%
240	38.9°	37.5°	2.3%	1.3%
235	37.9°	36.7°	1.7%	0.9%
230	36.3°	35.6°	---	0.3%

Spectrometer and Related Optics

The horizontally polarized UV beam generated by the ADP crystal passes through a 150 nm FL lens, and is then redirected vertically upward by a right angle, prism. The beam is brought to a focus at the center of a 5 cm dia. by 2 cm wide cylindrical scattering cell (cf. Fig. 18). The focus of the UV beam is centered 20 cm away from the entrance slit of the Spex model 1800, 3/4 meter, f 7.5 monochromator. A 50 mm FL quartz lens, held in translatable mounts and placed between the scattering cell and the monochromator slits, collects the light scattered at right angles from the laser beam, making a 1:1 image of the laser beam on the entrance slit of the monochromator. A crystal quartz polarization scrambler is placed ahead of the entrance slit to eliminate any polarization sensitivity of the monochromator to the incident light to be analyzed. The Spex monochromator has a 1200 gr/mm grating blazed at 300.0 nm and is used in first order. The resolution of the monochromator in first order is about 0.02 nm.

The wavelength of the monochromator was calibrated at seven different points in the uv using a low pressure Hg arc placed so as to illuminate the entire entrance slit and grating of the monochromator. The relative spectral response of the monochromator from 250 to 400 nm was also measured using a calibrated 200 watt GE quartz iodine lamp and a calibrated 6 1/2" square Corning CS 7-54 filter. The purpose of the filter is to reduce visible light from the source, which otherwise scatters within the spectrometer, causing a high background. Remnant background from visible light, plus the dark count, was evaluated using a Corning CS 0-54 filter which transmits light only at wavelengths longer than those of interest. The standard lamp illuminates a diffuse scattering surface constructed of Eastman high reflectance paint which is placed in front of the monochromator along the optic

axis of the collecting lens. The single photon photomultiplier pulses were counted in a specified time interval at many different wavelengths for the calibration. Signal linearity was checked by using uv calibrated neutral density filters.

Detection and Time-Analyzing Electronics

Figure 20 shows a schematic of the detection system used for either a spectral analysis or a time analysis of the scattered light. The output of the monochromator is sent to a EMI 9635 QAM Photomultiplier (PM) specially selected for low dark noise. The PM is mounted in a Products for Research TE 200 housing that is mounted at the exit slit of the monochromator. The light levels required for this system must be low enough so that we obtain either one or no detected photons for each laser pulse. Each detected photon pulse is amplified by a Kiethley Model 109, 50 Ω input, 20 db pulse amplifier that is placed at the output of the PM housing. The amplified pulses then go to an Ortec Model 463 constant fraction discriminator (CFD). The single photon pulses from the amplifier were monitored at the input of the CFD with an oscilloscope and found to vary in pulse height from about -50mV to -300mV with pulse widths of about 25 ns. The electrical noise pick up from the N_2 laser, on the other hand, was only a ±6mV signal. The CFD, which has a minimum input level of -50mV and therefore will not trigger on the electrical noise, is triggered to give an output pulse at a constant fraction of the input pulse height rather than at a constant input level. Triggering on a constant fraction of the pulse height substantially reduces the timing error (walk) that is caused by the varying single photon pulse heights generated by the PM. The output pulse from the CFD is sent to the stop input of an Ortec Model 437A time to pulse height converter (THC).

Initially, a Berkley 903 double pulse generator sends out two triggering pulses whose relative separation in time is adjustable. One pulse initiates the N_2 laser and the other pulse is sent to the start input of the THC. At a later time, determined by the time interval set on the double pulse generator, the delay in the triggering electronics, and the time response of the scattering species, the detected photon signal from the CFD may enter the stop input of the THC. If this pulse is within the time window viewed by the THC, it generates a pulse output from 0 to 10V whose height is proportional to the time interval between the start and stop input signals. The output of the THC is coupled to a Northern Scientific NS-710 pulse height analyzer (PHA). After several thousand laser pulses a time response of the scattering species is built up in the appropriate channels (or bins) of the PHA.

By counting a small range of pulse heights from the THC the detection system effectively time gates and consequently discriminates against unwanted background pulses that occur randomly in time. The minimum full scale time

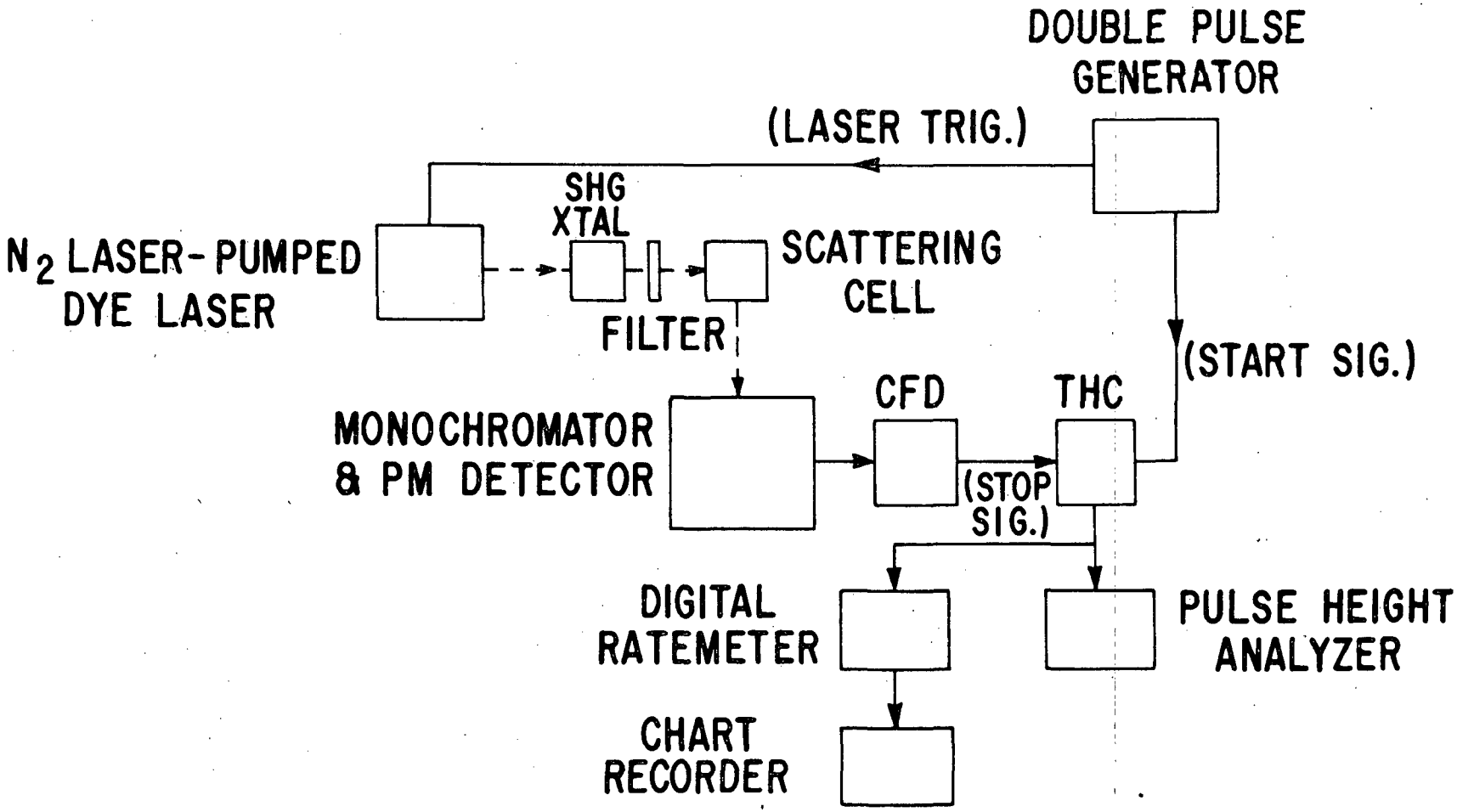

Figure 20. Block diagram of the Monochromator-Dye Laser Facility (MDLF) showing detection and analysis electronics.

range over which the THC can be set to detect a PM signal is 50 ns. This range is divided up into 1024 channels in the PHA or 50 ps per channel.

The output of the THC is also sent to a Tennelec TC 592P digital ratemeter which counts all the pulses from the THC regardless of height provided the lowest pulse height is set above the ratemeter threshold of 0.15V. This situation can be easily obtained by adjusting the time separation of the two pulses from the double pulse generator to give THC output pulses that lie above the ratemeter threshold. In this mode the THC serves as a coincidence gate. The digital ratemeter has an analog output that drives one pen of a dual pen strip chart recorder. The other pen on the recorder is driven by the output of the Kiethley electrometer that monitors the laser power. By scanning the laser wavelength at a fixed monochromator wavelength or vice versa, the scattering signal can be recorded as a function of laser wavelength (or monochromator wavelength) along with the average laser output power.

The THC and PHA were calibrated by using the two pulses from the double pulse generator to start and stop the THC. A dual beam oscilloscope monitored the start and stop input pulses. By setting the time interval between the pulses from the double pulse generator to different positions we calibrated the PHA with respect to the oscilloscope time scale.

By observing the number of PHA channels required for counting at fixed time interval of the double pulse generator, we could determine the jitter in the interval between the pulses to be 1 ns. This represents one limitation on the time resolution capabilities of our detection system. Figure 21 shows the results of data taken of the Rayleigh and Mie scattering from the laser beam in air. Each data point in Fig. 21 corresponds to a channel of the PHA. In this instance the THC range was set on 1 μs. Since there are 1024 channels covered by the 1 μs range the separation between each channel corresponds to about 1 nsec. Therefore, the half width of the pulse in Fig. 21 is about 6 ns. This width represents the average of many laser pulse widths plus the jitter in the triggering electronics as discussed above and any jitter in the initiation of the laser action. Thus, the time resolution of the system is determined to be 6 nsec.

Signal Counting Statistics

The maximum pulse repitition rate of the dye laser is limited by that of the pump laser to 100 Hz. In our experiments we usually ran the laser at the slightly lower frequency of 94 Hz, which is set by the double pulse generator. In this case the maximum signal rate that can be indicated by the detection system is 94 Hz. However, the indicated count rate begins to deviate significantly from true count rate below 20 cps. This behavior reflects the probability that more than one photon will be detected during the THC "on" period, since the THC responds only to the first detected photon.

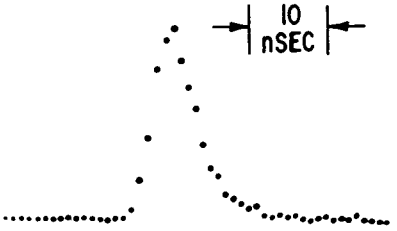

Figure 21 Time dependences of Rayleigh/Mie scattering as displayed by the multichannel analyzer. This result indicates the time response of the system to an "instantaneous" process.

The relationship between indicated count rate C_I and true count rate C_T can be determined from a simple statistical analysis, which yields

$$C_T = R \ln\left(\frac{R}{R-C_I}\right)$$

where R is the laser pulse rate. The ratio C_T/C_I is plotted in Fig. 22. Experimental data presented subsequently are corrected by this factor whenever appropriate.

Absolute N_2 Vibrational Raman Scattering Cross Section For Incident Light at 300.0 nm

This cross section for the vibrational RS from N_2 was measured using the SDLF in order to provide a standard against which to measure other cross sections (and effective cross sections). A typical RS signal from N_2 is shown in Fig. 23. The cross section value was obtained by measuring the ratio of Raman scattering to Rayleigh scattering at several different gas pressures (nominally 300, 500 and 700 Torr) and then multiplying this ratio, corrected for spectrometer response, by the theoretical value of the Rayleigh cross section, given by

$$\sigma_{Ray}^{TH} = \frac{4\pi^2}{\lambda_1^4}\left(\frac{n-1}{N}\right)^2$$

Here n is the refractive index measured at a molecule number density of N. A small depolarization correction (ref. 18) is omitted in this equation. Using $n-1 = 3.13 \times 10^{-4}$ for N_2 at 300 nm and STP, obtained from the International Critical Tables (ref. 46), we calculate

$$\sigma_{Ray}^{TH}(300\text{ nm}) = 6.60 \times 10^{-27}\ \text{cm}^2\ \text{sr}^{-1}$$

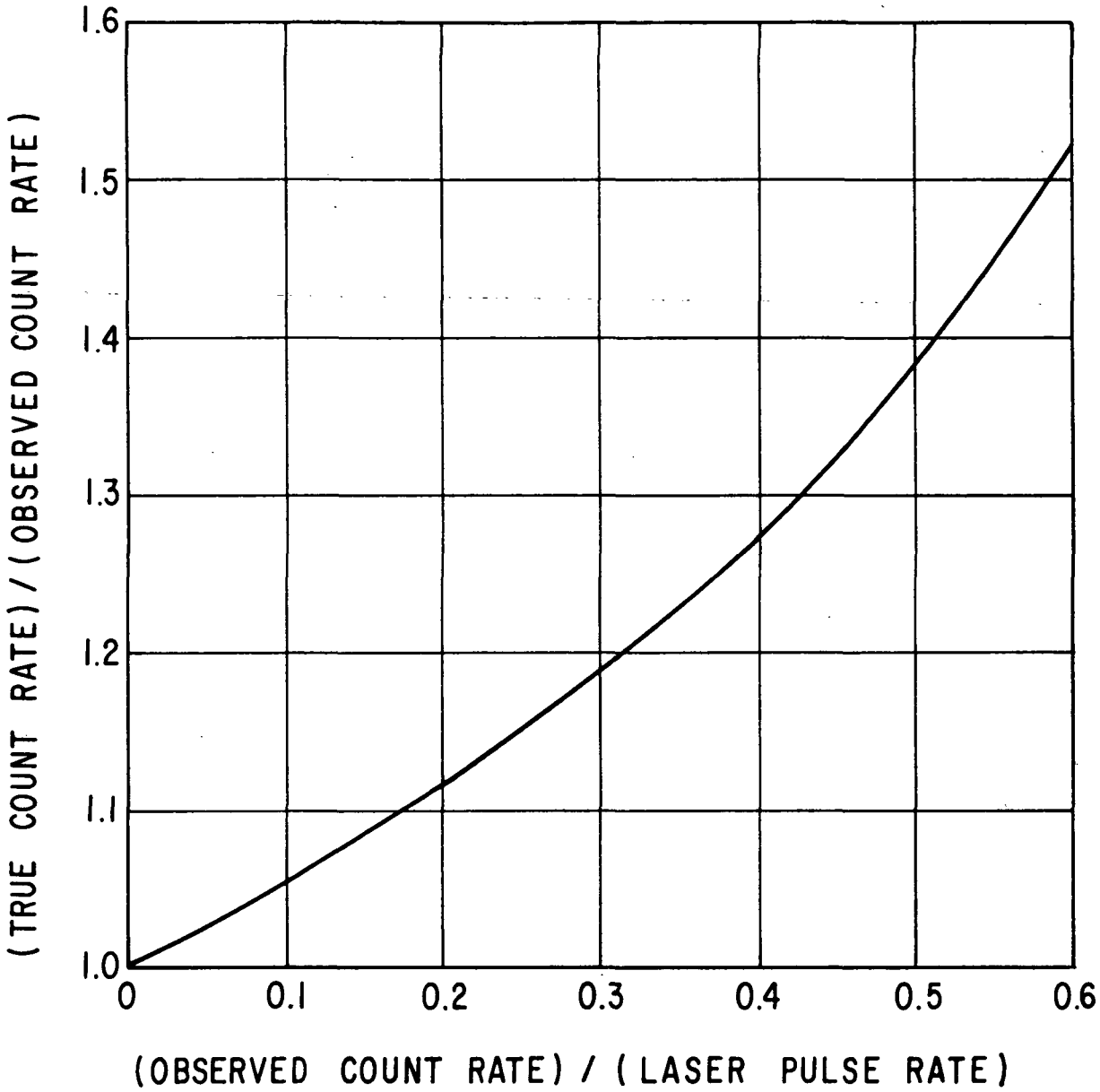

Figure 22 Relationship between true count rate and indicated count rate for the MDLF.

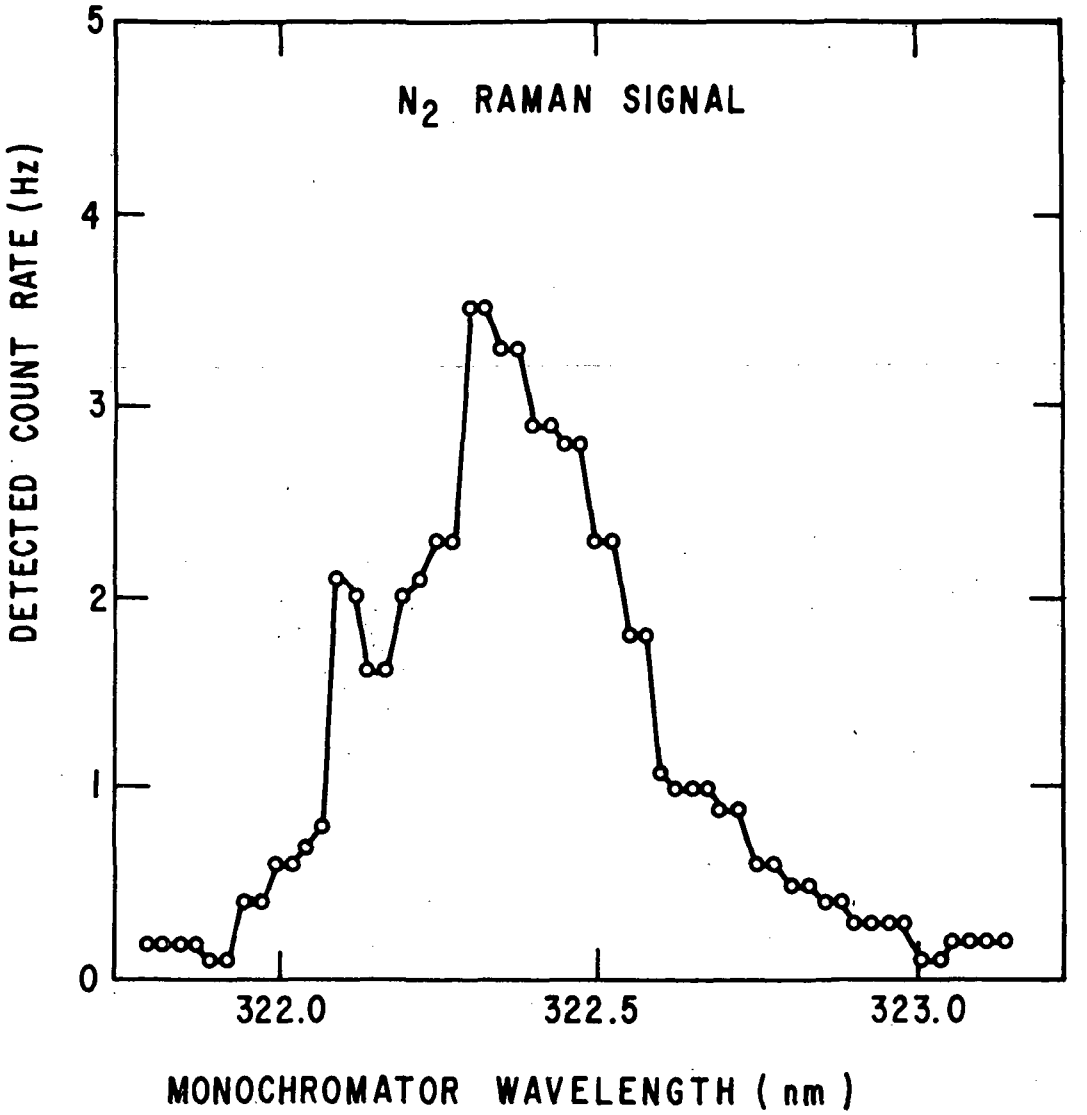

Figure 23 Typical signal obtained for vibrational Raman scattering from N_2 at 740 Torr.

The ratio $\sigma_{RAM}/\sigma_{RAY}$ was measured on two separate occasions in the SDLF using wide slits and a technique very similar to that described in ref. 40. The resulting values for this ratio were 1.50×10^{-3} and 1.44×10^{-3}. An average of these results yields

$$\sigma_{RAM}(N_2) = 0.97 \times 10^{-29} \text{ cm}^2/\text{sr} \pm 25\%$$

This cross section is for the Q-branch vibrational RS from N_2 summed over scattered light polarization in the right angle scattering geometry of Fig. 10. It is interesting to note that a $(1/\lambda_2)^4$ extrapolation of the value for the corresponding cross section measured at 514.5 nm (ref. 5) yields $0.463 \times 10^{-29} \text{cm}^2$. Thus the measured value is about 2.1 times larger than the extrapolated value. We believe that this weak enhancement is real. Indeed, the form of quantum mechanical expression for the cross section, Eq. (38), suggests that the cross section should increase faster than $(1/\lambda_2)^4$ over this wavelength interval because of the increased proximity to the strong vacuum UV resonances of N_2, which begin near 140 nm. The Rayleigh cross section also increases faster than $(1/\lambda_2)^4$. because of the dispersion of the refractive index, but the increase in the Raman cross section is more pronounced.

The O_2 Vibrational Raman Cross Section for Incident Light at 300 nm

We also measured the ratio of O_2 to N_2 Q-branch vibrational cross sections for incident light at 300 nm. This result yielded $1.59 \pm 20\%$ for the ratio, up from 1.24 at 514.5 nm for the cross sections summed over polarization. Thus the O_2 cross section increases faster than the N_2 cross section, which seems reasonable since the strong O_2 uv resonances begin at a longer wavelength (~230 nm).

Laser-Excited Fluorescence from SO_2

Sulphur dioxide exhibits relatively strong absorption between 260 and 320 nm, and much weaker absorption at longer wavelengths around 380 nm. As part of the work supported by this contract, we have examined the re-emission from SO_2 following narrow band (.005 nm), pulsed (5nsec) excitation at various wavelengths near 300 nm. We have observed the low pressure fluorescence and phosphorescence spectra, and the sensitivity of features of this spectra to exciting wavelength, self quenching and quenching by N_2 and air. In particular, we have found excitation wavelengths when the fluorescence shifted by the ν_1 vibration frequency is more than 10^4 times stronger in air near STP than vibrational Raman scattering from N_2. This fluorescence appears as a sharp peak rising over background continuum radiation. The sensitivity of the integrated peak intensity is such that it varies irregularly over a factor of two as the laser is tuned over a range of about 0.1 nm. These results are described in more detail below.

Low Pressure SO_2 Fluorescence

The absorption spectra of SO_2 has been studied and analyzed to some extent by several investigators (refs. 20, 47-53). To our knowledge N. Metropolis (ref. 51) has given the most accurate vibrational analysis of the ground to first excited singlet state transition bands in the 260-320 nm region. There is still some disagreement (ref. 53), however, over his assignment of the vibrationless (0, 0, 0)"-(0, 0, 0)' transition at 337.6 nm. A. J. Merer (ref. 52) has given a rotational analysis of the much weaker band system at longer wavelengths around 380 nm and demonstrated that these bands derive from a singlet-triplet transition.

The absorption spectrum of SO_2 near 300 nm has been shown in Fig. 9. The labeling of the bands A, B, C, . . . is due to Clements (ref. 47) who assigned these regularly spaced bands to a simple progression in the bending mode vibrational quantum ν_2. Metropolis, however, demonstrated that these bands are really a superposition of various higher combination bands which fortuitously create the appearance of a simple progression. The rotational substructure of these combination bands has not been analyzed to our knowledge. It is considerably complicated by the increased asymmetry of the molecule when excited to the first singlet state. Metropolis estimates a bond angle change from 120° to 100° when the molecule makes a transition to the first excited singlet state. The angle change is also accompanied by a change in the bond distances which eliminates the two-fold rotational symmetry that the molecule has in the ground electronic state.

For the SO_2 fluorescence measurements the scattering cell was filled with anhydrous grade (99.98%) SO_2 at pressures of a few tens of mTorr. We tuned the laser, whose bandwidth was 0.005 nm, through portions of the J, H, G, and F bands shown in Fig. 9 and examined the fluorescence output at the different laser wavelengths by scanning the monochromator from the laser wavelength out to longer wavelengths. In general the spectrum looked something like that reported by Mettee (ref. 20) who used a much broader Hg emission lamp for an excitation source. In our case a large continuum fluorescence occurs which reaches a maximum at about 340 nm. Superimposed on this continuum are many peaks whose positions relative to the exciting wavelength correspond to fundamental, overtone and combination tone vibrational levels in the ground electronic state. At certain laser wavelengths, however, it was observed that the fluorescence peaks became much stronger than the continuum fluorescence. In addition, the fluorescence peaks exhibited a shorter decay time than the continuum fluorescence. A particularly strong fluorescence peak whose wavelength was Stokes shifted by the ν_1 symmetric mode vibrational frequency was observed at 299.98 nm ± 0.04 nm, just to the short wavelength side of the peak of the G absorption band. This strong fluorescence peak is shown in Fig. 24 along with several

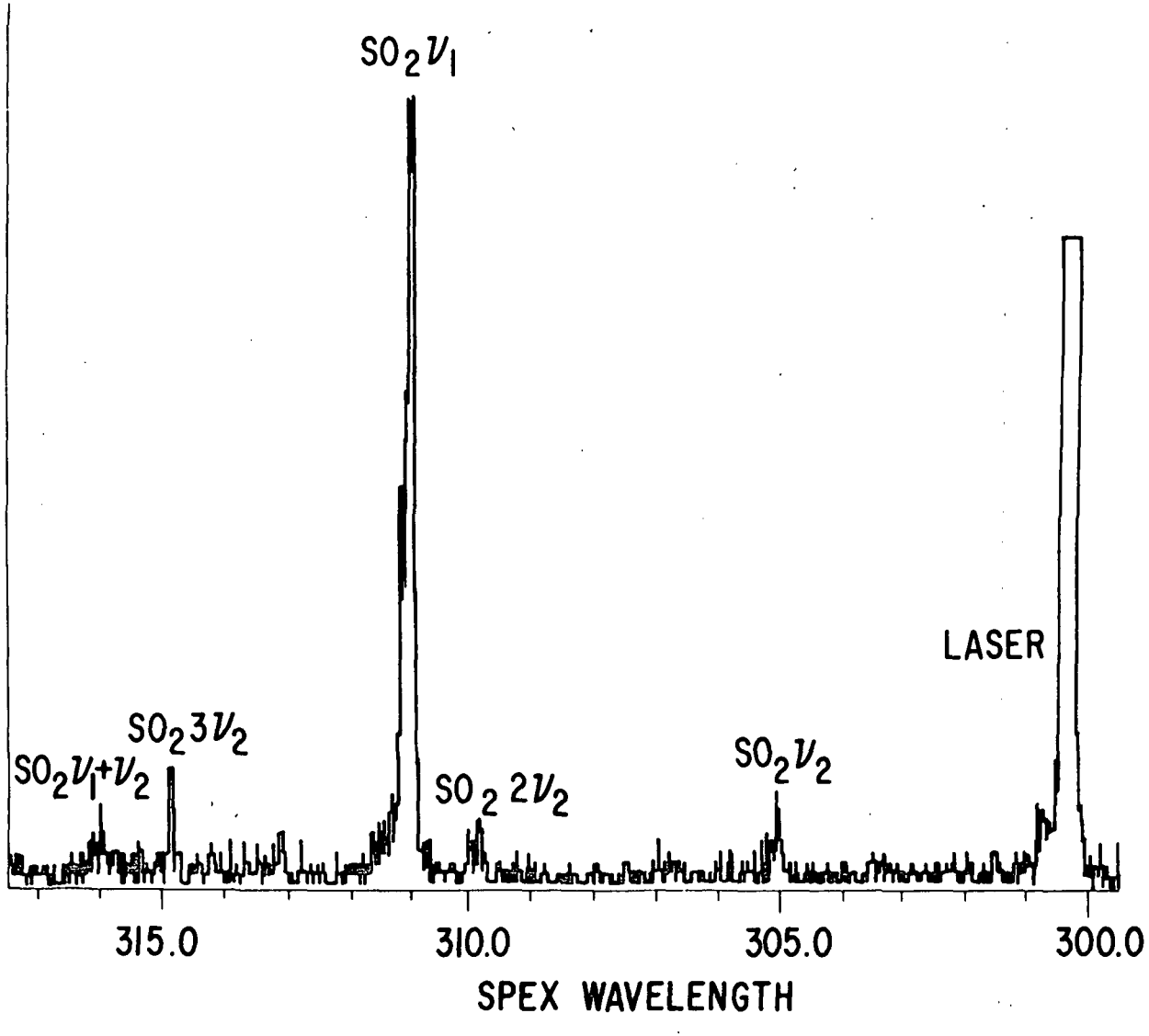

Figure 24 Fluorescence spectrum of low pressure (30 mTorr) SO_2 excited by light at 299.98 nm (corrected air wavelength) with bandwidth 0.005 nm.

other smaller peaks corresponding to overtone levels of the ν_2 bending mode, vibrational quantum and one peak that corresponds to a $\nu_1 + \nu_2$ combination tone level. The background between the peaks is mainly due to a continuum fluorescence emission. The actual background with no SO_2 in the scattering cell is considerably smaller than the continuum fluorescence. The spectrum for Fig. 24 was taken with about 10 mTorr of SO_2 in the scattering cell and 50 μm monochromator slits. The overtone and combination tone structure continues further out to longer wavelengths not shown in Fig. 24 with another moderately strong peak at about $3\nu_1$ (334.7 nm). When the laser is tuned only 0.08 nm away from the wavelength used for Fig. 24, the discrete spectrum falls off drastically leaving only a reduced ν_1 peak. The continuum fluorescence remains at about the same level, however. This is shown in Fig. 25 where the laser wavelength was reduced to 299.90 nm.

The sensitivity of the discrete fluorescence to incident wavelength can be further demonstrated by opening up the monochromator slits to obtain a semirectangular passband of 0.55 nm and monitoring the entire ν_1 fluorescence channel while tuning the laser wavelength over a small range of about 0.12 nm. A tuned laser fluorescence spectrum of this sort from 1 Torr of SO_2 is shown in Fig. 26. This data was obtained in the form of a histogram produced by the digital ratemeter counting for 10 sec intervals while the laser wavelength was swept at a rate of 1.16×10^{-4} nm/sec (i.e., one angular step of the grating every 5 sec). To produce Fig. 26 the data was taken from the histogram trace with a graphical digitizing system and placed on magnetic tape. Then the data was corrected for single photon detection by a computer, as described in the previous section and traced out on a convenient size scale by a digital plotter. The absolute wavelength measurements should be good to within ±0.04 nm. The laser wavelength timing per angular step of the laser grating was measured by stepping the grating 1000 steps with the digital drive and readout devices and taking the difference between two wavelength measurements before and after the 1000 steps. From this measurement it was determined that the tuning rate was 5.8×10^{-4} nm per step. Since the accuracy of this measurement was only about 10%, the accuracy of the wavelength scale in Fig. 26 is only 10%. The linearity of the scale is good to about 0.1% however.

From Fig. 26 we see that the fluorescence into the ν_1 channel shows a good deal of fine structure when the laser is tuned over this region of the spectrum. Strong structure was also seen at other regions of the spectrum. For example, four strong peaks were observed when tuning the laser through a region of the J band near 296.08 nm and observing the fluorescence in the $\nu_1 + 2\nu_2$ channel (217.6 cm^{-1}) at 316.47 nm. A large part of the tuned laser fluorescence (TLF) spectrum, however, did not show a strong fine structure. It was felt that the TLF spectrum in Fig. 26 corresponds to absorption between certain rotational levels in the two electronic states of the SO_2

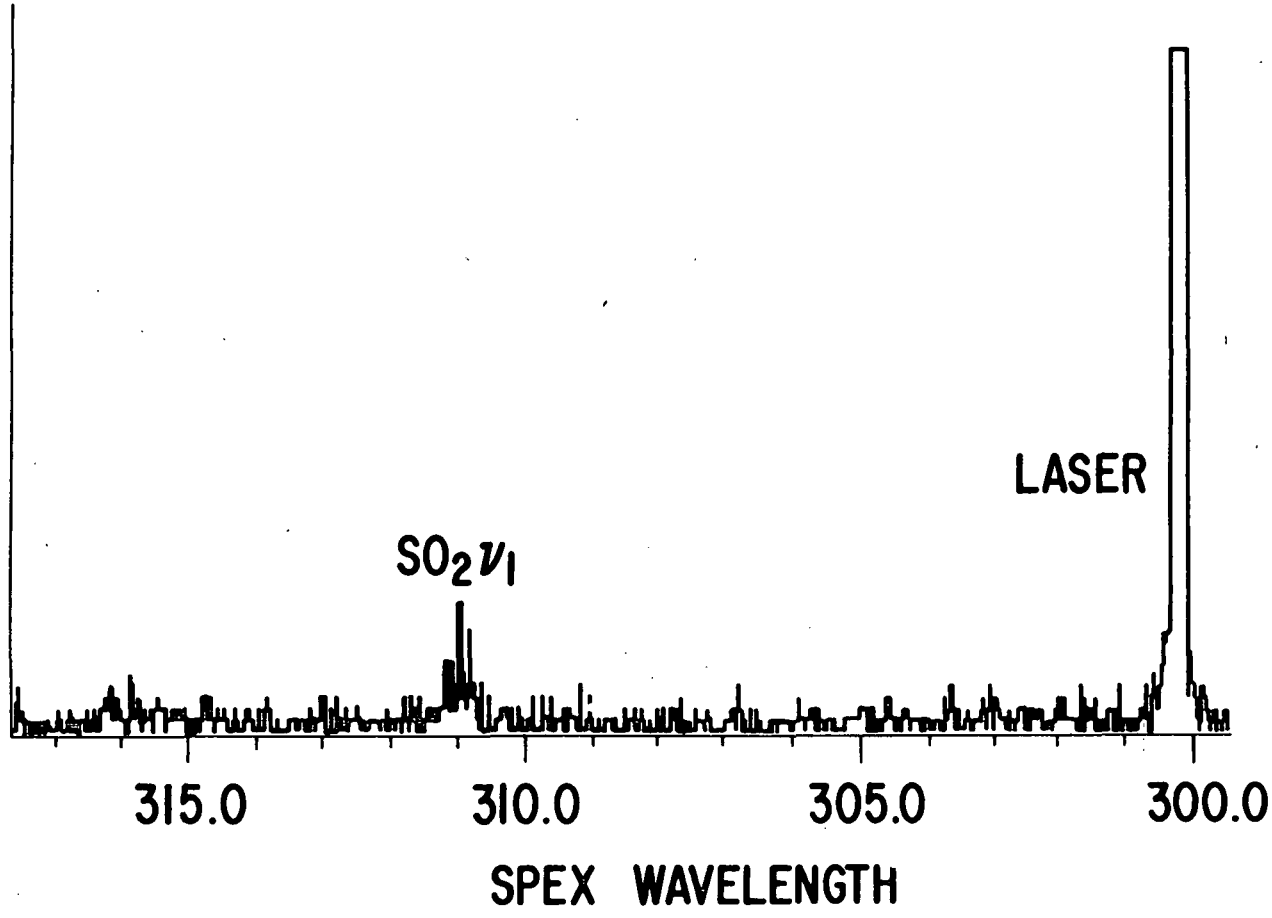

Figure 25 Fluorescence spectrum of low pressure (30 mTorr) SO_2 excited at 299.90 nm (corrected air wavelength).

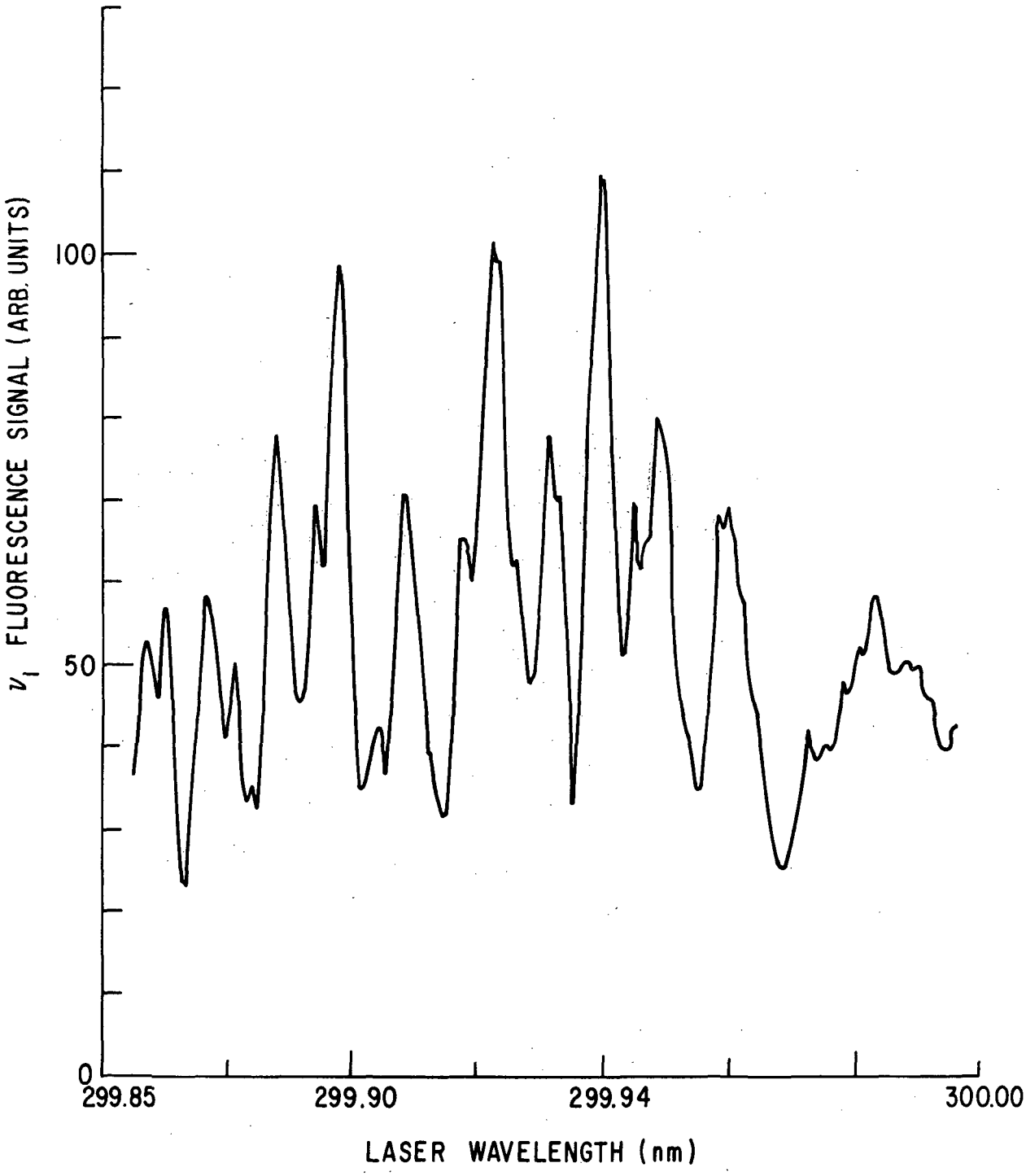

Figure 26 Tuned Laser Fluorescence (TLF) spectrum of SO_2. The monochromator slit function used to obtain this data is semi-rectangular with width 0.55 nm, centered on the ν_1 fluorescence line.

molecule. To verify this speculation Dr. R. J. Exton at NASA Langley Research Center has taken the absorption spectrum of SO_2 with a 2 m Czerny-Turner spectrometer in 3rd order with resolutions of 2.3×10^{-3} nm and 4.6×10^{-3} nm in the same region of the G band. The absorption cell used was 305 cm long (one pass) and filled with 50 mTorr of SO_2. A high pressure Hg lamp was used as the source light for the absorption measurements. Exton's absorption curves also show some structure in this region of the spectrum superimposed on a larger continuum absorption. In comparing the two sets of data, it was found that when the TLF curve was shifted by 6.8×10^{-2} nm, which could allow for wavelength measurement inaccuracies, there was striking correspondence between the peaks in the absorption curve and the peaks in the TLF curve. This correspondence is shown in Fig. 27 where the TLF spectrum (upper trace) is compared with the 2.3×10^{-3} nm resolution absorption spectrum (lower trace). It appears that the TLF spectrum shows with much greater contrast the structure in absorption which is superimposed on the continuum background absorption. The higher contrast in the TLF spectrum occurs because this measurement detects only the absorbed light that is emitted into the ν_1 fluorescence channel while the absorption spectrum includes all the light that is absorbed at the particular wavelength and either emitted into a broad continuum and many fluorescence peaks or nonradiatively de-excited.

Time Dependence of the Re-emission From SO_2: - The time dependence of the ν_1-shifted re-emission was examined using the 6 nsec resolution capability of the SDLF. In particular we were searching for a fast re-emission component characteristic of scattering. At very low gas pressures ($\lesssim 1$ mTorr) a significant fraction of the excited SO_2 molecules can diffuse out of the volume viewed by the spectrometer entrance slits before re-emission. Thus we do not expect to observe the intrinsic lifetime of the SO_2 re-emission. However, any anomolously fast component should have been detectable. None was observed in experiments at a number of different wavelengths. However, another interesting effect was observed. Super-imposed on the quasi-exponential decay following pulsed excitation at several wavelengths is a sinusoidal component which oscillates at a frequency of about 100 MHz. This feature is clearly visible in Fig. 28. It is possible that this effect is real, rather than an experimental artifact, because it is not observed at all excitation wavelengths, but it seems to be repeatable at certain wavelengths. The oscillation may arise from an exchange of excitation energy back and forth between the originally excited state and other states, perhaps in the triplet manifold responsible for the phosphorescence observed near 380 nm. A possibly analogous oscillatory exchange of energy occurs in the system of two coupled oscillators. Presently we are attempting a more detailed theoretical analysis of this possible effect in SO_2, and simultaneously extending our experimental observations.

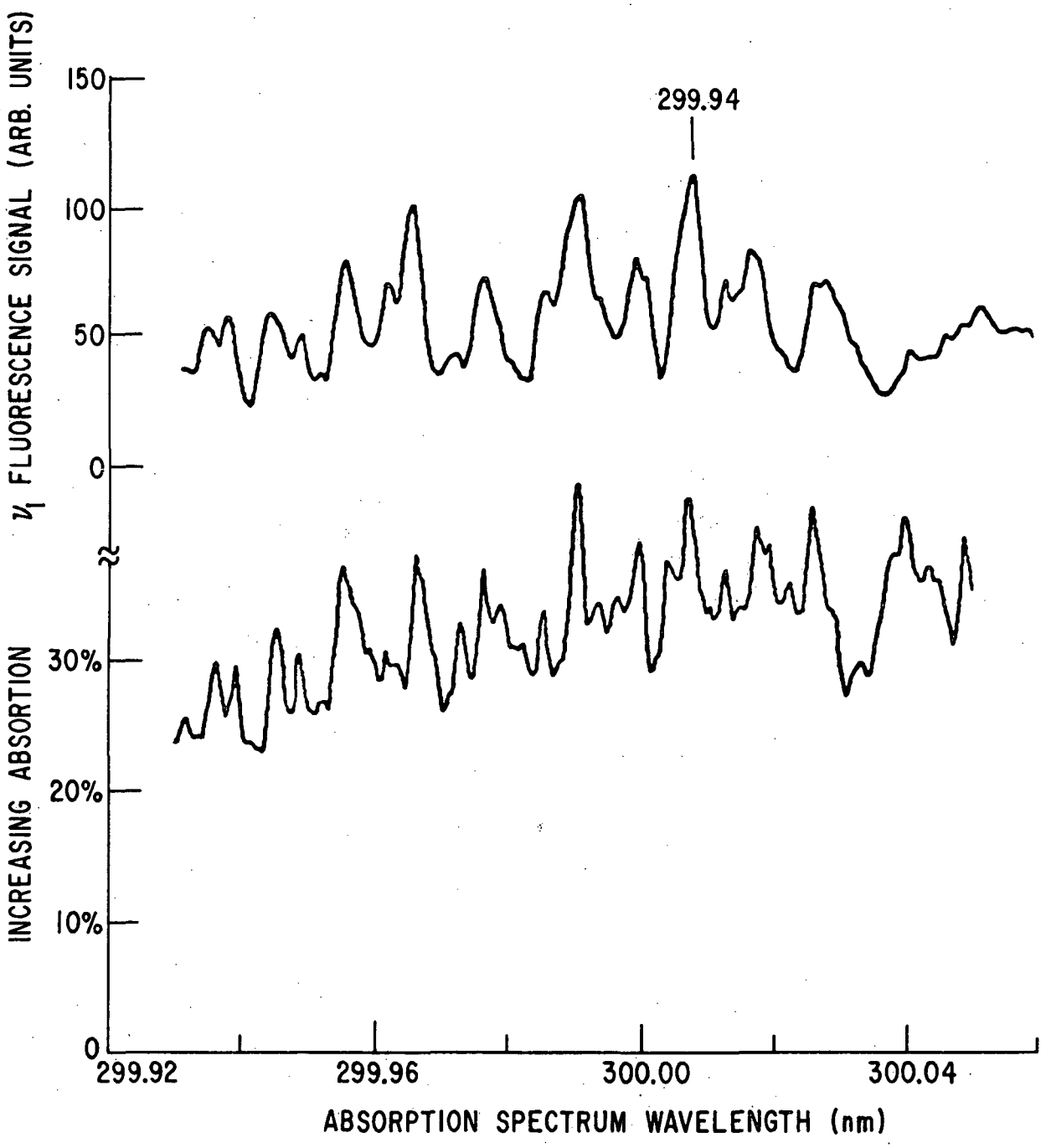

Figure 27 Comparison of TLF and absorption spectra, with variations adjusted to the same amplitude. The wavelength scale of the TLF spectrums has been shifted from its original calibration to match the absorption spectrum obtained by Dr. R. J. Exton at NASA Langley Research Center. The TLF spectrum was obtained with a laser bandwidth of 0.005 nm and monochromator bandwidth of 0.55 nm, centered on the ν_1 line fluorescence. The absorption spectrum was obtained with a slit function resolution of 0.0023 nm.

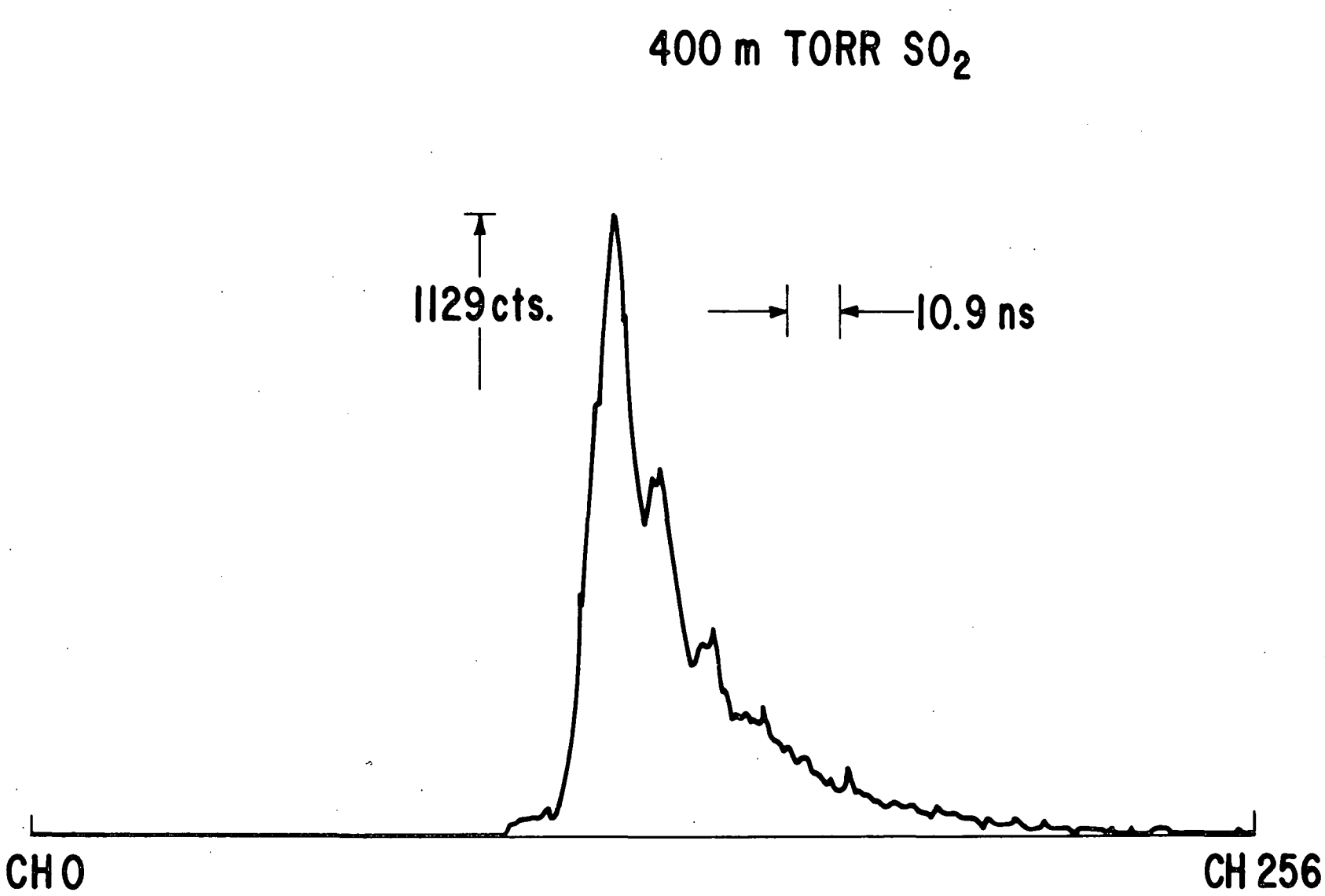

Figure 28 Time dependence of ν_1-shifted re-emission excited by a 5-nsec, 0.005 nm light pulse at a wavelength near 300 nm.

As the SO_2 pressure is increased from a few mTorr to 10 Torr, the fluorescence intensity integrated over time was observed to remain nearly constant. This result obtains because of the compensation between increased absorption and quenching discussed subsequently. However, the fluorescence decay time, which is governed by the radiative and non-radiative decay rates of the excited level from which the fluorescence originates, decreases steadily as the pressure increases. For pressures of SO_2 greater than about 10 Torr the self quenching was observed to reduce the decay time to less than the 5 nsec laser pulse width.

Self-Quenching in SO_2. - H. D. Mettee (ref. 20) in his article on the luminescence from SO_2 vapor has shown, by producing Stern-Volmer plots for low pressures, that the principal decay mechanism of an isolated SO_2 molecule excited to the first singlet state is by fluorescence and that any vibrational relaxation prior to emission is slight. In addition, Mettee concluded that electronic self quenching occurs at nearly every gas kinetic collision, with a cross section of $.188\ nm^2$.

Mettee's experiments employed relatively broad band non-laser excitation. In our narrow band self-quenching experiments, the scattering cell was pumped out to about 5 mTorr residual pressure through a stainless steel extension tube which runs from the scattering cell to a pumping and gas handling station. An Eck and Krebs valve of glass and Teflon polymer connects the scattering cell to a flexible stainless steel bellows which is connected to the extension tube. The flexible tubing allows the scattering cell to be translated in and out of the laser beam without disconnecting any of the tubing. The vacuum pump valve was closed and 10.8 Torr of anhydrous grade SO_2 was admitted to the scattering cell and connecting tubing. The pressure was monitored with a Dow Corning 704 oil manometer. With the monochromator slits set on 50 μm, a 40 second count was taken at 310.71 nm on the ν_1 fluorescent peak and at 311.71 nm on the continuum fluorescence. The laser wavelength was set at 299.96 nm and the power incident on the scattering cell was about 66 μw. The laser power was measured with and without the scattering cell in the laser beam in order to determine the insertion loss of the cell and absorption of the SO_2 gas. The scattering cell was then pumped down to four successively lower pressures and the above procedure repeated. The absorption coefficient measured from the slope of the log plot from the data was $0.038\ cm^{-1}\ Torr^{-1}$. This agrees with Exton's high resolution absorption measurements and P. Warneck's published results (ref. 53) for the absorption of SO_2 at the 300.0 nm wavelength.

Figure 29 is a plot of our measurements of the fractional absorption divided by the self quenched fluorescence signal in the ν_1 channel for the 5 different pressures. It is seen that the data is nearly linear with an intercept of zero; i. e., it follows the usual Stern-Volmer dependence. In the

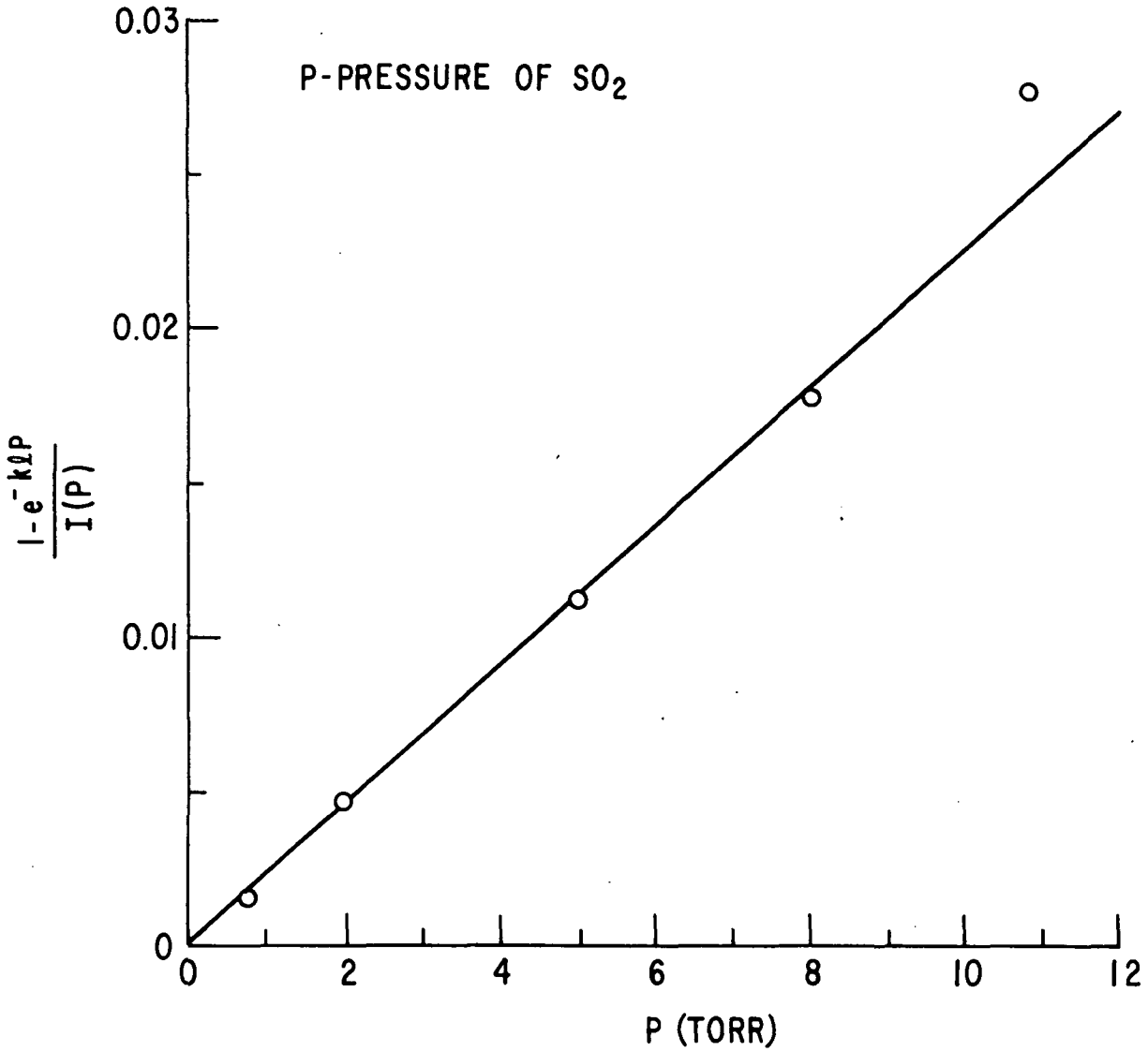

Figure 29 Stern-Volmer plot of SO_2 self-quenching.

regime where the absorption is small the exponential factor $1-e^{-\alpha \ell P_s}$ is approximated by $\alpha \ell P_s$ and the detected signal I_s is nearly independent of pressure. In this case any increase in the fluorescence from an increase in gas density would be cancelled by a corresponding increase in self quenching.

Quenching of SO_2 Fluorescence by Air. - Figure 30 shows a quenched fluorescence spectrum from SO_2 excited at 299.96 nm when 700 Torr of N_2 is added to one Torr of SO_2. In this case the ν_1 fluorescence peak was reduced in amplitude by a factor of about 190 when the buffer gas was added. The N_2 Raman signal can also be barely seen in Fig. 30 along with two other quenched fluorescence peaks shifted by the ν_2 and ν_3 vibrational quanta of SO_2. Further out in the spectrum than shown in Fig. 30, in the 380-450 nm region, there are several phosphorescence bands whose intensities are almost as great as the partially quenched ν_1 fluorescence peak. Mettee has demonstrated that the phosphorescence levels are populated predominantly by collisions. The phosphorescence lifetimes were observed to be several microseconds long. When the room lights are turned out the faint blue phosphorescence emission from the laser beam in the scattering cell can also be observed visually.

For the buffer gas quenching experiments the scattering cell was filled with SO_2 gas at a pressure between 1 and 10 Torr. The Eck and Krebs value at the cell was closed and the fill line and gas handling system pumped down to about 5 mTorr. The vacuum pump valve was then shut off and either N_2 from a laboratory bottle or air from the laboratory at about 100 Torr was admitted into the scattering cell and fill line. The N_2 or air buffer gas pressure was monitored with a Hg manometer. The valve at the scattering cell was cracked open and the pressure of the buffer gas was reset to 100 Torr. It was found by monitoring the fluorescence signal and the absorption of the laser beam through the scattering cell that the time required for the gas mixing was from between 5 and 10 min. After the buffer gas fill, the valve at the scattering cell was shut off and 15 to 20 min. was allowed before data was taken. Using 500 μm input and output slits on the monochromator, a 40 sec. count was taken on and off of the ν_1 fluorescence peak as described in the self quenching measurements. The power level of the laser was monitored and adjusted to keep the detected signal rate from saturating the photomultiplier. These measurements were repeated for several more increments of buffer gas pressure up to 700 Torr. Several measurements were taken with the N_2 buffer gas at 900 Torr. After the buffer gas quenching data was taken the cell was pumped out and flushed several times with N_2. The N_2 Raman signal was then measured with 700 Torr of N_2 in the cell. A background signal was then measured by shifting the monochromator 1.0 nm off of the ν_1 fluorescence wavelength. The data was then reduced by correcting the count rate for single photon counts as described earlier and then normalizing the count rates which were taken at different laser power

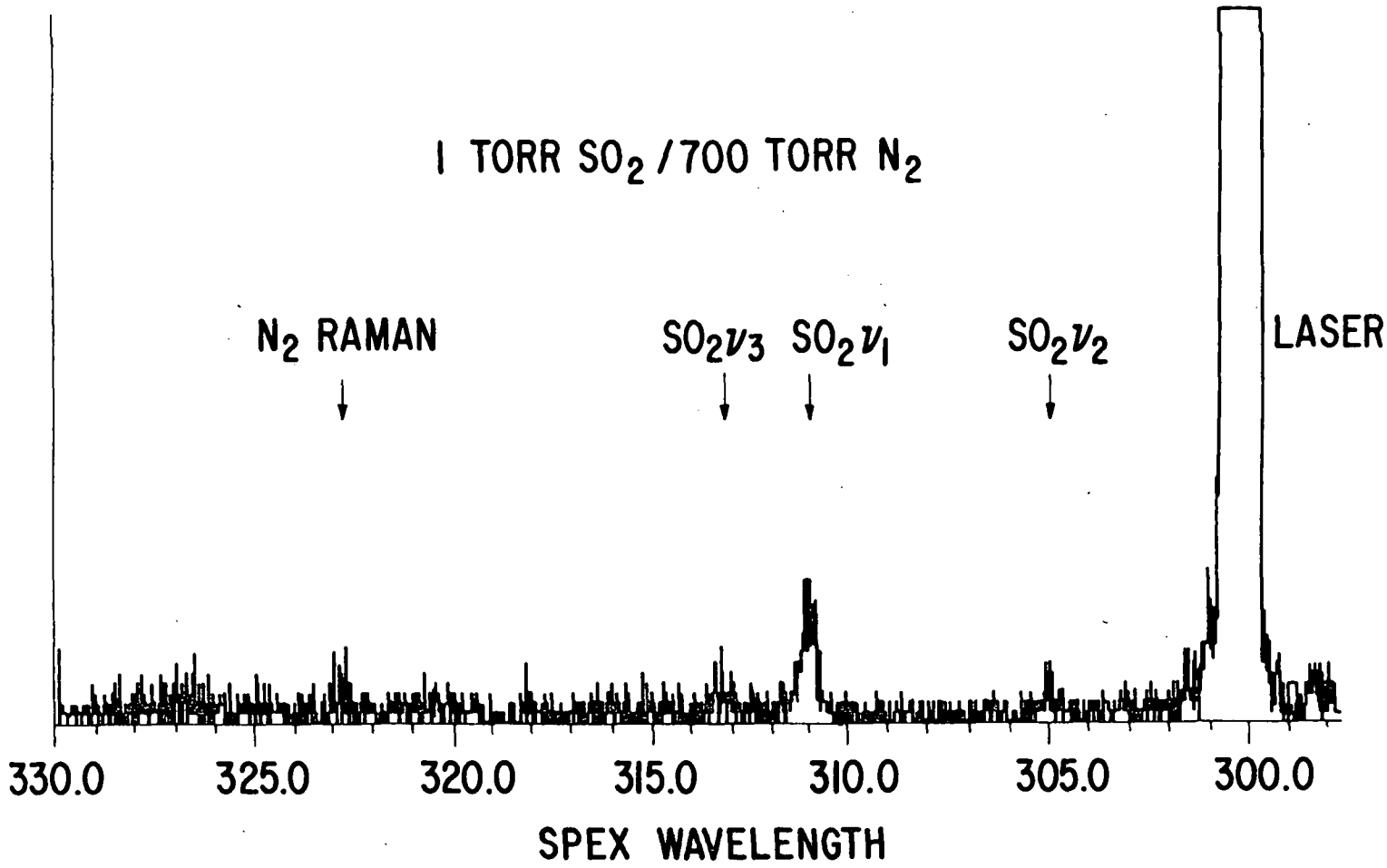

Figure 30 Fluorescence spectrum of SO_2 in 700 Torr N_2. The SO_2 fluorescence is excited by incident light of bandwidth 0.005 nm at 299.96 nm.

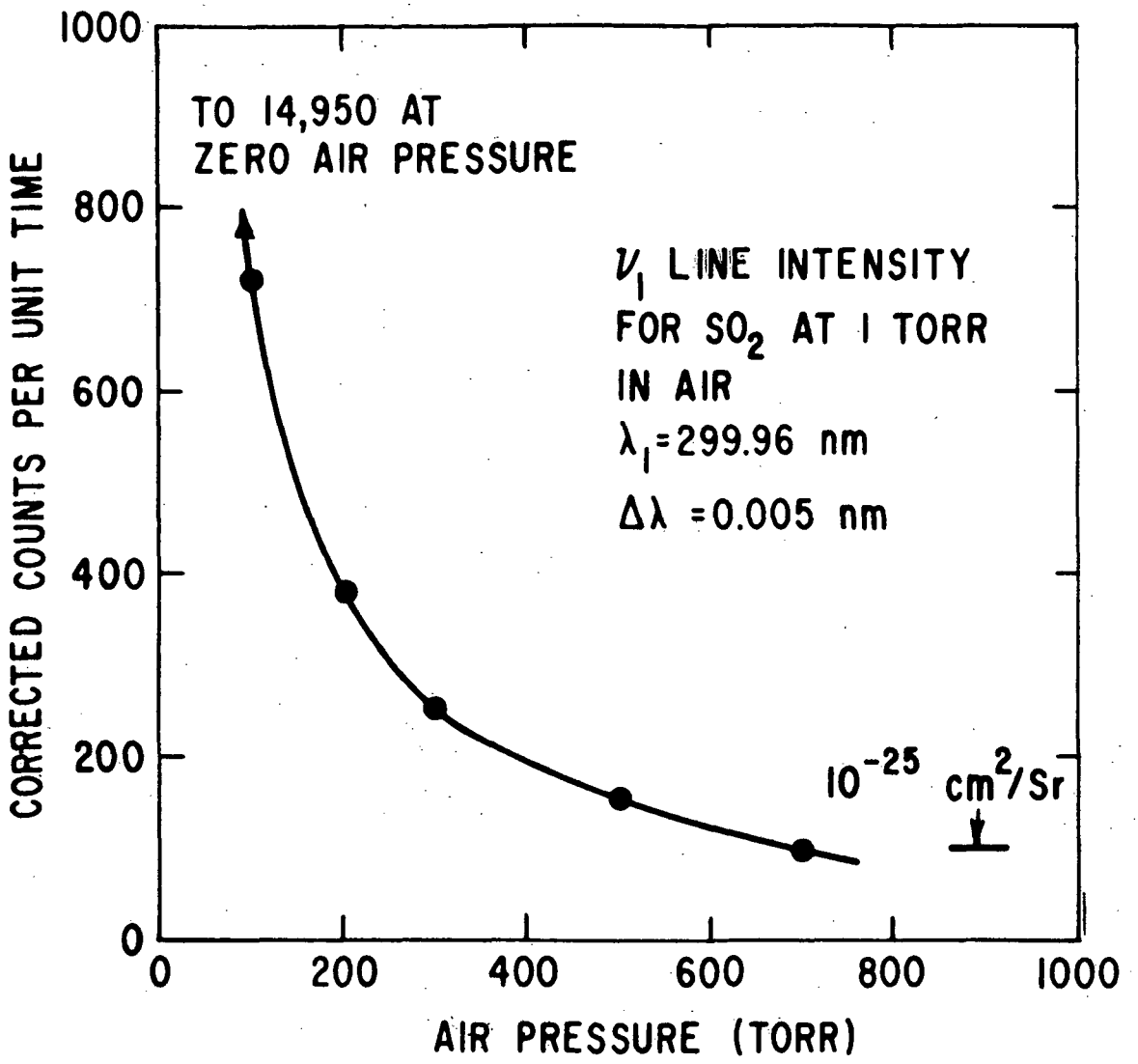

Figure 31 Intensity of ν_1-line fluorescence from SO_2 as a function of background air pressure. The SO_2 fluorescence is excited by incident light of bandwidth 0.005 nm at 299.96 nm. The effective cross section for ν_1-fluorescence, measured by comparison to N_2 vibrational Raman scattering, is shown in the figure.

levels to a common power level. The background count rate, which was only 0.2 Hz was then subtracted from the data.

Figure 31 shows our results for quenching of the ν_1 fluorescence from 1 Torr of SO_2 with the laboratory air as a buffer gas at five different pressures.

This figure demonstrates quite clearly that the variations of the SO_2 ν_1 line intensity is quite small over the normal range of variation of atmospheric pressures. Also shown here is the effective differential cross section for fluorescence into the ν_1 line by SO_2 in 700 Torr for air pressure. This cross section was determined by comparison against N_2 vibrational Raman scattering, using the previously measured absolute cross section for the latter at 300 nm excitation. The result obtained is

$$\sigma\ (SO_2, \nu_1) = 1 \times 10^{-25}\ cm^2/sr \pm 35\%$$

where the error estimate derives partly from the uncertainty in the N_2 cross section (±25%) and partly from statistical uncertainty in the SO_2 and N_2 count rates in the comparison measurement. It is significant that the SO_2 cross section is about four orders of magntidue stronger than that for N_2 excited 300 nm.

The results for air quenching of the SO_2 ν_1 line are displayed in terms of a Stern-Volmer plot in Fig. 32. As in the case of SO_2 self quenching, the linearity of this plot suggests that SO_2 absorption and subsequent fluorescence arises from a quasi-continuum. [See the discussion leading to Eq. (83)].

In order to determine the sensitivity of the ν_1 peak intensity to laser wavelength in the case of strong quenching, the spectrometer slits were again set to produce a wide (0.5 nm) semi-rectangular slit function and the laser was set to scan a small range. The resulting signal is shown in Fig. 33. Although this signal is quite a bit noisier than the corresponding low pressure result shown in Fig. 26, it is clear that there is some signal variation. From this and other results we estimate the variation to be on the order of ±30% over the tuning range shown.

In another experiment the monochromator wavelength was shifted to 311.71 nm, about 1 nm from the ν_1 peak, where the detected signal was from the continuum fluorescence. It was found that the continuum fluorescence at 311.71 nm also quenched at approximately the same rate as the ν_1 fluorescence peak. It was also found that quenching of 1 Torr of SO_2 with N_2 from a laboratory bottle of nitrogen gave the same results as quenching with the laboratory air. In addition, using nitrogen pressures up to 900 Torr in the scattering cell, we found that the quenching was still defined by the linear Stern-Volmer plot as in Fig. 32. No evidence of a deviation suggestive of scattering (i.e., an unquenched component of re-emission) was seen in any of these experiments.

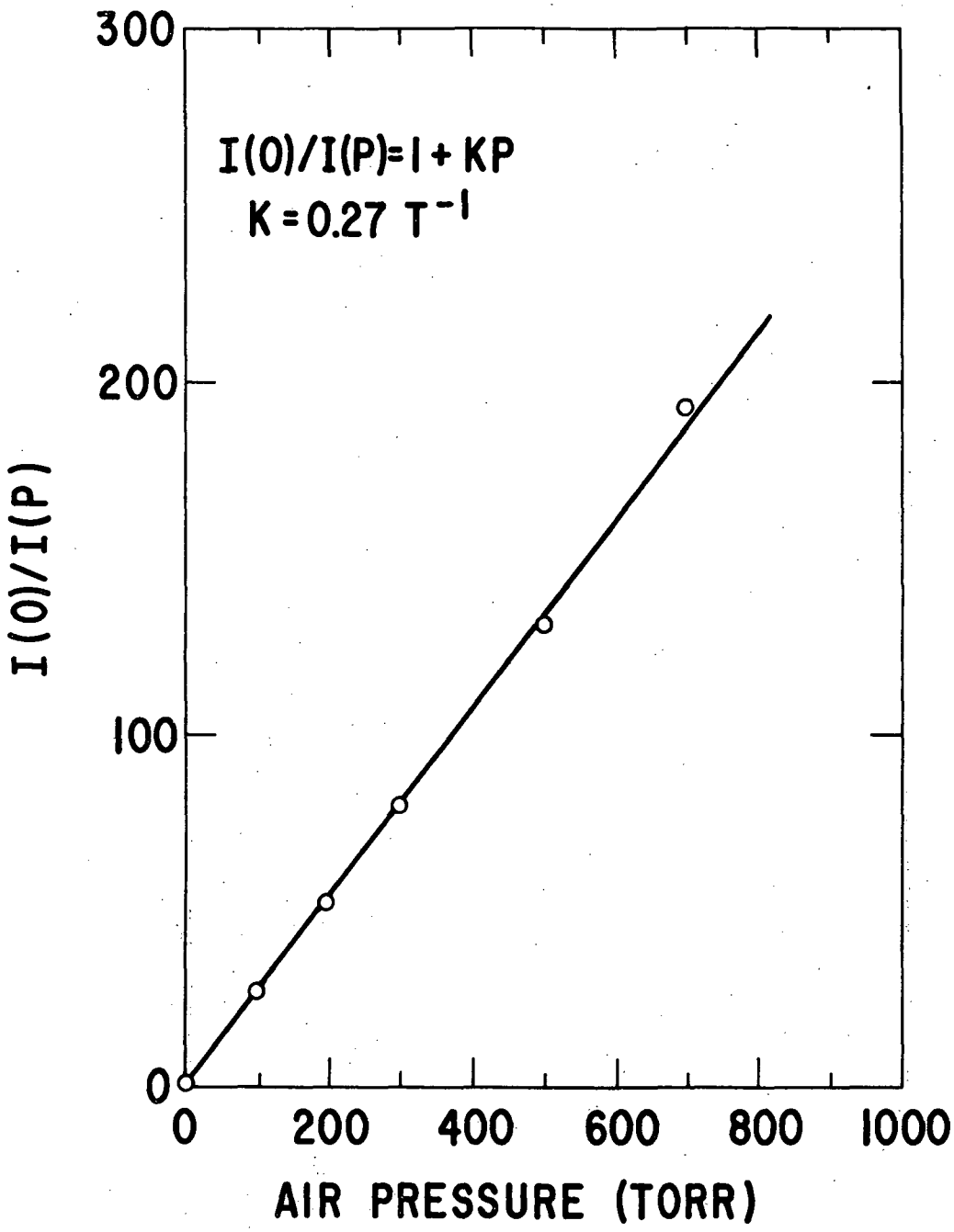

Figure 32 Stern-Volmer plot of SO_2 quenching by air, derived from data shown in Fig. 31.

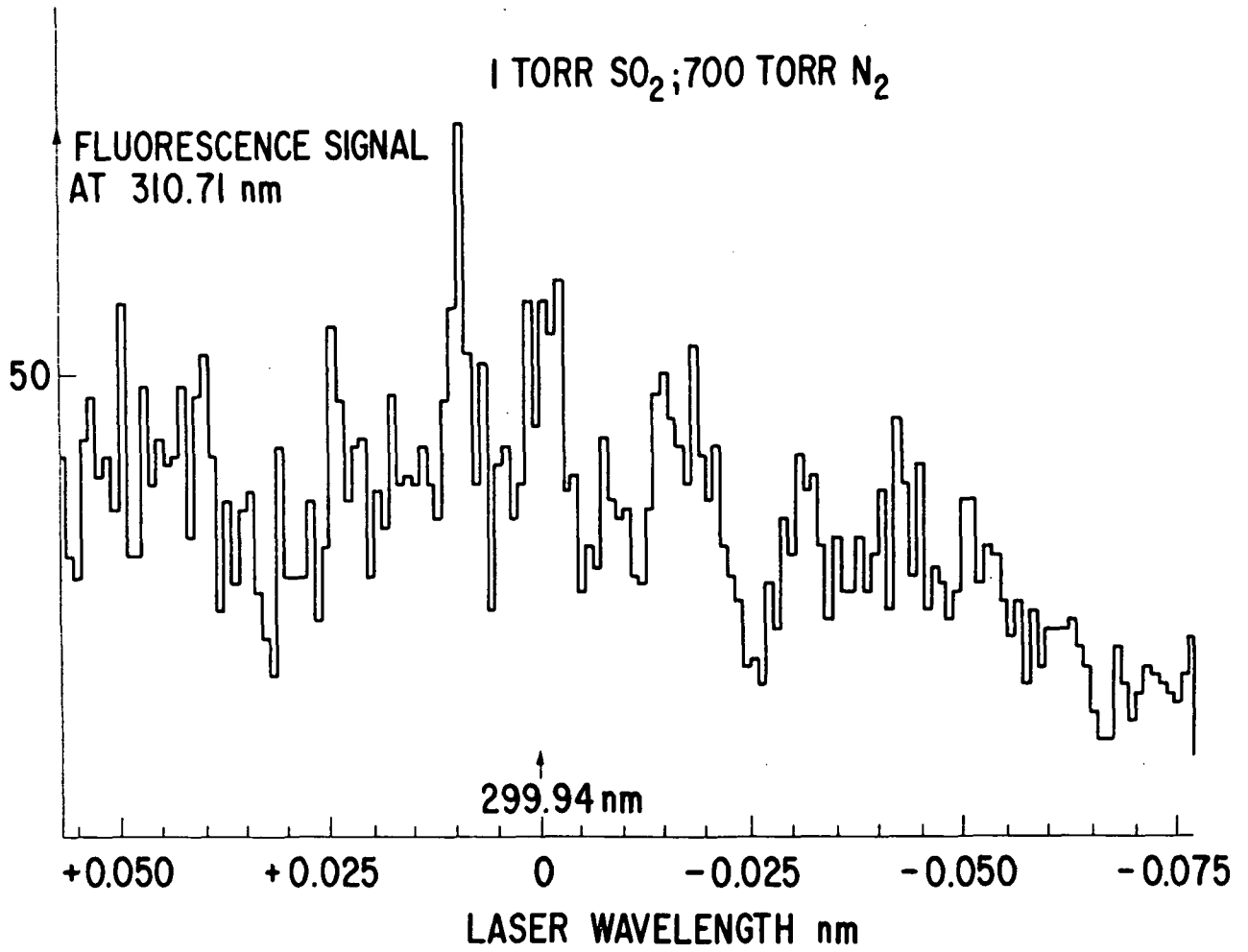

Figure 33 Tuned laser fluorescence spectrum of SO_2 ν_1-line in air.

A final point to be mentioned in this section is the polarization of the ν_1 fluorescence. The depolarization ratio ρ as defined previously was measured using a uv-polarizer in the filter holder in front of the monochromator collecting lens. The depolarization ratio for the ν_1 fluorescence at one Torr of SO_2 was 0.71. When 700 Torr of N_2 buffer gas was added to the scattering cell the depolarization increased to unity. This increase in depolarization is further evidence of the lack of a scattering signal (ref. 4).

IV. MODEL CALCULATIONS

In this chapter we consider several examples of applications of the results obtained in this work.

Ground Based Lower Atmosphere Probe

The large quenched fluorescence cross section found for SO_2 opens the possibility for concentration measurements of this gas at low concentrations. Initially, we consider two potential applications: measurement of source levels and measurement of ambient levels in the lower atmosphere.

A typical source of SO_2 is a smokestack whose effluent contains on the order of 100 ppm of SO_2 in nitrogen with other minor constituents. Suppose that the SO_2 concentration in the effluent is to be monitored from a distance of 200 meters by a LIDAR system transmitting light at a wavelength of 300 nm. The number of detected photons per joule of transmitted energy is given by

$$n = \frac{\rho\sigma L A \epsilon \eta T}{E_\lambda R^2} \tag{88}$$

where ρ is the number density of observed molecules, σ is the differential cross section (area/steradian) for the observed re-emitted light, L is the path length from which re-emission is observed. A is the area over which returned light is collected, ϵ is the optical efficiency, η is detector quantum efficiency, T is the two-way atmospheric transmission, E_λ is the scattered light photon energy in joules and R is the range. We assume the following system parameters:

$$\begin{aligned} \rho &= 2.7 \times 10^{15}\ \text{cm}^3\ \text{(100 ppm at STP)} \\ L &= 3\ \text{m} \\ A &= 1\ \text{m}^2 \\ \epsilon &= 10\% \\ \eta &= 20\% \\ T &= 50\% \\ E_\lambda &= 6 \times 10^{-19}\ \text{J} \\ R &= 200\ \text{m} \end{aligned}$$

Then, using the effective differential cross section found for the ν_1 line of SO_2 excited by 300 nm (nominal) radiation in air at STP,

$$\sigma = 1.0 \times 10^{-25}\ \text{cm}^2/\text{sr}$$

we obtain $n = 3 \times 10^4$ detected photons/joule. This strong response would allow even our 100 μW laboratory doubled dye laser to be used as a source monitor. According to the results of this calculation, it would provide 300 counts from 100 ppm of SO_2 in 100 seconds.

SO_2 sources of the type assumed above can also be monitored remotely by simple absorption (e. g. , against skylight) and by differential absorption of Rayleigh/Mie scattering, the so-called DIAL technique (refs. 54, 55). The 1/e absorption length for 300 nm radiation in the assumed plume is about 4 meters. Thus, good contrast is available for these methods.

On the other hand, the 1/e absorption length for a typical ambient air level of 10 ppb SO_2 is about 40 km. In this situation, absorption techniques are much more difficult to apply. However, the fluorescence signal appears to be sufficiently strong to allow range-resolved measurements of SO_2 at these levels at reasonable expense. Consider an experiment where 10 ppb of SO_2 is observed by a LIDAR system with 100 meter resolution at 1 km. We assume that the experimental parameters are as described in the previous example, with the following exceptions: ρ = 10 ppb (STP), R = 1 km, and L = 100 meters. Then from Eq. (88) we find

$$n = 4.5 \text{ counts/joule.}$$

This response is sufficiently strong to be observed in a practical instrument. We have pointed out previously that the decay time of the fluorescence re-emission from SO_2 in air near STP is sufficiently short (<<5 nsec) to allow high resolution time-of-flight ranging. It would be desirable to investigate the fluorescent return from SO_2 at slightly shorter wavelengths (say 270-280 nm) in order to take full advantage of the dark daytime background at wavelengths shorter than 300 nm caused by absorption of sunlight in the atmospheric ozone layer. Also, the influence of water vapor and temperature on the SO_2 quenching needs to be investigated. However, the present results are favorable indications that a LIDAR system observing SO_2 fluorescence can be used to monitor sources and ambient distribution of this gas in the lower atmosphere. Such a probe might be applied, for example, to map the SO_2 distribution far downwind of a source.

Ground-Based Upper Atmosphere Probe

Sodium and potassium layers at altitudes near 80-100 km have already been probed successfully from the ground using dye lasers and fluorescence techniques (refs. 15, 16). In this section we consider the possibility of a ground-based, spatially resolved probe of the O_3 layer at an altitude of 10-35 km. This application is important because the O_3 layer forms the primary shield of solar middle UV from the ground, and because it is an important indicator of chemical chains and physical processes in the stratosphere.

The ozone layer provides many orders of magnitude absorption at wavelengths near 250 nm, falling off gradually toward 300 nm. In order to achieve range resolution we will assume that a transmission wavelength is chosen near 300 nm, such that there is approximately 25% absorption through this layer. The number n of detected photons per joule of transmitted energy will be estimated from a slightly different procedure than used previously. This number can be calculated from the expression

$$n \simeq (0.25)\,\frac{(\xi/4\pi)\,\varepsilon\eta T A}{E_\lambda R^2} \tag{89}$$

where in addition to the parameters defined previously, the factor (0.25) is the assumed absorption, ξ is the efficiency of re-emission into the observed wavelength range following absorption of a photon, and the factor 4π arises from the (approximately) isotropic re-emission into 4π steradians. It is interesting to note that for SO_2 in air at STP, our previous results yield $\xi \simeq 10^{-6}$, determined primarily by quenching. At an altitude of 25 km, where collision frequencies are down by a factor of about 25 from STP (ref. 54), ξ should be on the order of 2.5×10^{-5} for SO_2. In the case of O_3, excitation into the absorption bands near 300 nm is dissociative. Thus the re-emission from O_3 may be similar to that of the resonance scattering from I_2 observed by Holzer et al. (ref. 4) in the visible. A rough estimate of in this case is given by the following product:

$$\xi = \begin{pmatrix}\text{fraction of radiation in} \\ \text{observed spectral lines}\end{pmatrix} \times \left(\frac{\text{mean time to radiate}}{\text{mean time to dissociate}}\right)$$

$$\simeq (10^{-1})\left(\frac{10^{-8}\text{sec}}{10^{-13}\text{sec}}\right) = 10^{-6}$$

Here the mean time to radiate is calculated from the integrated absorption coefficient for the Hartley band, estimated from Fig. 9, using a well known relationship (ref. 12) between these quantities. The mean time to dissociate is set equal to the time required for an oxygen atom with 2 ev of kinetic energy to travel 0.5 nm.

In order to calculate the number of detected photons per joule as given by Eq. (89), we assume the following system parameters:

E_λ	$= 6 \times 10^{-19}$J	T	= 10%
ξ	$= 10^{-6}$	A	= 10 m^2
ε	= 10%	R	= 25 km
η	= 20%		

These assumptions yield

$$\eta = 1.0 \text{ detected photons/joule}$$

which is well within the range of experimental feasibility. The experimental outlook is simplified by the fact that a narrow band, precisely-tuned source should not be needed because the relevant O_3 absorption (Hartley band) is a broad continuum. However, when the sun is near the zenith, substantial daylight background will be encountered. See ref. 56 for an analysis of the effect of this background. We should note that the assumption of 10% two way transmission of 300 nm radiation to 25 km altitude is probably optimistic for sea level operation, but should be achievable from elevated ground (say $\gtrsim$3 km). The requirements for high altitude and large collector area are similar to those for astronomical observatories. Thus the possibility of involving an observatory in LIDAR studies of the upper atmosphere is suggested.

Airborne Measurements

A LIDAR system carried by a high flying airplane can be used to determine the concentrations of many high altitude species. In this case power and collector area limitations can be compensated at least partially by proximity. As one example we consider a probe of ozone at 25 km by a plane flying at an altitude of 15 km. We assume a 1 m^2 collector, T = 50% and other system parameters as in the previous example. Then

$$n = 3.3 \text{ detected photons/joule.}$$

Likewise, an airborne system can be used to probe many other high altitude species. For example, we consider the system described above, but observing a 100 meter column at a range of 300 meters. Suppose that 1 joule is transmitted and that the expected number of detected photons is required to satisfy the condition

$$n \geq 100$$

in order to obtain reasonable statistical accuracy. Then from Eq. 88 we obtain as a condition for a successful measurement

$$\rho\sigma = 6 \times 10^{-14} \text{ cm}^{-1} \text{ sr}^{-1} \qquad (90)$$

In Table III we show estimated effective differential cross sections for fluorescence from a number of molecules and atoms at 20 km altitude, and the corresponding minimum densities which can be measured from Eq. 90. In the case of NO, feasible measurements must await development of doubling techniques or primary laser sources at 227 nm, but a recent publication (ref. 57) suggests that this development is likely to occur in the near future.

TABLE III

Estimated effective differential cross sections for molecular fluorescence (scattering in the case of O_3) in the atmosphere at 20 km altitude, and consequent minimum measurable concentrations (mmc) for the assumed airborne LIDAR system calculated using Eq. 90. The cross section for SO_2 was taken from experimental results obtained in this work. That for NO_2 was calculated from data presented by Fouche, Herzenberg and Chang (ref. 11). The NO cross section is obtained from absorption data of Bethke (ref. 21), assuming a 10^{-6} sec lifetime for radiative decay and quenching at every gas kinetic collision. The OH cross section was calculated similarly using absorption data presented by Penner (ref. 58). The scattering cross section for O_3 (excited by absorption in a dissociative continuum) is calculated by multiplying the absorption cross section from Fig. 9 by the re-emission efficiency estimated in this Chapter. The mmc are expressed as absolute number densities and also as parts per billion (ppb) referenced to a total molecular density of 1.85×10^{18} molecules/cm^3 at 20 km (ref. 59). Estimate re-emission efficiencies ξ are calculated such that $(4\pi/\xi)$ times the fluorescence cross section equals the corresponding absorption cross section. Also shown are corresponding results for the atoms listed in Table IV. The atomic fluorescence cross sections were calculated for the center of Doppler-broadened lines (220°K) using oscillator strengths collected in ref. 60. (The effects of collision broadening and hyperfine structure in the absorption line has been neglected in these calculations.)

Molecule	Estimated Re-emission Efficiency ξ	Effective Cross Section	mmc	mmc in ppb at 20 km
SO_2 (300 nm)	1.6×10^{-5}	2×10^{-24} cm^2/sr	3×10^{10} molecules/cm^3	16
NO_2 (400-500 nm)	10^{-7}	2×10^{-27}	3×10^{13}	16000
O_3(260 nm)	10^{-6}	1×10^{-24}	6×10^{10}	32
NO(227 nm)	3×10^{-3}	3×10^{-22}	2×10^{8}	.11
OH(308 nm)	1.6×10^{-4}	2×10^{-22}	3×10^{8}	.16
Atoms in Table IV	0.001 to 0.1	10^{-18} to 10^{-14} cm^2/sr	6 to 6×10^4 atoms/cm^3 (!)	

In addition to the molecules listed in Table III, there are many other species which can exhibit moderate to strong re-emission at accessible visible and uv wavelengths. Among these are the aromatic hydrocarbons, aldehydes, and various radicals such as CN and C_2.

In addition to its use to estimate minimum measurable concentrations, Eq. (90) can be used to demonstrate that under many conditions the LIDAR technique used with fluorescence will be more sensitive than absorption techniques. First, we note that a relationship between the effective differential fluorescence cross section and the corresponding absorption cross section is given by

$$\sigma \simeq (\xi/4\pi)\, \sigma_{abs} \tag{91}$$

where the re-emission efficiency ξ has been defined following Eq. (89). Thus the condition for a feasible observation (with the experimental parameters assumed above) becomes

$$\rho\sigma_{abs} \geq \frac{4\pi}{\xi} \times 6 \times 10^{-13}\ \mathrm{cm}^{-1} = \frac{7.5 \times 10^{-12}}{\xi}\ \mathrm{cm}^{-1}$$

But the condition for a feasible observation in an absorption measurement (for example, using the DIAL technique) is

$$\rho\sigma_{abs}\, H \gtrsim 10^{-2}$$

where H is the thickness of the observed layer. Thus the assumed LIDAR system will be more sensitive than a system using absorption measurements if

$$\frac{H}{\xi} < 1.33 \times 10^{6}\ \mathrm{km} \tag{92}$$

Note that if the DIAL technique is used to obtain range resolution in an absorption measurement, H corresponds to the range resolution. The results indicated in Table III suggest that at 20 km altitude Condition (92) is likely to be satisfied for NO, OH and atoms, but not necessarily for NO_2, SO_2 and O_3.

Measurement of Upper Atmosphere Constituents from a Satellite

Satellite LIDAR measurements are more difficult because of power and collector area limitations, as well as the large working distances required. On the other hand, transmission is high and many effective fluorescence cross sections are much larger than in the lower atmosphere because of reduced quenching. (The collision frequency is lower by a factor of 4×10^6 at 100 km altitude than at sea level - ref. 59.) The general net effect is that measurements are more difficult from a satellite. However, we will show that there are LIDAR type measurements which appear quite feasible.

In order to develop quantitative estimates, we assume as in the previous section that a 1 joule pulse is transmitted, that returned light is collected over a 1 m^2 area, and that the LIDAR system observes a 1 km column at a range R. Other experimental parameters are taken to be those assumed in the previous example. Then, as a condition for a successful measurement, we obtain from Eq. (80)

$$\rho\sigma \geq \left(6 \times 10^{-10}\text{cm}^{-1}\text{sr}^{-1}\right)\left(\frac{R}{100\text{ km}}\right)^2 \qquad (93)$$

When the number densities of various species at high altitudes are taken into account, Eq. (93) implies that a successful measurement requires a large cross section. However there are many atoms with fluorescence cross sections on the order of 10^{-13} to 10^{-16} cm^2/sr, for which very small concentrations can be measured. A representative group of these atoms is shown in Table IV. In Fig. 34 we show resulting estimated minimum measurable concentrations as a function of altitude, calculated from Eq. (93) assuming a satellite altitude of 250 km. The total density as a function of altitude is shown on the figure for comparison.

Also shown are the estimated minimum measurable concentrations for several molecules. It is immediately apparent that the situation for molecules is much less favorable than for the atoms discussed previously. This result obtains because of the multiplicity of available states introduced by the additional degrees of freedom of a molecule. This multiplicity reduces the re-emission cross section in three ways: first, because only a fraction of the molecules will be in initial states leading to the observed transition; second, because the strength of the transition is divided among all accessible excited states; and third, because the re-emission is distributed among all allowed downward transitions. Thus fluorescence cross sections for molecules are smaller. Estimated values used in preparing Fig. 34 are shown in Table V.

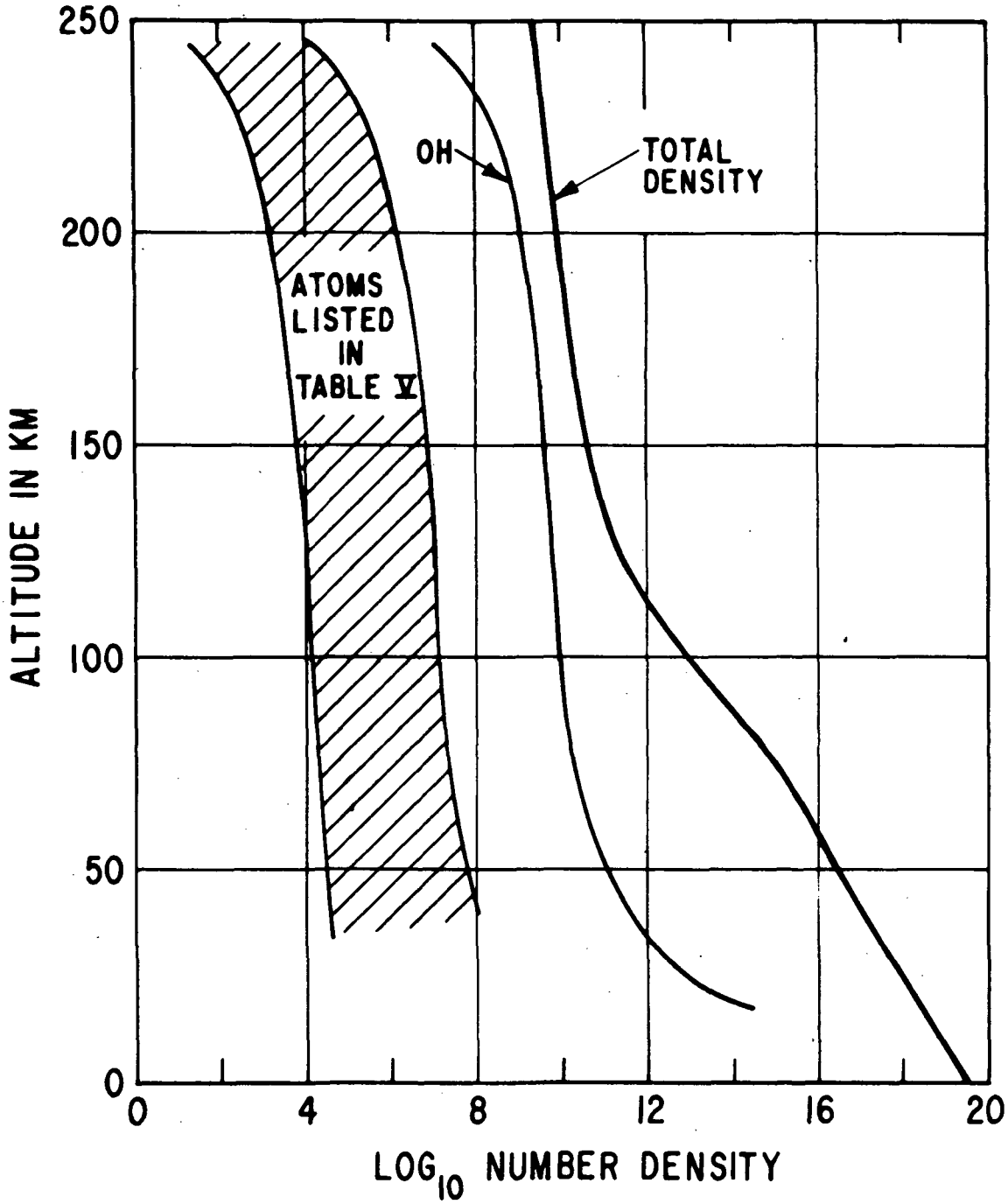

Figure 34 Minimum measurable concentrations of atoms and OH radical under conditions assumed for satellite probe. The total molecule density as a function of altitude, from ref. 59, is also shown for comparison.

TABLE IV

Atoms for which strong fluorescence under excitation on resonance lines between 250 and 900 nm has been demonstrated or is predicted on the basis of available transitions with large oscillator strengths. Unquenched fluorescence cross sections for these atoms calculated for the center of a Doppler-broadened line (200°K) are on the order of 10^{-13} to 10^{-16} cm^2/sr (hyperfine structure effects neglected). Corresponding excited state lifetimes are on the order of 10^{-9} to 10^{-6} seconds. Excitation wavelengths for these atoms, and corresponding oscillator strengths are collected in ref. 60. Atoms indicated by an asterisk (*) produce strong fluorescence at wavelengths shifted from that of the incident light, allowing discrimination against Rayleigh and Mie scattering.

Atom	Approximate Excitation Wavelength	Atom	Approximate Excitation Wavelength
Li	671 nm	Mn	403 nm
Na	589	Re	346
K	770	*Fe	300
Rb	795	*Ru	299
Cs	894	*Os	353
*Cu	327	*Co	341
Ag	328	*Rh	343
Au	268	*Ir	250
Mg	285	*Ni	337
Ca	423	*Pi	276
Sr	461	*Pt	266
Ba	554	*Al	394
Cd	326	*Ga	403
Hg	254	*In	410
*Rare Earths	400-900	*Tl	378
*Sc	391	*Sn	286
*Y	408	*Pb	283
Cr	427	*Bi	307
M0	390	*C	286

TABLE V

Estimated effective differential cross sections for molecular fluorescence (scattering in the case of O_3) in the atmosphere at 100 km altitude. These cross sections were calculated from measured absorption coefficients (refs. 19, 20, 21, 24, 59), using the equation $\sigma_{fl} = \sigma_{abs}(\xi/4\pi)$. Re-emission efficiencies ξ were estimated assuming no quenching since the collision frequency at 100 km is small (2×10^3 sec^{-1}). For SO_2 and NO_2, ξ takes into account the effects of the anomalously long fluorescence decay times (ref. 39) which are presumed to be related to non-radiative decay. The value of ξ for O_3 is diminished by dissociation; we use the value estimated earlier in this report.

Molecule	Estimated Re-emission Efficiency ξ	Cross Section
SO_2	1×10^{-3}	1×10^{-22} cm^2/sr
NO_2	5×10^{-3}	1×10^{-22}
O_3	10^{-6}	1×10^{-24}
NO	10^{-1}	1×10^{-20}
OH	10^{-1}	1.3×10^{-19}

Equation (93) can be used to estimate in what cases a LIDAR measurement will be more sensitive than an absorption measurement, as was done previously for the airborne system. In the present case, we find that the assumed LIDAR system should be more sensitive when

$$\frac{H}{\xi} \leq 1.33 \times 10^3 \text{ km} \left(\frac{100 \text{ km}}{R}\right)^2 \qquad (94)$$

where R is the observation range. This condition will be satisfied, for example, if H = 20 km and R = 150 km for $\xi \geq .034$. All atomic species and a few of the molecules considered will satisfy this condition at altitudes $\gtrsim$100 km.

V. CONCLUSIONS

Major tasks supported by this contract are:

1. A classical theoretical study of the amplitude and time dependence of re-emission from an isolated molecule following pulse light excitation, as a function of separation from resonance. (Chap. II). This study includes formulation of the problem, analysis of limiting cases and numerical solutions for intermediate cases in the transition from scattering to fluorescence.

2. A quantum-mechanical study of the problem described above. (Chap. II and Appendix C). The resulting expressions for the time dependence of the re-emission were shown to agree with the classical results in significant limiting cases. This agreement was taken as an indication that the classical results are essentially correct.

3. Theoretical analysis of the depolarization of scattering following excitation into a dissociative continuum, in which a quantum interference effect that tends to reduce depolarization was discovered (Chap. II and Appendix D).

4. Qualitative estimates suggesting the possibility of very strong scattering from O_3 excited in its Hartley band, which is a dissociative continuum (Chap. IV).

5. Measurement of the absolute NO_2 cross section for line fluorescence excited in air near STP by visible light (488 nm) (Chap. III).

6. Measurement of the O_3 vibrational Raman cross section for visible light (488.0 and 514.5 nm) excitation (Chap. III).

7. Assembly of a doubled dye laser spectroscopy system from components on hand (Chap. III).

8. Measurement of absolute N_2 and O_2 vibrational Raman cross sections for excitation at 300 nm, using the doubled dye laser system (Chap. III).

9. Detailed quantitative study of SO_2 ν_1-line fluorescence and quenching of this fluorescence by air (Chap. III).

From the consequent results and others described in this report, we have drawn the following conclusions:

Near Resonance Scattering

Analysis of the time dependence of re-emission from an isolated molecule excited by a light pulse shows a clear transition from delayed re-emission

(fluorescence) to "instantaneous" re-emission (scattering) as the separation from resonance is increased beyond substantial overlap between spectral distributions of the absorption line and incident light. This result was used to conclude tentatively that in a real gas the re-emission would be both instantaneous and insensitive to such effects of molecular interactions as quenching, collisional depolarization, and collisional relaxation when the separation from resonance is several times larger than:

A. The collision linewidth, and

B. The range of significant inhomogeneous broadening (statistical average of line shifts produced by Doppler effect and molecular interactions).

However, we cannot regard this conclusion as firmly established at the present time. Early results from an alternative quantum electrodynamic analysis suggest that the re-emission intensity in primary lines (i. e., lines from the originally excited intermediate state) will be independent of pressure under the conditions specified above, but that collisional depolarization and relative intensity of collision lines (satellite lines produced by energy exchanged during collisions) may remain equal to their values in fluorescence out to much greater separation from resonance. Our inability to draw firm general conclusions about the character of re-emission as a function of separation from resonance in a real gas is related to the location of the phenomena of interest in the far wings of an absorption line, where presently developed theories falter. Tuned laser fluorescence studies are expected to produce both incentive and information for further developments in this area. As a case in point, in work supported by GE we investigated collision-to-primary line intensity ratios as a function of separation from resonance in low pressure (200 mTorr) I_2 vapor. The incident light was from argon and krypton lasers that were single-moded and tuned over various gain curves using a tilted etalon. Over substantial tuning ranges (several times the Doppler full width at half maximum in one case) this ratio could be observed precisely and was found to remain essentially constant. This result supports the suggestions of the alternative quantum electrodynamic theory. However, it can also be explained on the basis of the original conclusion as arising from effects of inhomogeneous broadening produced by line shifts.

Scattering Following Excitation in Dissociative Continuum

In addition to near-resonance enhancement, we considered also the type of scattering that results from excitation in a dissociative continuum. Holzer et al. showed that this type of scattering from I_2 excited by blue light (488 nm) is substantially stronger than nitrogen Raman scattering. Our rough calculation in Chap. IV for the intensity of Raman scattering from O_3, excited in is dissociative Hartley band between 220 nm and 310 nm, indicates that in this case the scattering should be very strong, with a cross section on the

order of 10^{-24} cm^2/sr, or about five orders of magnitude stronger than the nitrogen Raman scattering.

Fluorescence

At the outset of this work it was presumed that the advantages of scattering over fluorescence as a gas probe would be important in atmospheric measurements. Accordingly, the enhancement of scattering in the approach to resonance and the ultimate shift from scattering-like to fluorescence-like re-emission in this approach received strong initial attention. However, during this work it became increasingly apparent that the greater strength of fluorescence is crucial to many measurements of low concentrations in the atmosphere from substantial distances, and furthermore, the potentially detrimental characteristics of fluorescence as a gas probe (e.g., quenching, time delay at low pressure) are often not serious impediments to these measurements. Specifically, fluorescence measurements with a LIDAR system should be useful under the following conditions:

1. The species whose measurement is sought exists at low concentration in a carrier gas that dominates line broadening and quenching.

2. The pressure of the carrier gas is known with sufficient accuracy to make line broadening and quenching corrections, and it is high enough to shorten the re-emission delay of observed fluorescence to the point where time-of-flight ranging can be used.

3. The quenched fluorescence of the target species is much stronger than ordinary RS and has a characteristic spectral distribution that allows its identification.

With respect to the time dependence, we and others have observed that fluorescence decay times are sharply reduced by quenching to times on the order of a few nanoseconds in air near STP. Even at the low pressures and collision frequencies encountered at high altitudes, the consequent near "natural" decay times of fluorescence for many molecules are not so long as to preclude useful range resolution. For example, an exponential decay time of 1 microsecond allows a resolution element of about 150 meters. With respect to the strength of fluorescence it has been found that even under rapid quenching in air near STP, characteristic fluorescence can be many orders of magnitude stronger than ordinary Raman scattering. For quantitative measurements in a system such as the lower atmosphere, dominant quenching rates must be determined accurately. In many cases, where the absorption and/or fluorescence cross sections have spectral structure on a fine scale, the spectral distribution of the exciting light must be controlled precisely. Furthermore, the sensitivity of these cross sections to temperature and minor species such as H_2O and CO_2 must be investigated. Nevertheless, quantitative experimental results such as those we have obtained

for SO_2 (see below) suggest that fluorescence measurements of minor species in the lower atmosphere may be quite worthwhile.

Experimental Results

In the experimental part of our work, re-emission from NO_2, I_2 and O_3 was observed in the visible, using an argon laser source, and re-emission from N_2, O_2 and SO_2 was observed in the ultraviolet near 300 nm. We found that the characteristic ν_1 line fluorescence from NO_2 in air near STP is slightly more than 100 times enhanced over the vibrational Raman scattering from N_2, in reasonable agreement with results calculated from data published by Fouche, Herzenberg, and Chang (ref. 11). This enhancement is probably not sufficient to allow practical measurements of ambient levels of NO_2 in the atmosphere, but there is a possibility that much stronger enhancement will be found under excitation at particular wavelengths in the blue, where Sackett and Yardley (refs. 35, 36, 37) have observed fluorescence components with anomalously fast decay.

Perhaps our most useful observation with respect to atmospheric probes is the very strong fluorescence from SO_2 in air near STP excited by light near 300 nm. The intensity of this fluorescence was measured to be 10^4 times stronger per molecule than vibrational Raman scattering from N_2, which itself was found to be several times larger than a $(1/\lambda_{scatter})^4$ extrapolation from measurements in the visible.

Model Calculations

Effective cross sections for fluorescence from OH, NO and a large group of atoms were estimated from available data in Chapter IV. These cross sections correspond to excitation in the range from 250-900 nm, except for NO which must be excited near 227 nm. The estimated molecule cross sections, though smaller than those for atoms by, typically, 6-8 orders of magnitude, are still sufficiently large to allow useful measurements.

Measured cross sections for ν_1-line fluorescence from SO_2, excited near 300 nm, and estimated resonance Raman scattering cross sections for O_3 excited between 250 and 300 nm were used as a basis for model calculations. These calculations indicate that the cross sections are sufficiently large to allow range-resolved LIDAR measurements of source levels of SO_2 and even ambient levels (on the order of 10 ppb) of SO_2 and O_3 in the lower atmosphere. Further, it appears likely that the O_3 cross section is sufficiently large to allow range-resolved LIDAR measurements of the stratospheric O_3 layer between 10 and 30 km altitude from a high altitude ground-based station or an airborne station.

The large fluorescence cross sections predicted for numerous atomic species at accessible excitation wavelengths allow concentrations of a few atoms/centimeter^3 to be measured at close range (300 meters) by an airborne LIDAR probe. Some molecule concentrations (e. g., SO_2 and O_3) may be measurable also. The large atom cross sections establish a good possibility that many atom concentrations in the upper atmosphere can be measured from a satellite LIDAR probe. However, the possibility for satellite LIDAR measurements of existing levels of molecules and radicals such as OH appears to be marginal at best.

APPENDIX A

Distinction Between Fluorescence and Resonance Raman Scattering

Various criteria have been used to distinguish between Raman scattering and fluorescence excited near or on resonance. The original distinction is that the frequency shift in Raman scattering is independent of incident wavelength (frequency), whereas in fluorescence the frequency itself, rather than the shift, is constant. Thus as incident light frequency is shifted, the Raman scattering frequency will shift comensurately, while fluorescence appears only at wavelengths characteristic of molecular transitions. However, this distinction is difficult to apply in the case of excitation into a true or apparent continuum (e.g., NO_2 or SO_2 absorption) where fluorescence would also be expected to shift with incident wavelength. It is also difficult to apply, although presumably operative, in cases which involve excitation very near resonance, because of problems associated with high resolution spectroscopy at low light levels.

Hibben (ref. 61) expresses a common distinction that scattering is instantaneous whereas fluorescence shows an exponential decay. However, strongly quenched fluorescence in high pressure gases, and fluorescence from many solids (e.g. dyes) is also very fast (10^{-10} to 10^{-12} sec.) such that its decay time is difficult to sense. It is possible to avoid this ambiguity by defining scattering as an intrinsically instantaneous process; i.e., a process which is effectively instantaneous in an isolated molecule. Yet this definition is obviously inapplicable to fluorescence from solids and liquids, and not even be generally meaningful for gases because of the expected sensitivity of re-emission on the borderline to the line broadening produced by molecular interactions.

The relevant work of Behringer and associates, extending from the present back to at least 1956, pertains mostly to "pre-resonance" and resonance excitation in solids and liquids. In a fairly recent review (ref. 25), Behringer appears to identify resonance scattering as that component of the re-emission excited near resonance with spectral characteristics similar to "ordinary" scattering excited well off resonance. On the other hand, features such as an underlying continuum which appears in the approach to resonance are identified as fluorescence. Behringer notes that the relationship between these phenomena is incompletely understood.

In 1970, Holzer, Murphy and Bernstein (ref. 4) published an important paper in which they identified a new type of resonance scattering, which results from excitation in a dissociative continuum. In this paper they specified a consistent set of distinctions between Raman scattering and fluorescence. In particular they noted that resonance Raman scattering is

usually strongly polarized and always insenstive to quenching, in distinction to fluorescence. Subsequently, Berjot, Jacon and Bernard (ref. 9) identified as fluorescence those processes which proceed predominantly through a single intermediate level, whereas scattering results when transitions through at least several intermediate levels are significant. This identification has the advantage of associating distinctive selection rules with the fluorescence, with the result that fluorescence and scattering can usually be distinguished by the spectral character of the re-emission.

Our own distinction is strictly utilitarian. We define scattering to be re-emission which is effectively instantaneous and insensitive to effects of molecular interactions such as quenching, collisional depolarization and the gross spectral broadening produced by collisional transfer. However, neither we nor others to our knowledge have yet demonstrated unequivocably whether or not re-emission excited off resonance, but predominantly through a single level, satisfies these criteria.

APPENDIX B

Quantum Mechanical Interferences

The quantum mechanical expression for the scattering cross section is given by

$$(\sigma_{12}) = \frac{1}{c^4 \hbar^2} \sum_n F_n \sum_p \omega_2^4 \, \delta(\omega_{nf} + \omega_{12})$$

$$(x) \left| \sum_r \frac{(D_2)_{fr} (D_1)_{rn}}{\omega_{rn} - \omega_1 + i\gamma_r/2} + \frac{(D_1)_{fr} (D_2)_{rn}}{\omega_{rf} + \omega_1 - i\gamma_r/2} \right|^2$$

which is identical to Eq. (38) except that the average over the fractional population of initial states F_n and sum over final states is indicated explicitly and the δ-function ensures energy conservation. Within the absolute square, the sum over intermediate states $\{r\}$ may include terms of opposite sign (or in the general case, complex terms with different phases) such that they tend to cancel. Since the relative magnitude of these terms depends on the incident frequency, interference effects can produce oscillations in the cross section as incident frequency varies. (Notice that contributions starting from different initial states and/or ending on different final states do not interfere, because the absolute square is performed for each term in the sum over initial and final states.) The most obvious situation where interference occurs is when incident frequency increases through a resonance, changing the sign of one of the terms. Interference effects of this type have been predicted in ref. 18. They are responsible for the dimunition of depolarization in scattering excited within a dissociative continuum which we have predicted and observed, and they also produce the observable effect in level crossing spectroscopy, where levels are shifted by an applied field.

From another standpoint, the possibility of this type of interference makes accurate estimates of scattering enhancement from oscillator strengths uncertain in cases where more than one intermediate level is likely to contribute significantly. A case in point is our estimate of the NO cross section at 250 nm, where we simply summed contributions from various vibrational bands algebraically, ignoring possible interference.

This procedure appears to be a good approximation when the separation from resonance is large compared with the separation between intermediate levels which contribute significantly to the scattering. To demonstrate this point, we consider the case where the relevant levels are associated with different rotational angular momentum, but the same vibrational and electronic states. Employing the Born-Oppenheimer approximation, we separate the rotational eigenfunctions R and the electronic-vibrational eiginfunctions τ to obtain for one of the terms in the absolute square

$$\sum_{V''R''} \frac{(D_2)_{\tau'R',\,\tau''R''}\,(D_2)_{\tau''R'',\,\tau R}}{\omega_{\tau''\tau} + \omega_{R''R} - \omega_1 + i\gamma_\tau/2}$$

Here unprimed, single-primed and double-primed letters designate initial, final and intermediate states, respectively. Now if the separation from resonance is sufficiently large, $\omega_{R''R}$ may be neglected and the sum over R" performed through closure (ref. 28). Then, if the absolute square is completed and the sum over all final states (including scattered radiation states) is performed, one obtains simply the absorption cross section. Working backward, the relative magnitudes for various components in the sum yield the branching ratios for various types of scattering. This argument may be extended to contributions through different vibrational and electronic states when the separation from resonance is sufficient. Unfortunately, in many cases, such as our estimate of the NO scattering excited at 250 nm, it is not. In such cases, our estimation procedure yields an "expectation value" but with a large uncertainty. A better estimate appears to require a much more detailed calculation.

APPENDIX C*

Quantum Calculation of Time Dependence of Re-emission

We desire a simple quantum mechanical model and formulation, which describe the time dependence of the scattering of a coherent pulse of light that is emitted from a laser pump source at a well-defined time and scatters from a quantum scatterer located at the origin. Our treatment is essentially that of a fixed single scatterer at the origin which would seem to preclude ab initio many-particle effects which give rise to inhomogeneous broadening of spectral lines both from molecular collisions and thermal motion of the scatterers, and collisional-nonradiative de-excitation (quenching) of excited states. The inhomogeneous broadening can be taken into account by suitably averaging over initial states of the scatterer, while the quenching can be taken into account, at least heuristically, by a suitable collisional renormalization of the intermediate state propagators.

For the internal states of the scatterer, we will consider the simplified model of a three-level quantum system with energy levels 0, 1, 2. We will assume that there are allowed dipole transitions between $0 \rightleftarrows 1$, $1 \rightleftarrows 2$. The states 0 and 2 can be chosen as the ground state and low-lying excited state, which could be contained within the ground state manifold, e. g. , a vibrational state. The pulse of light which is introduced into our system will have a central frequency ω_L and a frequency breadth Δ; the time breadth of the coherent pulse $\sim 1/\Delta$. We can view this problem in the following qualitative way. If the packet is far removed from the origin, there is no interaction between it and the scatterer; the interaction commences when the leading edge of the wave packet overlaps the scatterer. We can crudely break the scattered light emission up into two time regions: first, the emission rate when the wave packet spatially overlaps the scatterer; and, second, a fluorescence which occurs at a time after the packet has passed the origin. Usually one calculates fluorescent emission by initiating the system in an unstable state at time $t = 0$ and then allowing the system to radiatively decay. Here our initial condition is a wave packet of light and a scatterer in the ground state. For near-resonance cases, the wave packet will have Fourier components which mix the ground state with an excited state, and hence there will be a certain probability that the scatterer will be left in the excited state after the pulse has passed. This condition will then serve as the initiation of the unstable state from which the system can subsequently fluoresce. The relative and absolute strengths of the "scattering" and "fluorescence" so defined will depend upon the parameters of the wave packet and in particular on the nearness to resonance of the central pulse frequency ω_L.

*This appendix is taken from GE Report 73CRD196, authored by Seth D. Silverstein. The work was supported by Contract NAS1-11624 from NASA Langley Research Center.

Before we go into the specific quantum mechanical representation of the pulse and the details of the calculation, we will first outline the general formulation of the scattering problem with propagating wave packets (ref. 62).

Let us consider first the state at time $t = -t_0$ where the center of the wave packet is sufficiently removed from the origin that there is no overlap and hence no interaction. If we denote K as the sum of the free scatter and electromagnetic Hamiltonians, the wave function at time $t = -t_0$ is given by

$$e^{iKt_o} |\Psi_{ic}\rangle |\Phi_o\rangle \quad . \tag{C1}$$

Here $|\Psi_{ic}\rangle$ represents the wave function for the light pulse, and $|\Phi_o\rangle$ the ground state of the scatterer. We note that in standard time-dependent perturbation theory the initial states are usually taken as eigenstates of K and hence are stationary states in the absence of interaction. This is not appropriate for the case considered here because we desire that the pulse propagates in space and hence is nonstationary. Let us now turn on the interaction, so that the wave function at time +t is given by

$$e^{-i\mathcal{H}(t+t_o)} e^{iKt_o} |\Psi_{ic}\rangle |\Phi_o\rangle \quad , \tag{C2}$$

where

$$\mathcal{H} = K + V \quad .$$

We desire to obtain the probability amplitude for the system being in a noninteracting final state at a time t,

$$|\Psi_f(t)\rangle = e^{-iKt} |\Psi'\rangle |\Phi'\rangle \quad . \tag{C3}$$

This is given by

$$\langle\Psi'| \langle\Phi'| e^{iKt} e^{-i\mathcal{H}(t+t_o)} e^{iKt_o} |\Psi_{ic}\rangle |\Phi_o\rangle \quad . \tag{C4}$$

If we define

$$U(t+t_o) = e^{iKt} e^{-i\mathcal{H}(t+t_o)} e^{iKt_o} \quad , \tag{C5}$$

U possesses the standard perturbation expansion,

$$U(t+t_o) = 1 - i/\hbar \int_{-t_o}^{t} dt_1 V(t_1) + i^2/\hbar^2 \int_{-t_o}^{t} dt_1 \int_{-t_o}^{t_1} dt_2 \, V(t_1) V(t_2) + \cdots \quad . \tag{C6}$$

We are interested in a scattered photon; hence the terms of interest will be derived primarily from the second-order terms in the expansion of U. If the time of transit from the laser source to the scatter at the origin is long compared to the time width of the pulse, we can always set the initial time $-t_o \to -\infty$, with the condition that the wave packet is centered at the origin at $t = 0$.

We now want to consider the quantum mechanical representation of the initial pulse state $|\Psi_{ic}\rangle$. We choose $|\Psi_{ic}\rangle$ in a form such that the expectation value of the electric field operator describes a pulse propagating in the +z direction;

$$\langle \Psi_{ic} | \hat{\underset{\sim}{E}}(\underset{\sim}{r}, t) | \Psi_{ic} \rangle = \underset{\sim}{\varepsilon}_x \mathrm{Re} \int_0^\infty d\omega \, E(\omega - \omega_L) e^{-i\omega t} \quad . \tag{C7}$$

Here $\underset{\sim}{\varepsilon}_x$ is a unit polarization vector in the x direction. The electric field operator is given in terms of photon creation and annihilation operators by

$$\hat{\underset{\sim}{E}}(\underset{\sim}{r}, t) = -i \sum_{\underset{\sim}{k}, \lambda} \left(\frac{2\pi\hbar\omega_k}{V} \right)^{1/2} \underset{\sim}{\varepsilon}_{\underset{\sim}{k}\lambda} \left\{ a^+_{\underset{\sim}{k}, \lambda} e^{-i(\underset{\sim}{k} \cdot \underset{\sim}{r} - \omega_k t)} - a_{\underset{\sim}{k}, \lambda} e^{i(\underset{\sim}{k} \cdot \underset{\sim}{r} - \omega_k t)} \right\} \tag{C8}$$

We can achieve a semi-classical representation of the form (C7) by requiring that $|\Psi_{ic}\rangle$ be eigenstates of the destruction operators,

$$a_{\underset{\sim}{k}, \lambda} |\Psi_{ic}\rangle = \begin{cases} \alpha_{k, \lambda} |\Psi_{ic}\rangle & \text{for } \underset{\sim}{k}, \lambda \; \varepsilon (k_z > 0, \; k_\perp = 0, \; \lambda = \lambda_x) \\ 0 \qquad \text{otherwise.} \end{cases} \quad . \tag{C9}$$

The "coherent state" representation of the packet wave function (ref. 63) satisfies this condition:

$$|\Psi_{ic}\rangle = \exp\left[\sum_{>0} (a_{k_z} a^+_{k_z \lambda x} - |\alpha_{k_z}|^2/2) \right] |0\rangle \quad . \tag{C10}$$

Here $|0\rangle$ is the photon vacuum state and the wave function $|\Psi_{ic}\rangle$ is normalized. We can readily verify that (C9) satisfies (C10) by expanding the exponential operator in a power series and then operating on the result with $a_{\underset{\sim}{k}, \lambda}$, e.g.,

$$a_{\underset{\sim}{k},\lambda} \sum_{m=0}^{\infty} \frac{(a^{+}_{k_z,\lambda x})^m}{m!} |0\rangle = \delta_{\underset{\sim}{k},k_z} \delta_{\lambda,\lambda x} \alpha_{k_z} \sum_{m=1}^{\infty} \frac{(a_{k_z \lambda x} \alpha_{k_z})^{m-1}}{(m-1)!} |0\rangle \quad \text{(C11)}$$

$$= \alpha_{k_z} \delta_{\underset{\sim}{k},k_z} \delta_{\lambda,\lambda x} \exp\left[a^{+}_{k_z \lambda x} \alpha_{k_z}\right] |0\rangle \ .$$

We previously commented that the quantum state representing the propagating wave packet is nonstationary and hence not an eigenstate of the free electromagnetic field Hamiltonian. This is apparent from the form of (C7) exponential form of the operators exhibits an undetermined photon number. As is well known, photon number and phase are canonical operators, and it is this uncertainty in photon number which gives the desired aspect of the coherent propagation of the pulse. We note that our model of a single scatterer in vacuum rules out dispersive distortion of the pulse and such effects will be neglected.

We now want to specify the normalization for the wave packet function. We use a similar procedure as given in the preceding classical calculation, appropriately modified for the quantum case,

$$\frac{c}{4\pi} \int_{-\infty}^{+\infty} dt \left| \langle \Psi_{ic} | \hat{\underset{\sim}{E}}(r=0,t) \times \hat{\underset{\sim}{\mathcal{K}}}(r=0,t) | \Psi_{ic} \rangle \right| \Psi = N\hbar\omega_L + \text{const.} \ . \quad \text{(C12)}$$

That is, we want to describe the pulse in terms of an effective photon number N. The constant term is the vacuum contribution and does not depend upon the pulse. Upon insertion of the appropriate forms for the electric and magnetic field operators, we obtain

$$\frac{\hbar^2 L^2}{2\pi c V} \int_0^{\infty} d\omega \, \omega \left| \alpha(\omega) + \alpha(-\omega) \right|^2 = N\hbar\omega_L \ . \quad \text{(C13)}$$

Taking a Lorentzian form of $\alpha(\omega)$,

$$\alpha(\omega) = \Lambda_\ell \sqrt{\frac{\omega_L}{\omega}} \frac{1}{(\omega - \omega_L)^2 + \Delta^2/4} \quad \text{(C14)}$$

our normalization condition [Eqs. (41), (42)] gives

$$\Lambda_\ell^2 = \frac{2N\Delta^3 cV}{L^2} \left(1 + 0(\Delta/\omega_L)\right) \quad \text{(C15)}$$

We note that we have added a factor of $(\omega_L/\omega)^{1/2}$ to a standard Lorentzian in Eq. (C11). This is done for convenience only and can be replaced by unity to terms of order Δ/ω_L. We note that our analysis will neglect terms of order Δ/ω_L relative to unity as they will be very small for optical frequencies of interest.

For a Gaussian wave packet we take

$$\alpha(\omega) = \Lambda_g \sqrt{\frac{\omega_L}{\omega}} \exp[-(\omega - \omega_L)^2/2\Delta^2] \quad . \tag{C16}$$

to terms of order $\exp[-\omega_L^2/\Delta^2]$ relative to unity, we have

$$\Lambda_g^2 = \frac{2\sqrt{\pi}\, cVN}{L^2 \Delta} \quad . \tag{C17}$$

In our calculation of the time dependence of the scattering in the approach to resonance, we will work with the Lorentzian function only as it is mathematically simpler. For the Gaussian one would proceed in the same way; except that the mathematics dealing with integrals involving the convolution of error functions with harmonic functions and Lorentzians proves tedious. We can, however, infer the quantum results for the Gaussian by the connection between the classical and quantum results derived for the Lorentzian pulse.

We now give the representation of the final state. We choose as our final state of the electromagnetic field one which represents an additional photon which is not contained in the phase space spanned by $|\Psi_{ic}\rangle$. We designate the wave vector of this photon by $\underset{\sim}{k}_f$; hence $|\Psi_f\rangle$ can be taken as

$$|\Psi_{\underset{\sim}{k}_f, \lambda_f; m}\rangle = a^+_{\underset{\sim}{k}_f, \lambda_f} |\Psi_{ic}\rangle |\Phi_m\rangle \; ; \; \underset{\sim}{k}_f \neq (k_f > 0,\ k_\perp = 0) \tag{C18}$$

Here $|\Phi_m\rangle$ represents the final internal state of the scatterer which would correspond to m = 0 for Rayleigh processes, and m = 2 for Raman processes.

B. Calculations of the Scattering Intensity

In our calculation we are interested in the one photon emissions; accordingly we restrict our consideration to second-order terms in the interaction which are treated in the dipole approximation. As such, we use the $\underset{\sim}{E} \cdot \underset{\sim}{d}$ form of the electromagnetic interaction.

$$V(t) = -\underset{\sim}{E}(t) \cdot \underset{\sim}{d}(t) \tag{C19}$$

The second-order terms to be considered, Eq. (C6) are of the form

$$-1/\hbar^2 \int_{-\infty}^{t} dt_2 \int_{-\infty}^{t_1} dt_1 \ \langle f \,|V(t_2)V(t_1)|\, i\rangle \tag{C20}$$

Inserting the forms for the initial and final states as previously discussed, we have

$$\langle f \,|V(t_2)V(t_1)|\, i\rangle = -\sum_{\substack{\underset{\sim}{k}_1, \lambda_1 \\ \underset{\sim}{k}_2, \lambda_2}} \frac{2\pi\hbar}{V} \left|\omega_{k_1}\omega_{k_2}\right|^{1/2} \left|d_{\lambda_2}\right| m1 \left|d_{\lambda_1}\right|_{10}$$

$$\times \exp i[\omega_{m1} t_2 - \omega_{01} t_1 + i\Gamma_1/2(t_2 - t_1)] \tag{C21}$$

$$\times \langle \Psi_{ic} | a_{\underset{\sim}{k}_f, \lambda_f} \left[a^{+}_{\underset{\sim}{k}_2, \lambda_2} e^{i\omega_{k_2} t_2} - a_{k_2, \lambda_2} e^{-i\omega_2 t_2} \right]$$

$$\times \left[a^{+}_{k_1, \lambda_1} e^{i\omega_{k_1} t_1} - a_{k_1, \lambda_1} e^{-i\omega_{k_1} t_1} \right] | \Psi_{ic} \rangle$$

where $\omega_{mn} = (\epsilon_m - \epsilon_n)\hbar$.

We note that we have heuristically incorporated a lifetime Γ_1^{-1} for the intermediate state. Here Γ_1 is interpreted as the sum of quenching and spontaneous decay rates. From (C21) we obtain the sum of two terms

$$\frac{-2\pi\hbar}{V} \sum_{\substack{\underset{\sim}{k}_1, \lambda_1 \\ \underset{\sim}{k}_2, \lambda_2}} \left|\omega_{k_1}\omega_{k_2}\right|^{1/2} (d_x)_{m1} \left|d_{\lambda_f}\right|_{10} \delta_{\underset{\sim}{k}_1, k_f} \delta_{\lambda_1, \lambda_f} \delta_{k_{2\perp}, o} \delta_{\lambda_2, \lambda_x}$$

$$\times \left\{ \alpha^{*}_{k_2} \exp i \left[t_2 \left|\omega_{m_1} + \omega_{k_2}\right| - t_1 \left|\omega_{01} - \omega_{k_f}\right| + \frac{i\Gamma_1}{2}(t_2 - t_1) \right] \right. \tag{C22}$$

$$\left. + \alpha_{k_2} \exp i \left[t_2 \left|\omega_{m1} - \omega_{k_2}\right| - t_1 \left|\omega_{01} - \omega_{k_f}\right| + \frac{i\Gamma_1}{2}(t_2 - t_1) \right] \right\};$$

$$\frac{-2\pi\hbar}{V}\sum_{\substack{\underset{\sim}{k}_1,\lambda_1\\ \underset{\sim}{k}_2,\lambda_2}} \left(\omega_{k_1}\omega_{k_2}\right)^{1/2}\left(d_{\lambda_f}\right) m_1 (d_x)_{10}\,\delta_{\underset{\sim}{k}_2,\underset{\sim}{k}_f}\,\delta_{\lambda_2,\lambda_f}\,\delta_{k_{1\perp},0}\,\delta_{\lambda_1,\lambda_x}$$

$$\times\left\{\alpha^*_{k_1}\exp i\left[t_2\left(\omega_{m_1}+\omega_{k_f}\right)-t_1\left(\omega_{01}-\omega_{k_1}\right)+\frac{i\Gamma_1}{2}(t_2-t_1)\right]\right. \tag{C23}$$

$$\left.+\alpha_{k_1}\exp i\left[t_2\left(\omega_{m_1}+\omega_{k_f}\right)-t_1\left(\omega_{01}+\omega_{k_1}\right)+\frac{i\Gamma_1}{2}(t_2-t_1)\right]\right\}$$

We are interested in near resonance phenomenon, $\omega_L \to \omega_{10}$. Hence the dominant contributions from the above terms will be the ones which exhibit a near stationary phase over the full time domains. This corresponds to the last term in Eq. (C23).

Performing the double-time integral in Eq. (C20), we have

$$\frac{2\pi}{V\hbar}\left(\omega_L\omega_{k_f}\right)^{1/2}\left(d_{\lambda_f}\right) m_1 (d_x)_{10}\sum_{k_f}\left(\frac{\omega_{k_f}}{\omega_L}\right)^{1/2}\alpha_{k_f}\,\frac{\exp i\left[\omega_{k_f}-\omega_{k_z}-\omega_{om}\right]t}{\left[\omega_{k_z}-\omega_{10}+i\Gamma_1/2\right]\left[\omega-\omega_{k_f}+\omega_{om}+i\delta\right]} \tag{C24}$$

We will proceed with the calculation for the Lorentzian packet case.

One first converts the k_z sum to an integral over positive frequency. Then, to order Δ/ω_L relative to unity, the ω integral can be extended to $-\infty$ with the resulting form,

$$f_{k_f,\lambda_f}(t) = \Delta K e^{it(\omega_{k_f}-\omega_{om})}\sqrt{\omega_{k_f}}\int_{-\infty}^{\infty}\frac{d\omega}{2\pi}\,\frac{e^{-i\omega t_1}}{(\omega-\omega_{10}+i\Gamma_1/2)(\omega-\omega_{k_f}+\omega_{om}+i\delta)\left((\omega-\omega_L)^2+\Delta^2/4\right)}, \tag{C25}$$

where

$$K = 2/\hbar\sqrt{\frac{2N\Delta\omega_L}{cV}}$$

For $t < 0$, one closes the contour in the upper-half plane picking up the residue at the pole $\omega = \omega_L + i\Delta/2$,

$$f_{k_f,\lambda_{f<}}(t) = \frac{K\sqrt{\omega_{k_f}}\exp i\left[\omega_{k_f}-\omega_{om}-\omega_L-i\Delta/2\right]t}{\left[\omega_L-\omega_{10}+i/2(\Gamma_1+\Delta)\right]\left[\omega_L-\omega_{k_f}+\omega_{om}+i\Delta/2\right]}\,. \tag{C26}$$

For $t > 0$, we close the contour picking up the residues at the three poles in the lower half of the complex ω plane,

$$f_{k_f, \lambda_f}(t) = \Delta K e^{it(\omega_{k_f} - \omega_{om})} \sqrt{\omega_{k_f}} \left\{ \frac{\exp - i[\omega_{1o} - i\Gamma_1/2]t}{[\omega_{1m} - \omega_{k_f} - i\Gamma_1/2][(\omega_{1o} - \omega_L - i\Gamma_1/2)^2 + \Delta^2/4]} \right.$$

$$+ \frac{\exp - i[\omega_{k_f} - \omega_{om}]t}{[\omega_{k_f} - \omega_{1m} + i\Gamma_1/2][(\omega_{k_f} - \omega_{om} - \omega_L)^2 + \Delta^2/4]}$$

$$\left. + \frac{i \exp - i[\omega_L - i\Delta/2]t}{\Delta[\omega_L - \omega_{1o} + i(\Gamma_1 - \Delta)/2][\omega_L - \omega_{k_f} + \omega_{om} - i\Delta/2]} \right\} . \qquad \text{(C27)}$$

We desire to compute the average rate of photon production at a time t which is contained within the frequency interval $\omega_c \pm \delta/2$, within a solid angle element $d\underline{\Omega}$. The frequency interval corresponds to a spectrometer channel. If we represent the probability by $dF_{\lambda f}(t)/d\underline{\Omega}$, the production rate is given by

$$\frac{d^2 F_{\lambda f}(t)}{dt d\underline{\Omega}} = \frac{V}{(2\pi c)^3} \int_{\omega_c - \delta/2}^{\omega_c + \delta/2} \omega_f^2 \frac{d}{dt} \langle |f_{k_f, \lambda_f}(t)|^2 \rangle_{ave.} \, d\omega_f \quad . \qquad \text{(C28)}$$

The averaging bracket $\langle \ \rangle_{ave.}$ in the above equations represents the average over the initial states of the scatterer. By performing such an average as a series of convolution integrals over distributions, we can incorporate inhomogeneous broadening effects such as collisional and Doppler broadening. For simplicity in the following we will neglect, for now, the inhomogeneous broadening.

For $t < 0$, we obtain

$$\frac{dF_{\lambda f}<(t)}{d\underline{\Omega}} = \frac{K^2 V}{(2\pi c)^3} \frac{e^{\Delta t}}{(\omega_L - \omega_{1o})^2 + (\Delta + \Gamma_1)^2/4} \int_{\omega_c - \delta/2}^{\omega_c + \delta/2} \frac{\omega_f^3 \, d\omega_f}{(\omega_f - \omega_L + \omega_{mo})^2 + \Delta^2/4} \quad . \qquad \text{(C29)}$$

We note that the absolute magnitudes of the emission and any angular dependences of the emission depend upon the evaluation of the matrix elements contained within K. We will leave this in its general form. We see that the contribution for $t < 0$ identically follows the time dependence of the envelope of the pulse with a coefficient whose magnitude depends upon the proximity to resonance and the position and width of the spectrometer channel. To terms of order $\delta/\omega_c \ll 1$ relative to unity, we obtain an emission rate,

$$\frac{d^2F_{\lambda_{f_1}<}(t)}{dt\,d\underline{\Omega}} = \frac{2K^2V\omega_c^3\Delta e^{-\Delta|t|}}{(2\pi c)^3[(\omega-\omega_{1o})^2+(\Delta+\Gamma_1)^2/4]}\left\{\tan^{-1}\left(\frac{\delta+2(\omega_c-\omega_L+\omega_{mo})}{\Delta}\right)\right.$$

$$\left. + \tan^{-1}\left(\frac{\delta-2(\omega_c-\omega_L+\omega_{mo})}{\Delta}\right)\right\} . \qquad \text{(C30)}$$

For maximum response, we center the detection channel at $\omega_c = \omega_L - \omega_{mo}$ which is the center position of the emitted Raman or Rayleigh lines. For $\delta >> \Delta, \Gamma$, which is the regime of interest, the line is contained within the spectrometer channel and the results obtained for the maximum emission rate within the channel are:

$$\frac{d^2F_{\lambda_f<}(t)}{dt\,d\underline{\Omega}} = \frac{K^2V\Delta}{c^3(2\pi)^2}\,e^{-\Delta|t|}\,\frac{(\omega_L-\omega_{mo})^3}{(\omega_L-\omega_{1o})^2+(\Delta+\Gamma_1)^2/4}\,(1+0(\Delta/\delta)) . \qquad \text{(C31)}$$

Therefore, for the emission rate for $t < 0$, we are able to derive the resonant enhancement throughout the regime of resonance. For $t > 0$, the evaluation of Eq. (C28) with the expressions given in Eq. (C27), becomes complicated for the general case. Accordingly, we will investigate two regimes: (a) near resonance $\omega_L - \omega_{1o} > \delta >> \Delta, \Gamma$; (b) resonance fluorescence $\omega_L = \omega_{1o}$. In both cases we will center the detection channel at the center of the Raman or Rayleigh lines, $\omega_c = \omega_L - \omega_{mo}$.

For the case (a) we obtain

$$\frac{dF^{(a)}_{\lambda_f>}(t)}{dt\,d\underline{\Omega}} \cong \frac{K^2V}{(2\pi c)^3}\,\frac{4(\omega_L-\omega_{mo})^3}{(\omega_{1o}-\omega_L)^2}\left\{(2+e^{-\Delta t})\tan^{-1}\delta/\Delta\right. \qquad \text{(C32)}$$

$$\left. - e^{-\Delta t}\left[\pi - e^{\Delta t/2}\,\frac{\Delta}{\delta(\delta t)}\sin\delta t/2\,(1+0(1/\delta t))\right]\right\}\,(1+0((\Delta/\delta)^2,(\Gamma_1/\delta)^2)) .$$

For times $t >> \delta^{-1} \sim 10^{-12}$ sec, our results become

$$\frac{d^2F^{(a)}_{\lambda_{f_1}>}(t)}{dt\,d\underline{\Omega}} \cong \frac{K^2V\Delta}{(2\pi)^2c^3}\,\frac{(\omega_L-\omega_{mo})^3\,e^{-\Delta|t|}}{(\omega_{1o}-\omega_L)^2} . \qquad \text{(C33)}$$

Any fluorescent contribution, i.e., with an exponential decay rate of $\exp(-\Gamma_1 t)$ obtained from the evaluation of the integrals is at least of order Δ^2/δ^2, Γ_1^2/δ^2 relative to unity.

For case (b), $\omega_L = \omega_{1o}$, resonance fluorescence, the result obtained is:

$$\frac{d^2F_{\lambda f<}(t)}{dtd\underline{\Omega}} = \frac{4K^2V\Delta}{(2\pi)^2c^3}\,\frac{(\omega_L-\omega_{mo})^3}{(\Delta+\Gamma_1)^2}\,e^{-\Delta|t|} \quad ; \tag{C34}$$

$$\frac{d^2F_{\lambda f>}(t)}{dtd\underline{\Omega}} = \frac{4K^2V\Delta}{(2\pi)^2c^3}\,\frac{(\omega_L-\omega_{mo})^3}{(\Gamma_1-\Delta)^2}\left[e^{-\Delta t/2} - \frac{2\Delta}{\Gamma_1+\Delta}\,e^{-\Gamma_1 t/2}\right]^2 \quad . \tag{C35}$$

We see that as we traverse from the near-resonance condition $\omega_L - \omega_{1o} > \delta$ to the exact resonance limit $\omega_L = \omega_{1o}$, the fluorescence part identifiable by a decay of the form $\exp(-\Gamma_1 t)$ has increased substantially in its contribution to the emission rate; that is, at near-resonance we start out with an emission that follows the packet envelope. As we then move closer into resonance both the part which follows the packet envelope and a part which exhibits an exponential decay rate become appreciably larger, with the exponential part growing at a faster rate until we achieve the resonance fluorescence condition given in Eq. (C35).

An important point to stress here is that the results obtained in Eqs. (C31) through (C35) for the Lorentzian packet are identical as far as time dependence and resonant enhancement to that obtained in the classical calculation given in Chapter II. As we remarked before, the quantum calculation for a Gaussian wave packet contains some difficult integrals; however, now that the connection between the classical and quantum mechanical cases has been determined for a Lorentzian distribution, we can reasonably infer that the same connection will prevail for the Gaussian case also.

APPENDIX D

Volume 23, number 1 CHEMICAL PHYSICS LETTERS 1 November 1973

A NEW EFFECT IN THE DEPOLARIZATION OF RESONANT LIGHT SCATTERING FROM MOLECULES IN THE VAPOR PHASE: I_2 *

S.D. SILVERSTEIN and R.L. St. PETERS
General Electric Corporate Research and Development, Schenectady, New York 12301, USA

Received 20 July 1973

Theoretical discussions of the depolarization ratios in two types of resonance processes are given. These processes are discrete state resonance fluorescence, and Raman scattering when the resonance is between a bound state and evanescent-dissociative states. Theory predicts a dramatic difference for these two cases due to a quantum mechanical phase cancellation in the case of virtual dissociative states. The predictions have been verified experimentally.

In this note, we present the results of theoretical treatments we have made on the depolarization ratios for two types of resonant light scattering processes: resonance fluorescence associated with interelectronic absorption with a specific vibrational–rotational transition, and "resonant" Raman scattering when the resonance is between a bound state and an evanescent dissociative state.

Quantum mechanics dictates a dramatic difference for the depolarization in these two processes. The concepts given here are general**; for the sake of experimental verification, we specifically apply the theory to the I_2 molecule. The theoretical predictions are a priori in the sense of *no* adjustable parameters. From the experimental results reported in the literature [2–4], and from further high resolution studies we have performed [5], we see that theory and experiment are in close agreement.

Experiments relevant to the theory have been made by Holzer et al. [2] and Kiefer and Bernstein [3]. For incident laser wavelengths above the dissociation limit in I_2, they observed depolarization ratios for the fundamental in an overtone sequence of ≈ 0.16 for the Q branch peak at high resolution and ≈ 0.35 for an area measurement incorporating the O and S branches. Berjot et al. [4], in their experiments using a 5017 Å‡ laser excitation on I_2 vapor, observed discrete state depolarization ratios of ≈ 0.75 at zero foreign gas pressure, and a reduced depolarization of ≈ 0.35 at high foreign gas pressure.

The details of the theoretical calculations as originally conceived and performed by one of us (SDS) will be published elsewhere [1]. Suffice it here to discuss the significant differences between the two resonance cases, and then to give the numerical results from the application to I_2.

First, the electronic transitions of interest in I_2 are $\Sigma \rightleftarrows \Pi_0$; hence the rotational angular momentum must change by $\Delta J = \pm 1$ in absorption or emission. This implies that the emission in resonance fluorescence will be a doublet corresponding to a Q branch ($\Delta J = 0$) and either an S ($\Delta J = +2$) or an O ($\Delta J = -2$) branch. The depolarization ratios for discrete state resonance fluorescence are known from Placzek's [6] original calculations. The O and S branches give 0.75, while the Q branch value depends upon the J quantum number. There are two different Q branch terms which we denote by Q_+ corresponding to the transition sequences $J \rightarrow J+1 \rightarrow J$, and Q_- corresponding

* This research has been supported by Contract NAS1-11624 from NASA Langley Research Center.

** The results given here correspond to transitions in symmetric top molecules for the angular momentum $K = 0$ in both states. In ref. [1] we have further generalized the results to molecules having Q branch absorptions.

‡ There is a misprint in the caption to Table 1 of ref. [4]. The correct wavelength is 5017 A, not 5107 A as printed.

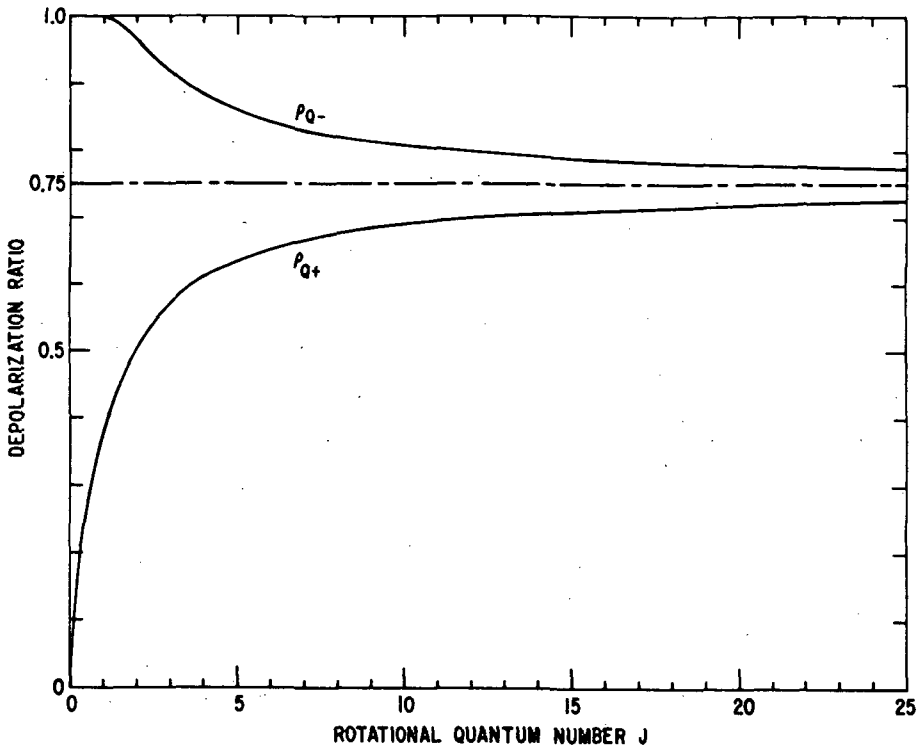

Fig. 1. A plot of the two Q branch depolarization ratios as a function of rotational angular momentum quantum number J. The $Q_{\pm}$ correspond to cases where intermediate state resonances are with states $J \pm 1$.

to $J \rightarrow J-1 \rightarrow J$. The depolarization ratios of $Q_{\pm}$ depend upon the rotational quantum number, and both asymptotically approach 0.75 in the limit of high J. We note that for the *discrete case* we are in resonance with *only one* of the two terms. The depolarization ratios $\rho_{Q_{\pm}}$ go to opposite limits at low J. For example, for $J = 0$, the perpendicular scattering is zero; hence $\rho_{Q_{\pm}}(J = 0) = 0$. On the other hand, for $J = 1$, $\rho_{Q_-}(J = 1) = 1$. In fig. 1, we plot the depolarization ratios for the Q branches as a function of J. We note that the results given here are in accord with the low pressure experiments [4] at 5017 Å, as the dominant line under the gain curve of the Ar ion laser is the R(26) 62–0 transition which has a high enough J to give a depolarization ratio of ≈ 0.75.

The situation is entirely different for the case when the incident laser frequency corresponds to transitions to evanescent, dissociative molecular states. The "outgoing" scattering solutions can be expanded in terms of a complete set of partial waves, and the energy is independent of the "rotational" quantum number J in this expansion. For a given J value, both $Q_{\pm}$ contribute and their contributions are summed prior to squaring. The very interesting consequence of the quantum mechanics which results in the new effect described here is that these two terms enter with opposite sign in the depolarized (perpendicular) component of the emission, hence effecting a cancellation and a substantial reduction in the depolarization ratio. As there is a continuum of evanescent states, one must sum the contributions from all the J values as each has a "continuum resonance".

In an actual experimental situation, the results in this case are sensitive to the spectrometer exit slit function. For example, for the case applicable to very narrow slits where we get negligible amplitudes of the O and S branch Raman emissions, even for low J's, we calculate a Stokes fundamental depolarization

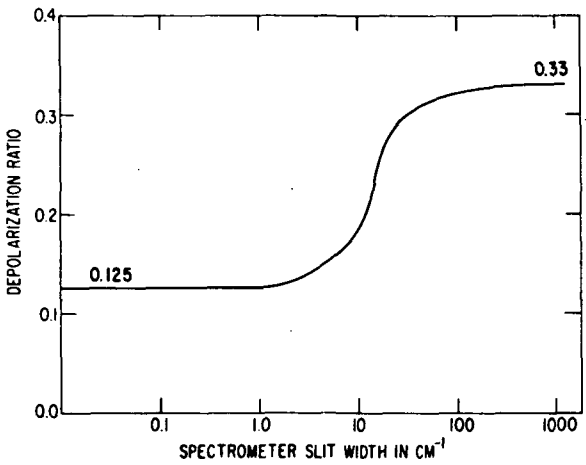

Fig. 2. A plot of the predicted, theoretical depolarization ratios for I_2 at 400°K as a function of slit width with a triangular slit function for resonant scattering from dissociative states.

ratio for the Q branch at 400°K of ≈ 0.13 for a 1 cm^{-1} spectrometer slit‡. For I_2, being so heavy, the results are insensitive to temperature.

In fig. 2, we give the theoretical predictions for the Stokes fundamental depolarization for the case of "resonance" with the evanescent-dissociative molecular states in I_2 as a function of slit width for a triangular slit function with the slit centered at the $J = 60$ Q branch frequency. The asymptotic value for small slit widths is the Q branch only contribution, quoted previously, while as the slit is widened the increase corresponds to the added contributions of the O and S branches. The wide slit asymptote, which is equivalent to an area measurement, predicts a depolarization of ≈ 0.33. The results of our a priori theory are in very good agreement with experiment [2–5]. The calculations include only the contribution of scattering from molecules in the $v = 0$ initial state. "Hot bands", or scattering from vibrationally excited molecules, have the same spectral shape and depolarization but are shifted slightly toward shorter wavelengths [3]. The hot band contribution will not affect the asymptotes of fig. 2 but may slightly alter the intermediate region. The relative contributions of the different bands can be determined by numerical calculations of the vibrational overlap integrals [7].

The most significant difference between the two types of resonance processes described here is the quantum-mechanical cancellation which occurs in the depolarized component in the scattering from evanescent intermediate states. If, however, one had a series of pressure broadened discrete states which effectively meld into a continuum, the contributions would *add incoherently*; hence there would be *no* phase cancellation and *no* anticipated substantial reduction in the depolarization ratio. This latter conclusion is quite relevant to the pressure experiments of Berjot et al. [4] and indicates that their high pressure emission is largely due to remnant scattering from excited vibrational levels via resonance with dissociative states, which is present at all pressures, while the discrete resonance fluorescent contribution from the ground vibrational level, which is dominant at low pressures, has been quenched out.

‡ We have experimentally measured a Q branch depolarization ratio of 0.12 ± 0.02 with a 1.6 cm^{-1} slit.

References

[1] S.D. Silverstein, Depolarization in the Resonant Light Scattering From Molecules in the Vapor Phase with Specific Application to I_2, to be published.
[2] W. Holzer, W.F. Murphy and H.J. Bernstein, J. Chem. Phys. 52 (1970) 399.
[3] W. Kiefer and H.J. Bernstein, J. Mol. Spectry. 43 (1972) 366.
[4] H. Berjot, M. Jacon and L. Bernard, Can. J. Spectry. 17 (1972) 60.
[5] R.L. St. Peters and S.D. Silverstein, General Electric Corporate Research and Development Report, to be published.
[6] G. Placzek, Handbuch der Radiologie, 2nd Ed., Vol. 6 (II) (1934).
[7] P.F. Williams and D.L. Rousseau, Phys. Rev. Letters 30 (1973) 951.

REFERENCES

1. Melfi, S. H. : Remote Measurements of the Atmosphere Using Raman Scattering. Applied Optics, vol. 11, no. 7, July 1972, pp. 1605-1610.

2. Grams, G. W. ; and Wyman, C. M. : Compact Laser Radar for Remote Atmospheric Probing. J. Appl. Meteorology, vol. 11, no. 7, Oct. 1972, pp. 1108-1113.

3. Lapp, M. ; Penney, C. M. ; and Asher, J. A. : Application of Light-Scattering Techniques for Measurement of Density, Temperature, and Velocity in Gasdynamics. ARL-73-0045, Jan. 1973.

4. Holzer, W. ; Murphy, W. F. ; and Bernstein, H. J. : Resonance Raman Effect and Resonance Fluorescence in Halogen Gases. J. Chem. Phys., vol. 52, no. 1, Jan. 1, 1970, pp. 399-407.

5. Penney, C. M. ; Goldman, L. M. ; and Lapp, M. : Raman Scattering Cross Sections. Nature, vol. 225, no. 58, Feb. 7, 1972, pp. 110-112.

6. Rudder, Ralph R. ; and Bach, David R. : Rayleight Scattering of Ruby-Laser Light by Neutral Gases. J. Opt. Soc. Amer., vol. 58, no. 9, Sept. 1968, pp. 1260-1266.

7. Berjot, M. ; Jacon, M. ; and Bernard, L. : Effet Raman de Resonance par Excitation dans le Continuum d'Absorption: Sections Efficaces Relatives de Diffusion. Optics Communications, vol. 4, no. 2, Oct. 1971, pp. 117-120.

8. Berjot, M. ; Jacon, M. ; and Bernard, L. : Effet Raman de Resonance par Excitation dans le Continuum d'Absorption: Importance des Transitions Virtuelles. Optics Communications, vol. 4, no. 3, Nov. 1971, pp. 246-248.

9. Jacon, Marcel; Berjot, Maurice; Bernard, Lucien: Optique Moléculaire-Passage Continu de la Fluorescence de Résonance a l'Effet Raman de Résonance. C. R. Acad. Sc. Paris. vol. 273, series B, Nov. 29, 1971, pp. 956-959.

10. Berjot, Maurice; Jacon, Marcel; and Bernard, Lucien: Passage Continu de la Fluorescence de Résonance à l' Effet Raman de Résonance. Can. J. Spectroscopy, vol. 17, no. 2, March 1972, pp. 60-62.

11. Fouche, D. G. ; Herzenberg, A. ; and Chang, R. K. : Inelastic Photon Scattering by a Polyatomic Molecule: NO_2. J. Appl. Phys., vol. 43, no. 9, Sept. 1972, pp. 3846-3851.

12. Mitchell, Allan Charles Grey; and Zemansky, Mark W.: Resonance Radiation and Excited Atoms. The Macmillon Co., 1934.

13. Fouche, D. G.; and Chang, R. K.: Observation of Resonance Raman Scattering below the Dissociation Limit in I_2 Vapor. Phys. Rev. Lett. vol. 29, no. 9, Aug. 28, 1972, pp. 536-539.

14. St. Peters, R. L.; Silverstein, S. D.; Lapp, M; and Penney, C. M.: Resonance Raman Scattering or Resonance Fluorescence in I_2 Vapor? Phys. Rev. Lett., vol. 30, no. 6, Feb. 5, 1973, pp. 191-192.

15. Bowman, M. R.; Gibson, A. J.; and Sandford, M. C. W.: Atmospheric Sodium Measured by a Tuned Laser Radar. Nature, vol. 221, Feb. 1, 1969, p. 456.

16. Felix, F.; Keenliside, W.; Kent, G. S.; and Sandford, M. C. W.: Laser Radar Measurements of Atmospheric Potassium. Paper presented at Fifth Conference on Laser Radar Studies of the Atmosphere (Williamsburg, Va.) June 4-6, 1973.

17. Glauber, R. J.: Quantum Theory of Coherence, in Quantum Optics, S. S. Kay, and A. Maitland, eds., Academic Press, New York, 1970.

18. Penney, C. M.: Light Scattering in Terms of Oscillator Strengths and Refractive Indices. J. Opt. Soc. Amer., vol. 59, no. 1, Jan. 1969, pp. 34-42.

19. Griggs, M.: Absorption Coefficients of Ozone in the Ultraviolet and Visible Regions. J. Chem. Phys. vol. 49, no. 2, July 15, 1968, pp. 857-859.

20. Mettee, H. D.: Fluorescence and Phosphorescence of SO_2 Vapor. J. Chem. Phys. vol. 49, no. 4, Aug. 15, 1968, pp. 1784-1793.

21. Bethke, George W.: Oscillator Strengths in the Far Ultraviolet. I. Nitric Oxide. J. Chem. Phys., vol. 31, no. 3, Sept. 1959, pp. 662-668.

22. St. Peters, R. L.; and Silverstein, S. D.: Manifestations of Pressure Broadening on Tuned Resonance Raman Fluorescence. Optics Communications, vol. 7, no. 3, March 1973, pp. 193-196.

23. Herzberg, Gerhard,: Molecular Spectra and Molecular Structure. Vol. II. Infrared and Raman Spectra of Polyatomic Molecules. D. Van Nostrand Co., Inc. (New York), 1945.

24. Hall, Jr., T.C.; and Blacet, F.E.: Separation of the Absorption Spectra of NO_2 and N_2O_4 in the Range of 2400-500 A. J. Chem. Phys. vol. 20, no. 11, Nov. 1952, pp. 1745-1749.

25. Behringer, Josef: Observed Resonance Raman Spectra. pp. 168-223 in Raman Spectroscopy. Herman A Szymanski, ed., Plenum Press, 1967.

26. Kiefer, W.; and Bernstein, H.J.: Vibration-Rotational Structure in the Resonance Raman Effect of Iodine Vapor. J. Mol. Spectr., vol. 43, no. 3, Sept. 1972, pp. 366-381.

27. Williams, P.F.; and Rousseau, D.L.: Resonant Raman Scattering from Iodine: Spectral Changes with Excitation Frequency. Phys. Rev. Lett., vol. 30, no. 20, May 14, 1973, pp. 951-954.

28. Placzek, G.: Rayleigh-Streuung und Raman Effekt. Handbuch der Radiologie, Vol. 6, Part 2, Akademische Verlagsgesellschaft, 1934. English Trans. UCRL-Trans-526(L).

29. Mrozowski, S.: The Polarization of Band Fluorescence of Some Metallic Vapors. Acta Phys. Pol., vol. 7, 1938, pp. 45-48.

30. Pringsheim, Peter: Fluorescence and Phosphorescence. Interscience Publishers, Inc. (New York), 1963.

31. Silverstein, S.D.; and St. Peters, R.L.: A New Effect in the Depolarization of Resonant Light Scattering from Molecules in the Vapor Phase: I_2. Chem. Phys. Letts., vol. 23, no. 1, Nov. 1, 1973, pp. 140-142.

32. Stair, Ralph; Schneider, William E.; and Jackson, John K.: A New Standard of Spectral Irradiance. Applied Optics, vol. 2, no. 11, Nov. 1963, pp. 1151-1154.

33. Anon.: Eastman White Reflectance Paint, Kodak Publication No. JJ-32.

34. Sakurai, Katsumi; and Broida, H.P.: Spectral Study of NO_2 Fluorescene Excited by 11 Lines of Argon and Krypton Ion Lasers. J. Chem. Phys. vol. 50, no. 6, March 15, 1969, pp. 2404-2410.

35. Sackett, Philip B.; and Yardley, James T.: Radiative Lifetime of Nitrogen Dioxide using a Tunable Organic Dye Laser. Chem. Phys. Lett. vol. 6, no. 4, Aug. 15, 1970, pp. 323-325.

36. Sackett, P. B.; and Yardley, J. T.: Short-Lived Fluorescence from Nitrogen Dioxide. Chem. Phys. Lett. vol. 9, no. 6, June 15, 1971, pp. 612-614.

37. Sackett, Philip B.; and Yardley, James T.: Dynamics of NO_2 Electronic States Excited by a Tunable Dye Laser. J. Chem. Phys., vol. 51, no. 1, July 1, 1972, pp. 152-166.

38. Stevens, C. G.; Swagel, M. W.; Wallace, R.; and Zare, R. N.: Analysis of Polyatomic Spectra Using Tunable Laser-Induced Fluorescence: Applications to the NO_2 Visible Band System. Chem. Phys. Lett., vol. 18, no. 4, Feb. 15, 1973, pp. 465-469.

39. Douglas, A. E.: Anomalously Long Radiative Lifetimes of Molecular Excited States. J. Chem. Phys., vol. 45, no. 3, Aug. 1, 1966, pp. 1007-1015.

40. Penney, C. M.; St. Peters, R. L.; and Lapp, M.: Absolute Intensity and Polarization of Rotational Raman Scattering from N_2, O_2, and CO_2. NASA CR-121091, 1973.

41. Fouche, D. G.; and Chang, R. K.: Relative Raman Cross Section for O_3, CH_4, C_8H_8, NO, N_2O and H_2. Appl. Phys. Lett. vol. 20, no. 7, April 1, 1972, pp. 256-257.

42. Fouche, D. G.; and Chang, R. K.: Relative Raman Cross Section For N_2, O_2, CO, CO_2, SO_2, and H_2S. Appl. Phys. Letts. vol. 18, no. 12, June 15, 1971, pp. 597-580.

43. Hänsch, T. W.: Repetitively Pulsed Tunable Dye Laser for High Resolution Spectroscopy. Appl. Opt. vol. 11, no. 4, April 1972, pp. 895-898.

44. Bergman, A.; David, R.; and Jortner, J.: A Powerful Broad Band Tunable Dye Laser. Opt. Comm., vol. 4, no. 6, Feb./March 1972, pp. 431-433.

45. Singh, S.; Bonner, W. A.; Potopowicz, J. R.; and van Uitert, L. G.: Nonlinear Susceptibility of Lithium Formate Monohydrate. Appl. Phys. Lett., vol. 17, no. 7, Oct. 1, 1970, pp. 292-294.

46. Washburn, Edward W., ed.: International Critical Tables. Vol. VII. McGraw-Hill, Inc., 1930.

47. Clements, J. H.: On the Absorption Spectrum of Sulphur Dioxide. Phys. Rev., vol. 47, no. 3, Feb. 1, 1935, pp. 224-232.

48. Price, W.C.; and Simpson, D.M.: Absorption Spectra of Sulphur Dioxide and Carbon Disulphide in the Vacuum Ultra-Violet. Proc. Roy. Soc., vol. A165, 1938, pp. 272-278.

49. Metropolis, N.; and Beutler, H.: Absorption System of Sulphur Dioxide at 3800Å. Phys. Rev., vol. 57, June 1, 1940, p. 1078.

50. Metropolis, N.: The Structure of Electronic Bands of Polyatomic Molecules. Phys. Rev., vol. 60, no. 4, Aug. 15, 1941, pp. 283-294.

51. Metropolis, N.: Vibrational Analysis of the Absorption System of Sulphur Dioxide of λ 3400-2600. Phys. Rev., vol. 60, no. 4, Aug. 15, 1941, pp. 295-301.

52. Merer, A. J.: Rotational Analysis of Bands of the 3800Å System of SO_2. Discussions of the Faraday Society, no. 35, 1963, pp. 127-136.

53. Warneck, P.; Marmo, F.F.; and Sullivan, J.O.: Ultraviolet Absorption of SO_2. Dissociation Energies of SO_2 and SO. J. Chem. Phys., vol. 40, no. 4, Feb. 15, 1964, pp. 1132-1136.

54. Schotland, R.M.; Chang, D.; and Bradley, J.: Study of Active Probing of Water Vapor Profiles and Results of Experiments. New York University, College of Engineering and Science, Tech. Rep. No. GSL-TR-65-6, 1965.

55. Byer, Robert L.; and Garbuny, Max: Pollutant Detection by Absorption Using Mie Scattering and Topographic Targets are Retroreflectors. Appl. Opt., vol. 12, no. 7, July 1973, pp. 1496-1505.

56. Kildal, Helge; and Byer, Robert L.: Comparison of Laser Methods for the Remote Detection of Atmospheric Pollutants. Proc. IEEE, vol. 59, no. 12, Dec. 1971, pp. 1644-1663.

57. Dinev, S.G.; Stamenov, K.V.; and Tomov, I.V.: Generation of Tunable UV Radiation in the Range 216-314 nm. Optics Communications, vol. 5, no. 5, Aug. 1972, pp. 419-421.

58. Penner, S.S.: Quantitative Molecular Spectroscopy and Gas Emissivities. Addison-Wesley Publishing Co., Inc. 1959.

59. Staff of United States Air Force Air Research and Development Command, Air Force Research Division, Geophysics Research Directorate: Handbook of Geophysics. Macmillian (New York), 1960.

60. Mavrodineanu, Radu; and Boiteux, Henri: Flame Spectrscopy. John Wiley and Sons, Inc., 1965.

61. Hibben, J. H.: The Raman Effect and its Chemical Applications. Reinhold Press (New York), 1939.

62. Goldberger, M. L.; and Watson, K. M.: Collision Theory. Oxford University Press, 1954.

63. For a recent review article with additional references, see: Glauber, R. J.: Quantum Theory of Coherence, in Quantum Optics. Kay, S. H., and Maitland, A., editors, Academic Press, New York, 1970.

NASA CR-132363

DISTRIBUTION LIST
NAS1-11624

	No. Copies
NASA Langley Research Center Hampton, VA 23665	
Attn: Report & Manuscript Control Office, Mail Stop 180A	1
Raymond L. Zavasky, Mail Stop 115	1
Wendell G. Ayers, Mail Stop 217K	1
Dr. Frank Allario, Mail Stop 193A	1
Dr. Reginald J. Exton, Mail Stop 235A	1
Dr. G. Burton Northam, Mail Stop 401A	10
NASA Ames Research Center Moffett Field, CA 94035	
Attn: Library, Mail Stop 202-3	1
NASA Flight Research Center P.O. Box 273 Edwards, CA 93523	
Attn: Library	1
NASA Goddard Space Flight Center Greenbelt, MD 20771	
Attn: Library	1
Richard J. Pinamonti, Jr.	1
NASA Lyndon B. Johnson Space Center 2101 Webster Seabrook Road Houston, TX 77058	
Attn: Library, Code JM6	1
M. Jay Harnage, Jr., Code HC	1
Dr. Robert D. Hudson, Code TN2	1
Jet Propulsion Laboratory 4800 Oak Grove Drive Pasadena, CA 91103	
Attn: Library, Mail 111-113	1
NASA Wallops Station Wallops Island, VA 23337	
Attn: Library	1
Alfred C. Holland, Code DAS, Building E-106	1

	Copies
NASA Lewis Research Center 21000 Brookpark Road Cleveland, OH 44135	
Attn: Library, Mail Stop 60-3	1
Tom A. Coney, Mail Stop 500-318	1
Jack A. Salzman, Mail Stop 500-318	1
NASA Marshall Space Flight Center Huntsville, AL 35812	
Attn: Library	1
Kenneth A. Kadrmas, S&E-AERO-F	1
NASA John F. Kennedy Space Center Kennedy Space Center, FL 32899	
Attn: Library, IS-DOC-1L	1
National Aeronautics & Space Administration Washington, DC 20546	
Attn: KSS-10/Library	1
ERF/Michael A. Calabrese	1
ERF/Jules Lehmann	1
ERF/Luke L. Liccini	1
REE/Dr. Bernard Rubin	1
Environmental Protection Agency National Environmental Research Center P. O. Box 15027 Las Vegas, NV 89114	
Attn: Dr. S. Harvey Melfi	1
Environmental Protection Agency Research Triangle Park, NC 27711	
Attn: Bill Herget	1
United Aircraft Corporation United Aircraft Research Laboratories East Hartford, CT 06108	
Attn: Bill Morey	1
Stanford University Department of Physics Menlo Park, CA 94305	
Attn: Dr. Bob Byers	1

	Copies
Block Engineering, Inc. 19 Blackstone Street Cambridge, MA 02139 Attn: Stanley Klainer	1
Dr. Rudolf Penndorf 148 Oakland Street Wellesley Hills, MA 02181	1
New York University University Heights Bronx, NY 10453 Attn: Professor Richard M. Schotland	1
University of Missouri Rolla, MO 65581 Attn: Dr. Burton Schuster	1
Mitre Corporation McLean, VA 22067 Attn: Edward A. Ward	1
University of Wisconsin 1225 Dayton Street Madison, WI 53706 Attn: Dr. Edwin Eloranta James Weinman	1 1
Stanford Research Institute 333 Ravenswood Avenue Menlo Park, CA 94025 Attn: Edward K. Proctor, Jr. R. T. H. Collis	1 1
Air Force Cambridge Research Laboratories Bedford, MA 01731 Attn: Dr. Louis Elterman Dr. Frederic E. Volz (OPA)	1 1
McDonnell Douglas Corporation McDonnell Douglas Aerospace Center 5301 Bolsa Avenue Huntington Beach, CA 92647 Attn: Dr. Jack Grossman, A3-833	1

	Copies
Drexel University Philadelphia, PA 19104 Attn: Professor John A. Cooney	1
Massachusetts Institute of Technology Lincoln Laboratory P. O. Box 73 Lexington, MA 02173 Attn: Dr. Daniel G. Fouche Dr. Paul L. Kelly	1 1
University of Arizona Tucson, AZ 85721 Attn: Dr. Ben Herman	1
Edgewood Arsenal, MD 21010 Attn: Harvey Tannenbaum	1
College of the City of New York Convent Avenue and W 139 Street New York, NY 10031 Attn: Professor Samir A. Ahmed	1
The Aerospace Corporation Electronics Research Laboratories Wuantum Optics Department P. O. Box 92957 Los Angeles, CA 90045 Attn: Dr. Milton Birnbaum	1
Martin Marietta Corporation The Martin Company Denver Division Post Office Box 179 Denver, CO 80201 Attn: Nicholas J. Ganiaris	1
National Center for Atmospheric Research Boulder, CO 80302 Attn: Dr. Gerald W. Grams	1

	Copies
Tohoku University Research Institute of Electrical Communication Katahira 2-Chome Sendai 980, Japan Attn: Professor Humio Inaba	1
Canada Center for Remote Sensing Department of Eenergy Mines & Resources Ottawa, Ontario k1AOE4 Canada Attn: Dr. Michael Bristow	1
NASA Scientific & Technical Information Facility P. O. Box 33 College Park, MD 20740	12 plus reproducible